University of New Hampshire
University of New Hampshire Scholars' Repository

Doctoral Dissertations Student Scholarship

Winter 2006

Modeling of diffusional creep and stress relaxation in copper grains during manufacturing of microelectronic integrated circuits

Vasyl M. Grychanyuk
University of New Hampshire, Durham

Follow this and additional works at: https://scholars.unh.edu/dissertation

Recommended Citation
Grychanyuk, Vasyl M., "Modeling of diffusional creep and stress relaxation in copper grains during manufacturing of microelectronic integrated circuits" (2006). *Doctoral Dissertations*. 352.
https://scholars.unh.edu/dissertation/352

This Dissertation is brought to you for free and open access by the Student Scholarship at University of New Hampshire Scholars' Repository. It has been accepted for inclusion in Doctoral Dissertations by an authorized administrator of University of New Hampshire Scholars' Repository. For more information, please contact nicole.hentz@unh.edu.

MODELING OF DIFFUSIONAL CREEP AND STRESS RELAXATION IN COPPER GRAINS DURING MANUFACTURING OF MICROELECTRONIC INTEGRATED CIRCUITS

BY

VASYL M. GRYCHANYUK

B.S./M.S., Dnepropetrovsk National University, Ukraine, 2001

DISSERTATION

Submitted to the University of New Hampshire
In Partial Fulfillment of
The Requirements for the Degree of

Doctor of Philosophy

in

Mechanical Engineering

December 2006

Reproduced with permission of the copyright owner. Further reproduction prohibited without permission.

UMI Number: 3241642

INFORMATION TO USERS

The quality of this reproduction is dependent upon the quality of the copy submitted. Broken or indistinct print, colored or poor quality illustrations and photographs, print bleed-through, substandard margins, and improper alignment can adversely affect reproduction.

In the unlikely event that the author did not send a complete manuscript and there are missing pages, these will be noted. Also, if unauthorized copyright material had to be removed, a note will indicate the deletion.

UMI®

UMI Microform 3241642
Copyright 2007 by ProQuest Information and Learning Company.
All rights reserved. This microform edition is protected against unauthorized copying under Title 17, United States Code.

ProQuest Information and Learning Company
300 North Zeeb Road
P.O. Box 1346
Ann Arbor, MI 48106-1346

Reproduced with permission of the copyright owner. Further reproduction prohibited without permission.

This dissertation has been examined and approved:

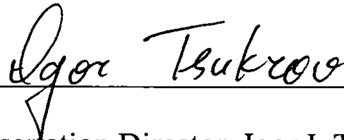

Dissertation Director, Igor I. Tsukrov
Associate Professor of Mechanical Engineering

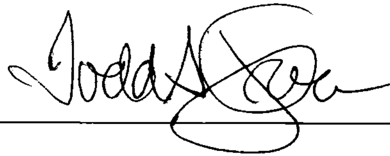

Dissertation Co-Director, Todd S. Gross
Professor and Chair of Mechanical Engineering

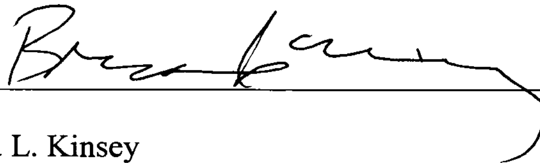

Brad L. Kinsey
Assistant Professor of Mechanical Engineering

Marianna A. Shubov
Professor of Mathematics

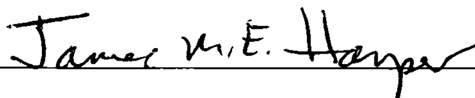

James M. Harper
Professor of Physics

11/7/06
Date

Reproduced with permission of the copyright owner. Further reproduction prohibited without permission.

ACKNOWLEDGMENTS

The author would like to express his deepest appreciation and gratitude to his dissertation advisor Prof. Igor Tsukrov for his guidance and support throughout the course of the program. His vast experience and extensive knowledge were essential to complete this research.

The author also would like to express his sincere thanks and appreciation to the PhD co-advisor Prof. Todd Gross, whose insights shaped the foundation of this research project and whose guidance and encouragement was tremendously important for the success of the research efforts.

The author also wishes to thank Shaoning Yao for help with Atomic Force Microscope, Jindra Novak for his interest in this project and fruitful discussions, Sheldon Parent for help with maintenance of the Computational Mechanics Lab and Tracey Harvey for help with administrative responsibilities.

This work was supported by the National Science Foundation, Division of Manufacturing and Industrial Innovation, under Grant No. DMI-0300216. The donation of the Cu-damascene sample by IBM is gratefully acknowledged.

Reproduced with permission of the copyright owner. Further reproduction prohibited without permission.

TABLE OF CONTENTS

ACKNOWLEDGMENTS iii

TABLE OF CONTENTS iv

LIST OF TABLES viii

LIST OF FIGURES ix

ABSTRACT xv

CHAPTER PAGE

1. INTRODUCTION 1

   1.1. Copper interconnects in the integrated circuit technology 1

   1.2. Failures in copper interconnects attributed to diffusional creep 3

   1.3. Overview of existing approaches to the modeling of diffusional creep processes 5

   1.4. Objective and scope 10

2. COUPLED FORMULATION OF TRANSIENT ELASTICITY-VACANCY DIFFUSION PROBLEM 14

   2.1. Equilibrium vacancy concentration and stress-induced mass flow 15

      2.1.1. Thermodynamic approach to equilibrium vacancy concentration 15

      2.1.2. Kinetics of stress-induced mass flow 19

   2.2. Coupled governing equations of elasticity and vacancy diffusion 22

      2.2.1. Coupling through grain boundary vacancy flux 22

Reproduced with permission of the copyright owner. Further reproduction prohibited without permission.

2.2.2. Coupling through diffusional creep strain rate 29

3. NUMERICAL MODELING OF DIFFUSIONAL CREEP USING COMMERCIAL FINITE ELEMENT PACKAGE MSC.MARC 32

3.1. Incremental solution of transient coupled governing equations 33

3.1.1. Incremental principle of virtual work and explicit time integration 33

3.1.2. MSC.Marc finite element mesh and element types 35

3.1.3. Treatment of discrete grain assembly in a continuum model using multipoint constraints 36

3.2. Reduction of computer computation time 38

3.2.1. Mesh refinement multipoint constraints 41

3.2.2. Selection of adjustable time step and stability of incremental procedure 45

3.2.3. Increase of computation efficiency using extrapolation 46

4. DIFFUSIONAL CREEP AND STRESS RELAXATION IN PERIODIC GRAIN ASSEMBLIES AND VALIDATION OF FINITE ELEMENT PROCEDURE 54

4.1. Stress relaxation of Cu linear square grain array...55

4.1.1. Modeling assumptions and parameters...56

4.1.2. Evolution of stress field in the grain array...59

4.1.3. Temperature dependence of free surface profile and contribution of Nabarro-Herring and Coble creep mechanisms 63

4.1.4. Estimate of relaxation time 64

4.2. Diffusional creep in 3x3 grain assembly 66

4.2.1. Evolution of tractions on internal grain boundaries..............................67

Reproduced with permission of the copyright owner. Further reproduction prohibited without permission.

4.2.2. Dependence of diffusional creep rate on grain size 72

4.2.3. Effect of grain boundary thickness on diffusional creep rate predictions 73

5. SEVERAL EXAMPLES OF FINITE ELEMENT PREDICTIONS OF STRESS RELAXATION IN TYPICAL COPPER INTERCONNECT STRUCTURES 75

5.1. Modeling of single-level structure subjected to thermal load 76

5.1.1. Elastic stress field in interconnect lines subjected to thermal load 77

5.1.2. Modeling of transient stress relaxation using coupled finite element approach 81

6. MODELING OF DIFFUSIONAL CREEP CONSTITUTIVE BEHAVIOR WITH EQUIVALENT VISCOPLASTIC FINITE ELEMENTS 86

6.1. Computational challenges of diffusional creep modeling 87

6.2. Mathematical description of diffusional creep constitutive behavior 88

6.3. Effective diffusional creep law for grain boundary layer and grain interior 90

6.3.1. Stress relaxation numerical experiment for grain corner region 90

6.3.2. Stress relaxation numerical experiment for grain boundary layer 96

6.4. Approximation of diffusional creep behavior in the entire Cu grain with four effective creep laws 107

6.4.1. Effective creep laws in Cu grain corners, grain boundary region and grain interior 109

6.4.2. Effective creep laws in Cu grain corners, grain boundary layer and grain interior 114

7. CONCLUSION 121

Reproduced with permission of the copyright owner. Further reproduction prohibited without permission.

LIST OF REFERENCES 126

APPENDIX A. LISTING FOR MSC.MARC FORTRAN USER SUBROUTINES ..130

Reproduced with permission of the copyright owner. Further reproduction prohibited without permission.

LIST OF TABLES

Table 3.1. Parameters of test computation to compare the performance of coupling approach through grain boundary flux and coupling through diffusional creep strain rate 41

Table 4.1. Values of parameters used in the stress relaxation modeling of periodic copper grain array to compare numerical and theoretical predictions. 58

Table 4.2. Numerical values of parameters for creep response modeling of 3x3 grain assembly to compare the model predictions to the results of Garikipati et al. [26]. 69

Table 5.1. Mechanical properties of materials used in a typical interconnect line........77

Reproduced with permission of the copyright owner. Further reproduction prohibited without permission.

LIST OF FIGURES

Figure 1.1. Atomic force microscope topographical map of Cu interconnect line sample supplied by IBM Corporation. 1

Figure 1.2. Outline of major steps in the dual damascene interconnect metallization technique. 2

Figure 1.3. Schematic illustration of the deformed shape in a typical uncapped single-level interconnect line subjected to the elevated temperature during thermal cycle. 4

Figure 1.4. Nabarro-Herring and Coble diffusion creep models. 7

Figure 2.1. Qualitative illustration of equilibrium vacancy concentration defined by a) hydrostatic stress σ_h and b) traction σ_n normal to grain boundary. 18

Figure 2.2. Vacancy fluxes due to concentration gradients within a grain. 19

Figure 2.3. Schematic illustration of the enhanced diffusivity region at grain boundaries 20

Figure 2.4. The enhancement of diffusivity in grain boundary region due to the reduction of the activation energy for vacancy motion. 21

Figure 2.5. Simulation sequence performed on each time step. Elastic loading is followed by the solution of transient concentration problem resulting in the accumulation of diffusion creep displacements in the unloaded configuration. 25

Figure 2.6. Schematic illustration of compatibility constraints that need to be applied in addition to external boundary conditions in a body that contains several neighboring grains 26

Figure 2.7. Normal and tangent components of surface vacancy flux at a grain boundary. 27

Figure 2.8. Unloaded and current loaded configurations for a body that contains multiple grains. 29

Figure 2.9. Schematic illustration of diffusion creep strain rate concept. The arrows that illustrate atomic flux $\mathbf{j}_a$ are understood as the mass flow velocities of material element faces. 30

Reproduced with permission of the copyright owner. Further reproduction prohibited without permission.

Figure 3.1. Finite element mesh of idealized square grain. The shaded area represents the grain boundary region with a typical thickness of 1 nm. 36

Figure 3.2. Degrees of freedom for adjacent nodes of neighboring grains constrained by Eq. (3.5)...37

Figure 3.3. Grain boundary sliding model suggested by Raj and Ashby [20]...............38

Figure 3.4. The predictions of concentration profile are close for both coupling approaches through GB vacancy flux and through creep strain rate. 40

Figure 3.5. First order mesh refinement multipoint constraint. 42

Figure 3.6. Comparison of vacancy concentration field predictions for FEA models with continuous mesh and mesh refinement multipoint constraints at temperature 800 K, time t = 0.01 s. 43

Figure 3.7. Comparison of stress σ_{xx} predictions for FEA models with continuous mesh and mesh refinement multipoint constraints at temperature 800 K, time t = 0.01 s. (a) Distribution of stresses. (b) Evolution of average stress.....................44

Figure 3.8. Example of the growth of oscillations that occurs during forward time integration when time step exceeds the critical value required for stability of explicit procedure..46

Figure 3.9. Test problem used to evaluate the performance of vacancy flux and concentration nodal time series extrapolation...48

Figure 3.10. Dependence of the extrapolation error on the fraction of "recovery" steps in extrapolation sequence. 51

Figure 3.11. Stability of repeating extrapolation sequence for total number of sequence steps $N_s = 1000$. (a) third order extrapolation polynomial, N_r = 500. (b) third order extrapolation polynomial, N_r = 900. (c) second order extrapolation polynomial, N_r = 900. (d) first order extrapolation polynomial, N_r = 900..52

Figure 3.12. Dependence of extrapolation accuracy on the selection of extrapolation base point. 53

Figure 4.1. Model of periodic square grain array used for validation of finite element procedure...56

Figure 4.2. Periodic grain array subjected to fixed strain. (a) Initial purely elastic deformation after instantaneous application of ε_x at time t = 0. (b) Schematic of expected evolution of free surface profile due to mass flow. 59

Reproduced with permission of the copyright owner. Further reproduction prohibited without permission.

Figure 4.3. Evolution of normal stress distribution along the internal grain boundary (x = 0) at temperatures $T = 0.7T_m$ (solid lines) and $T = 0.3T_m$ (dashed lines). Predictions of Gao et al. [17] shown by triangles are reported as approximately independent of temperature. 61

Figure 4.4. Grain boundary diffusion wedge model of polycrystalline film subjected to uniform externally applied strain (Gao et al. [17]). 62

Figure 4.5. Relaxation of average stress $\langle \sigma_{xx} \rangle$. Insets show the distribution of σ_{xx} at selected time instances. 62

Figure 4.6. Free surface profile at time $t = \tau$ for stress relaxation at different temperatures. 63

Figure 4.7. Maxwell model of a solid. 64

Figure 4.8. Comparison of diffusional creep theoretical estimate of relaxation time τ to the finite element predictions. 66

Figure 4.9. FEA model of 3x3 grain assembly. Symmetry allows to reduce the number of elements in the model by 75 %. 68

Figure 4.10. Stress distribution at time t = 500 s in 3x3 grain assembly subjected to externally applied biaxial traction. Parameters for this computation are specified in Table 4.2. 70

Figure 4.11. Traction normal to internal grain boundary of center grain at time t = 500 s. 71

Figure 4.12. Creep rate dependence on grain size at temperature T = 673 K and applied stress 100 MPa. Comparison of finite element results to theoretical predictions of Nabarro-Herring and Coble. 73

Figure 4.13. Creep rate dependence on the choice of grain boundary region thickness for the 100 nm grain. 74

Figure 5.1. Schematic illustration of cross-section of a typical single-level interconnect structure. 76

Figure 5.2. Two-dimensional plane strain model of periodic interconnect unit cell. (a) Geometry and (b) thermomechanical loading. 78

Figure 5.3. Contour plots of stress σ_{xx} in thermally loaded single-level interconnect structure 79

Figure 5.4. Contour plots of stress σ_{yy} in thermally loaded single-level interconnect structure. 80

Reproduced with permission of the copyright owner. Further reproduction prohibited without permission.

Figure 5.5. Contour plots of stress σ_{xy} in thermally loaded single-level interconnect structure. 80

Figure 5.6. Evolution of average stress and deformed shape for a typical Cu-Ta-dielectric structure under thermal loading. 82

Figure 5.7. Two-dimensional model of periodic interconnect line structure experimentally studied by Singh et al. [29]. (a) Geometry. (b) Finite element mesh. (c) Initial stress σ_{xx} after application of thermal load. 83

Figure 5.8. Comparison of finite element predictions to experimental results of Singh et al. [29]. 85

Figure 6.1. Finite element model used to establish effective creep law for grain corner region assuming that stress relaxation occurs due to vacancy fluxes from top surface to internal grain boundary....92

Figure 6.2. FEA predictions of effective creep law for grain corner region in the temperature range from 473K to 1073K. The computed data is fitted with power law equation (6.5)....93

Figure 6.3. Temperature dependence of parameters A and $\dot{\varepsilon}_{\infty}$ obtained by fitting Eq. (6.5) to FEA predictions of creep law curves shown in Figure 6.2. 95

Figure 6.4. Comparison of stress σ_{xx} at time $t = 3.0 \cdot 10^{-3}$ s computed according to (a,b) equivalent viscoplastic element technique and (c,d) coupled FEA formulation. 96

Figure 6.5. Finite element model used to establish effective creep law behavior for GB layer. Equivalent stress and strain rate are averaged over the regions numbered 1 through 10. 98

Figure 6.6. FEA predictions of effective creep law for grain boundary layer at temperature 673 K. Creep laws are shown for the regions numbered 1 through 10 in Figure 6.5. 99

Figure 6.7. Distribution of (a) vacancy concentration and (b) concentration gradient along the internal grain boundary during the transient stress relaxation of GB layer. 101

Figure 6.8. Comparison of equivalent creep law predictions for GB layer and grain corner region. 102

Figure 6.9. (a) Equivalent FEA model of Cu ¼ grain with diffusional creep laws in the GB layer as shown in Figure 6.6 (b) "benchmark" coupled elasticity-mass flow FEA model. 103

Reproduced with permission of the copyright owner. Further reproduction prohibited without permission.

Figure 6.10. Comparison of stress σ_{xx} at the initial, intermediate and final stages of stress relaxation; (a)-(c): equivalent FEA model with effective creep law in GB layer, (d)-(f): "benchmark" coupled elasticity-mass flow FEA model. 104

Figure 6.11. Time evolution of average stress in the ¼ grain model. Predictions of equivalent element technique are compared to the "benchmark"coupled FEA simulation. 105

Figure 6.12. Time evolution of nodal stress in the ¼ grain model. Predictions of equivalent element technique are compared to the "benchmark"coupled FEA simulation. 106

Figure 6.13. Deformed shape and vertical displacements in the equivalent GB layer finite element model at the final stage of stress relaxation 107

Figure 6.14. Equivalent FEA model of Cu grain with four effective diffusion creep laws and 1nm GB region. 110

Figure 6.15. FEA predictions of effective creep laws in the grain corners and the rest of 1nm GB region at temperature 673 K. 111

Figure 6.16. Approximation of creep behavior in the grain interior with a single effective creep law averaged over the areas of GB layer and the rest of the grain interior. 111

Figure 6.17. Approximation of creep behavior in the grain interior with a single effective creep law averaged over the entire area of the grain interior. 112

Figure 6.18. Time evolution of average stress in the equivalent model of Cu grain with the creep behavior approximated by four creep laws in the GB region and the grain interior. 112

Figure 6.19. Predictions of time evolution of stress σ_{xx} in the grain corner node A for the equivalent FEA model with four creep laws in the GB region and the grain interior. 113

Figure 6.20. Predictions of time evolution of stress σ_{xx} in the grain center node B for the equivalent FEA model with four creep laws in the GB region and the grain interior. 113

Figure 6.21. Equivalent FEA model of Cu grain with coarse mesh, 5nm GB layer and four effective diffusion creep laws. 115

Figure 6.22. FEA predictions of four effective creep laws in the grain corners, 5nm GB layer and grain interior at temperature 673 K. 116

Reproduced with permission of the copyright owner. Further reproduction prohibited without permission.

Figure 6.23. Average stress in the equivalent Cu grain model with coarse mesh and the creep behavior approximated by four creep laws in the GB layer and the grain interior. 117

Figure 6.24. Stress σ_{xx} in the grain corner node A predicted by the equivalent FEA model with coarse mesh and four creep laws in the GB layer and the grain interior. 117

Figure 6.25. Stress σ_{xx} in the grain center node B predicted by the equivalent FEA model with coarse mesh and four creep laws in the GB layer and the grain interior. 118

Figure 6.26. Equivalent FEA model of Cu grain with refined mesh, 5nm GB layer and four effective diffusion creep laws........ 118

Figure 6.27. Average stress in the equivalent Cu grain model with refined mesh and the creep behavior approximated by four creep laws in the GB layer and the grain interior. 119

Figure 6.28. Stress σ_{xx} in the grain corner node A predicted by the equivalent FEA model with refined mesh and four creep laws in the GB layer and the grain interior. 119

Figure 6.29. Stress σ_{xx} in the grain center node B predicted by the equivalent FEA model with refined mesh and four creep laws in the GB layer and the grain interior. 120

Reproduced with permission of the copyright owner. Further reproduction prohibited without permission.

ABSTRACT

MODELING OF DIFFUSIONAL CREEP AND STRESS RELAXATION IN COPPER GRAINS DURING MANUFACTURING OF MICROELECTRONIC INTEGRATED CIRCUITS

by

VASYL M. GRYCHANYUK

University of New Hampshire, December 2006

The finite element technique was developed to study diffusional creep and stress relaxation in Cu grains with several atomic monolayers thick grain boundary region of enhanced diffusivity. The model was motivated by the need to study nanoscale back-end interconnect structures of microelectronic circuits. These structures have the length scale that does not conform to the assumptions of classical dimensional theories of diffusional creep.

Both diffusion and elasticity governing equations are considered in the coupled formulation of mass flow and stress analysis. Vacancy concentration field in the grains subjected to external load is coupled to stress field through diffusional creep strains. The formulation has been implemented in the commercially available finite element software package MSC.Marc.

We validated the model for the case of stress relaxation in one-dimensional grain array by comparing the finite element simulations to the predictions of classical Nabarró-Herring and Coble theories. The numerical results show good correspondence to analytical predictions, suggesting that this model may be used to predict diffusive stress

Reproduced with permission of the copyright owner. Further reproduction prohibited without permission.

relaxation in more advanced systems of practical importance, such as Cu interconnects at elevated temperatures. We have used our model to study the effect of grain size on creep rate in a polycrystal under external load. The approach has been applied to study the stress relaxation in a typical Cu-Ta-dielectric structure subjected to thermal loads.

To improve the computational efficiency of the diffusional creep modeling, we developed the numerical technique of equivalent viscoplastic finite elements. This approach was found to improve the computational efficiency by reducing the coupled elasticity-mass flow problem to the equivalent mechanical creep analysis. The predictions of the equivalent element viscoplastic model showed good correspondence to the stress relaxation results obtained with coupled elasticity-mass flow FEA approach.

Reproduced with permission of the copyright owner. Further reproduction prohibited without permission.

CHAPTER 1

INTRODUCTION

1.1. Copper interconnects in the integrated circuit technology

Interconnect lines form the back-end structure in the integrated circuit technology and distribute electric signals to various systems on a chip. An example of a Cu interconnect line is shown in Figure 1.1. The manufacturing process of Cu-damascene interconnects has become an important field of research since early 1990's. Much technological effort has been applied to reduce the feature size in accordance with the Moore's law. Currently, typical dimension of the interconnect cross-section is on the order of a 100 nm (about 400 atomic radii of Cu).

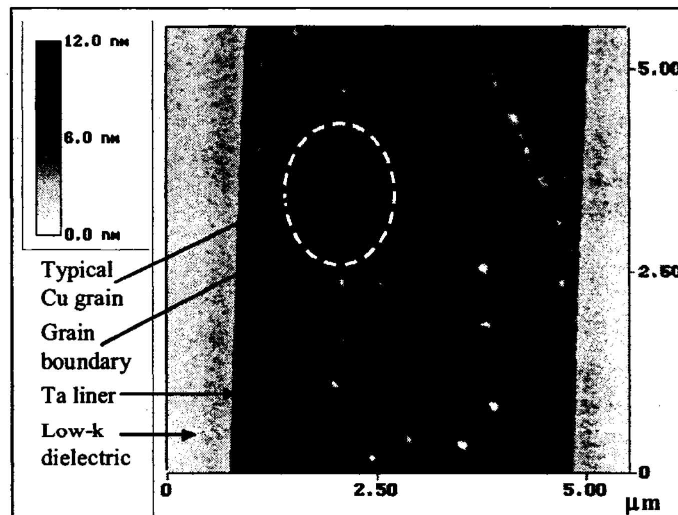

Figure 1.1. Atomic force microscope topographical map of Cu interconnect line sample supplied by IBM Corporation.

Reproduced with permission of the copyright owner. Further reproduction prohibited without permission.

As the minituarization of back-end structures continues, the interconnect signal delay time becomes a limiting factor for the integrated circuit performance. Thus copper replaced aluminum as the interconnect line material due to lower resistivity and improved signal delay characteristics. Copper interconnect lines are manufactured using the dual-damascene technique. The name "damascene" originates from Damascus, a place in Syria where ancient jewelers used similar method to deposit precious metals for ornaments. The process flow is schematically shown in Figure 1.2.

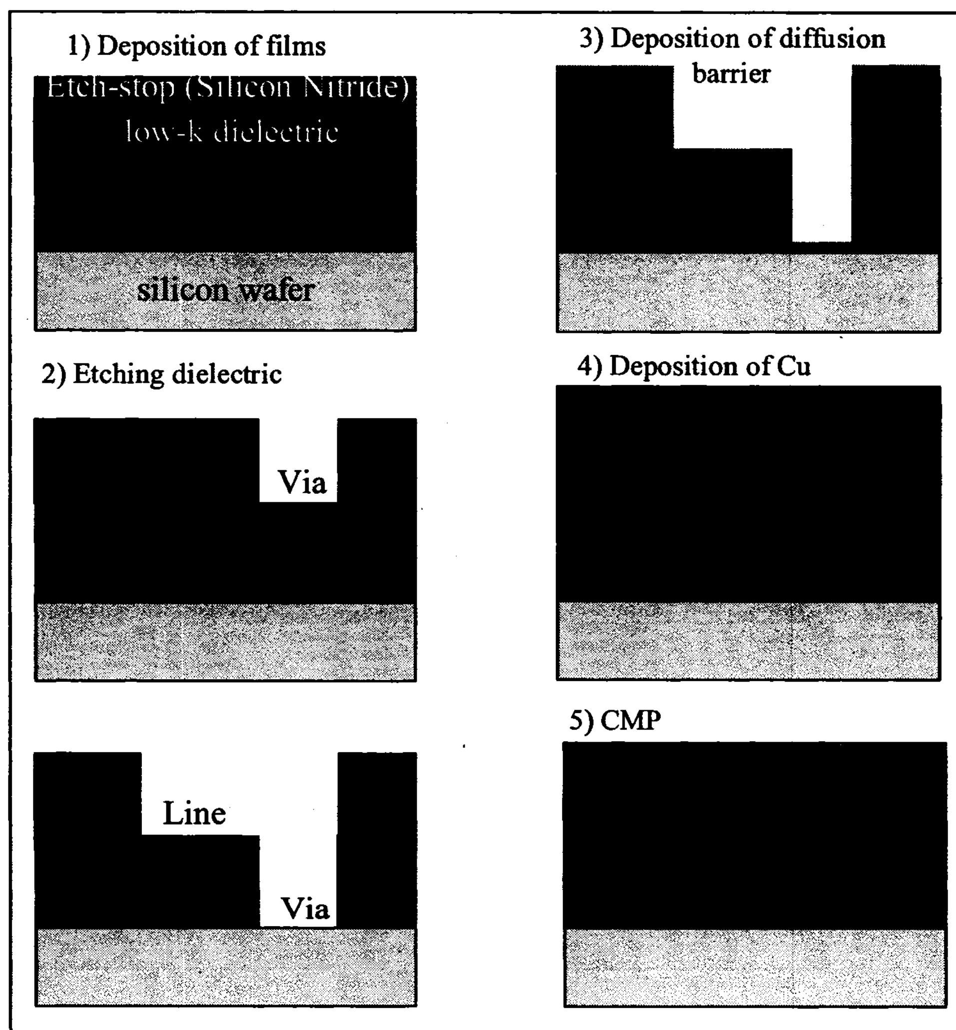

Figure 1.2. Outline of major steps in the dual damascene interconnect metallization technique.

Reproduced with permission of the copyright owner. Further reproduction prohibited without permission.

The dielectric blanket is patterned using reactive ion etching. Chemical vapor deposition or physical vapor deposition is then used to create the diffusion barrier and seed layers. Copper is deposited by filling the trenches using electroplating as the currently preferred method, according to Rathore and Chanda [1]. It is followed by chemomechanical polishing to flatten the layer and thus produce a planar layered structure. Thermal cycle from room temperature to 350-400°C is used to anneal out the device damage from the reactive ion etch. Finally, the surface is capped with a dielectric and another interconnect level is manufactured. The dual damascene technique, in which both via and line are deposited simultaneously, results in 30% fewer manufacturing steps compared to single damascene technique where lines and vias are deposited separately (see, for example, Sullivan [2]).

1.2. Failures in copper interconnects attributed to diffusional creep

The reliability issues for interconnect lines have become increasingly important after the introduction of Cu as the material of choice. For example, Cu does not have a self-passivating oxide, therefore the integrity of cap layers is vital to the reliability of integrated circuits. Other manufacturing trends that contribute to the reliability risks include the increasing density of back-end interconnect lines and the introduction of low-k dielectrics which have low Young's moduli and high coefficients of thermal expansion.

The deformed shape due to thermal strains in the typical single-level interconnect structure subjected to elevated temperatures is schematically shown in Figure 1.3. Considerable stresses develop in the interconnect lines during the thermal cycle due to the mismatch of thermal expansion coefficients between the substrate, the dielectric and the diffusion barrier (Kamsah et al. [3]). For the dielectric material, thermal stresses may

Reproduced with permission of the copyright owner. Further reproduction prohibited without permission.

result in such negative impact as thermomechanically induced cracking and adhesion loss, i.e. delamination. For the conductor, understanding of the impact of thermal stress on the reliability requires the consideration of the interconnect line length scale.

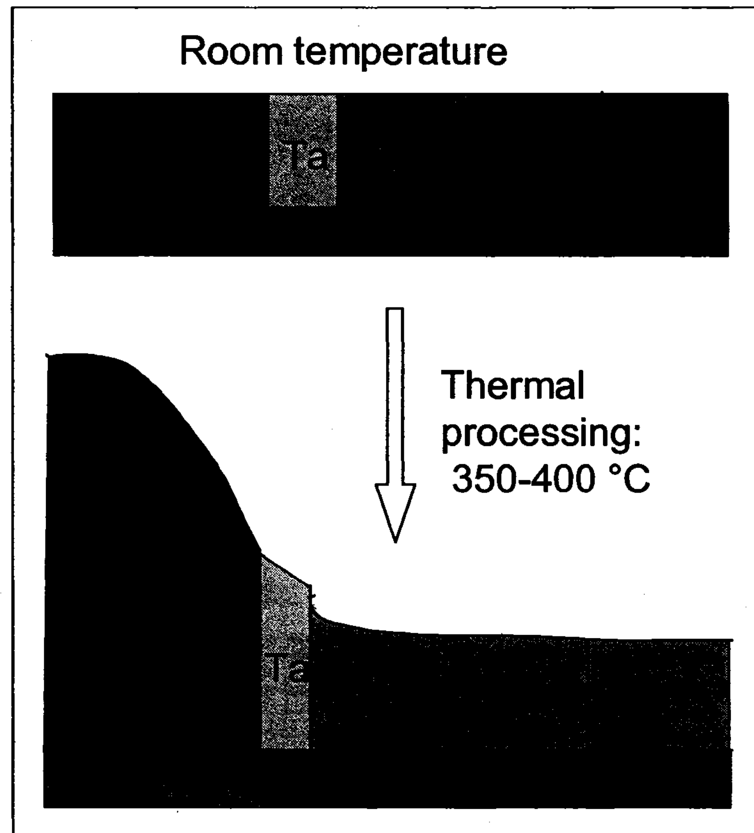

Figure 1.3. Schematic illustration of the deformed shape in a typical uncapped single-level interconnect line subjected to the elevated temperature during thermal cycle.

We may assume that dislocation activity is not relevant at interconnect size length scales and processing temperature ranges, as suggested, for example, by Kobrinsky et al. [4]. We believe that some of the failure mechanisms in Cu interconnects could be based on the phenomenon of nanoscale diffusion-based deformation. This deformation may be attributed to the Cu-Cu grain boundary and Cu-Ta interfacial sliding, as well as to the material buildup due to diffusional creep. The experimental background for this

Reproduced with permission of the copyright owner. Further reproduction prohibited without permission.

assumption was provided by Gross et al. [5], who developed an AFM method to measure out-of-plane deformation resulting from thermal cycling and applied this technique to observe the Cu-polyimide interconnect structure. Stress-induced diffusional creep mechanisms have been shown to contribute to failures in Cu interconnect structures (see, for example, Lee et al. [6], Hussein and He [7]). The coalescence of vacancies may result in the void nucleation. Further stress-driven vacancy flow contributes to the void growth which can result in the increase of line resistance or complete line failure. In this thesis we focus on the impact of the diffusional mass flow on the nanoscale deformation and the resulting transient stress relaxation.

1.3. Overview of existing approaches to the modeling of diffusional creep processes

Diffusional creep is traditionally described using the models of Nabarro, Herring and Coble [8-10]. These classical models assume that creep deformation occurs as a result of vacancy diffusion in response to stress induced vacancy concentration gradients. The Nabarro-Herring model estimates the creep rate based on vacancy diffusion through the grain bulk as defined by the diffusivity in the grain interior. The model predicts the dependence of the creep rate on the grain size d as $1/d^2$. Coble creep model extended this approach by considering the grain boundary as the only diffusion path. The activation energies for grain boundary diffusion are assumed smaller than the corresponding values in the grain interior, based on the physical concept of the grain boundaries as the regions with much faster diffusion due to less regular atomic structure. The model predicts $1/d^3$ creep rate dependence on grain size. Both Nabarro-Herring and Coble theories present dimensional models lumping grain geometry into linear constants and focusing on the

Reproduced with permission of the copyright owner. Further reproduction prohibited without permission.

dependence of creep rate on grain size, temperature and stress for a polycrystalline material. The constitutive (creep strain rate vs stress) equations are derived for both models using the assumptions that the grains of idealized square shape are loaded as shown in Figure 1.4, and the behavior of an individual grain is representing the behavior of a polycrystal. Note that although Nabarro-Herring and Coble models are widely accepted to describe the diffusional creep phenomena, the experimental verification of diffusional creep has been a subject of debates in the literature [11-13]. Recent reviews of the mechanisms and models of diffusional creep/plasticity are presented in [14-16].

Several investigators have used the principles of these models, namely vacancy migration in response to stress gradients, to predict stress relaxation in discrete structures. Gao et al. [17] modeled grain boundary (GB) diffusion in polycrystalline thin metal films through introduction of crack-like boundary wedges which evolve by the transport of material from free surface along the grain boundary. Their analysis assumed no surface diffusion and grain boundary grooving in the films subjected to in-plane stresses. This model was applied to study the deformation of thin Cu films in the works of Weiss et al. [18] and Buehler et al. [19].

The impact of stress-driven diffusion on GB sliding was studied in the classical paper of Raj and Ashby [20]. More recent efforts to model diffusion-accomodated GB sliding and grain rotation were presented in [21-23]. Experimental and numerical modeling of GB sliding was provided by Kamsah [24]. Dutta et al. [25] introduced a shear lag model to study the diffusional creep/plasticity and GB sliding in Cu interconnect lines.

Reproduced with permission of the copyright owner. Further reproduction prohibited without permission.

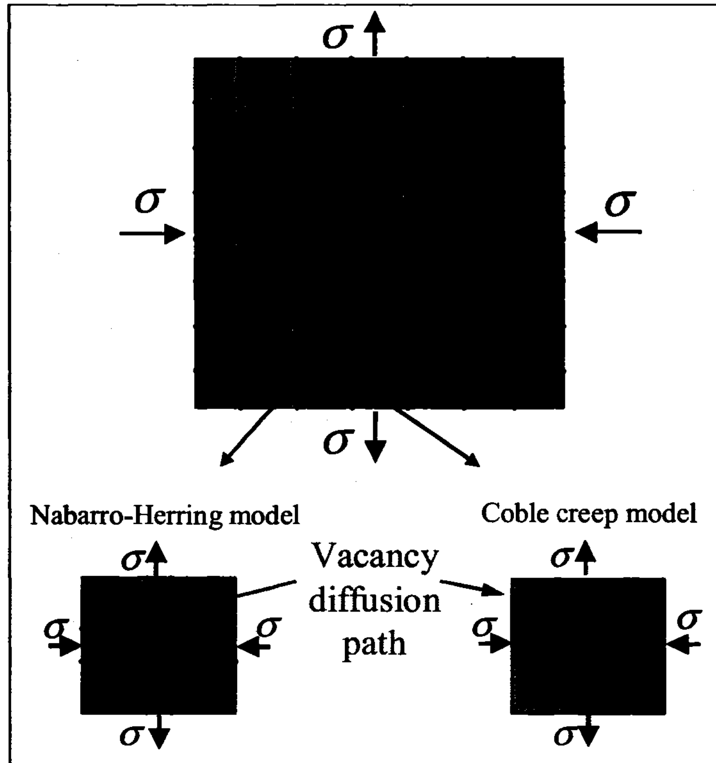

Figure 1.4. Nabarro-Herring and Coble diffusional creep models.

Garikipati et al. [26] presented advanced coupled formulation of the vacancy concentration and elasticity problems in polycrystalline solids. Their model was applied to array of square grains and they considered the variation of vacancy formation energy over the finite width of GB region. While the formulation of their model accurately captures the physics of the problem, their example used unrealistically thick GB regions (100 nm vs typical thicknesses of ~1 nm corresponding to 3-4 Cu monolayers).

The work of Bower and coworkers represents one of the most long-term and comprehensive efforts to model inelastic deformation in interconnects. The finite element formulation developed by Bower and Craft [27] addressed stress driven interface diffusion, electromigration and void growth using the concept of sharp grain boundaries. The stress field evolution was assumed to be caused by separation between grains due to

Reproduced with permission of the copyright owner. Further reproduction prohibited without permission.

material deposited on or removed from grain boundary. Zhang et al. [28] extended the formulation to a 3D model that accounts for strain and electromigration-induced surface diffusion. They implemented their formulation into a finite element program and performed simulations to analyze evolution of voids in idealized interconnects and surface roughening of thin films. Recent work of Singh et al. [29] employs a similar formulation to model stress relaxation in copper damascene structure and to estimate the diffusivities along interfaces. The effect of passivation layer on stress relaxation and the corresponding experimental estimate of GB diffusivity was also provided by Gan et al. [30].

The modeling effort described above is based on the continuum treatment of nanoscale diffusion creep deformation. The alternative approach is to predict the deformation by modeling the motion of individual atoms. The major techniques of atomistic simulation are lattice statics, lattice dynamics, Monte-Carlo and molecular dynamics. Many authors including Swygenhoven et al. [31], Shiotz et al. [32], Wolf et al. [33] applied molecular dynamics methods to model nanoscale deformation. The biggest advantage of atomistic modeling is the ability to gain insight into the atomic-level structure and thermomechanical deformation behavior. In addition, it is convenient to model large inelastic deformations which would require remeshing in continuum FEA treatment. However, atomistic approach has several limitations. Most importantly, the maximum grain size that can be modeled with molecular dynamics is dictated by computer capacity and speed. Current supercomputers are capable of handling the simulation cells that contain several millions of individual atoms. For example, the computer that allows to run the simulation for one million atoms of copper is able to

Reproduced with permission of the copyright owner. Further reproduction prohibited without permission.

model the cubic simulation cell of approximately 22.8 nm lateral size. In addition, the requirement of small time steps to track the atomic motion limits the time period for molecular dynamics simulations. The number of time steps typically does not exceed 10^7 which results in the modeling time window ~10 ns [33]. To model nanoscale deformation during this time period, it is necessary to consider the simulation cells with artificially high strain rate by applying large external stress. Although it was argued [34] that high strain rate molecular dynamics computations are close to Coble creep theoretical predictions, the atomistics simulations are deformation rate dependent, therefore care must be taken to select the applied stress and time step to adequately model nanoscale deformation during the short time period. The next important concern is empirical or semiempirical nature of interatomic potentials which may not precisely describe the atomic bonds and forces.

Other modeling efforts which consider diffusion processes in polycrystalline metals include the studies of stress-induced diffusive fracture by Guo et al. [35] and triple junction diffusion by Fedorov et al. [36]. One of the first modeling efforts of surface diffusion which contributes to the GB grooving was presented in the classical paper of Mullins [37]. More recent GB grooving, surface diffusion and interface motion modeling includes the work of Thouless [38] and Sun and Suo [39]. Cocks and Gill [40] presented the variational formulation to describe the grain growth. Pan et al [41] introduced the FEA approach to model the grain boundary grooving and grain interface migration due to coupled grain boundary and surface diffusion mechanisms. Their approach is based on the classical treatment of GB diffusive cavitation by Needleman and Rice [42]. This

Reproduced with permission of the copyright owner. Further reproduction prohibited without permission.

model is applied to study the diffusion-based evolution of voids in Cu polycrystals. Modeling of voids in polycrystalline materials was also investigated in [43-45].

We believe that it is inappropriate to use dimensional models for polycrystalline behavior of structures that are 1-2 grain diameters wide and have dimensions of 100 nm or less. The complex stress state in each individual grain and geometrical constraints of the problem necessitate the finite element solution. The work of Rzepka et al. [46] is one of the successful applications of commercially available software to predict diffusive flow in Al(Cu) lines due to gradients in stress, electric potential, temperature and surface curvature. We believe that it is desirable to employ commercial finite element codes to tackle these potentially numerically unstable transient processes. In this thesis, we employ the FEA package MSC.Marc to study the diffusion-based mechanical response of Cu interconnects to thermomechanical loads.

1.4. Objective and scope

In this thesis, we present the model of diffusion-accommodated creep in Cu grains that has the unique feature of a finite thickness grain boundary region with enhanced diffusivity. This approach is somewhat similar to the theoretical framework of Garikipati et al. [26] that includes the concept of finite thickness GB region with reduced vacancy formation energy. However, the consideration of enhanced diffusivity in GB region enables us to estimate the impact of interface roughness, interface impurity, deposition conditions, and feature size on stress relaxation in nanoscale interconnect structures. Since diffusion of vacancies in the region adjacent to grain boundary is thought to be faster than in the bulk, it is expected to have a prominent effect on stress relaxation for nanoscale grains and structures. We compare our numerical predictions for stress

Reproduced with permission of the copyright owner. Further reproduction prohibited without permission.

relaxation and creep in a simple structure to the analytical predictions of Nabarro-Herring and Coble. Commercial FEA software MSC.Marc is employed to make the computations tractable. Some concepts of our numerical technique were presented in [47]. We explore the possibility to enhance the formulation and introduce purely mechanical FEA treatment that captures the stress-strain response to the diffusional vacancy flow process in Cu polycrystalline material. This can be done by incorporating the numerically obtained effective creep laws into the mechanical finite element stress analysis.

To provide the mechanical formulation of creep process, it is required to specify a creep law as a material property. The available diffusional creep law expressions of Nabarro-Herring and Coble classical theories are based on the assumptions of the idealized square grain geometry. In addition, these expressions are derived assuming the orthogonal compressive and tensile externally applied loads. Although it is not possible to obtain the diffusion creep law in a closed-form for the general case of grain geometry and external load, we note that numerical techniques can be developed to approximate such general creep laws as a material property for arbitrary grains. The resulting purely mechanical simulations provide a considerable increase of computational efficiency compared to the coupled elasticity-mass flow model. Therefore, an attempt is made in this dissertation to obtain numerically the effective creep laws which approximate the diffusion behavior within Cu grains. The equivalent creep laws are computed using the coupled elasticity-mass flow formulation developed in this dissertation. The modeling of nanoscale deformation is then performed by incorporating the numerically obtained effective creep laws into the mechanical finite element stress analysis.

Reproduced with permission of the copyright owner. Further reproduction prohibited without permission.

The numerical predictions of the coupled elasticity-mass flow model were obtained for the grain geometry and external loading that correspond to the assumptions of classical diffusion creep theories. We found that the predictions are close to Nabarro-Herring and Coble theories for small values of grain size. It may be concluded that the coupled formulation presented in this thesis and the equivalent viscoplastic finite element technique developed on its basis may serve as a numerical extension of classical theories. The proposed technique relaxes several assumption of classical theories at the expense of the requirements for numerical computations and the calibration of model parameters such as GB region thickness. First, this technique relaxes the assumption of square geometry, allowing to consider the grain of arbitrary shapes. Second, the technique allows to model the grains subjected to arbitrary externally applied loading. Another assumption of the classical theories which is relaxed in our formulation is the pre-defined vacancy diffusion path. Although we found that creep behavior varies throughout the grain and needs to be represented by more than one creep relation, the technique provides the convenience of specifying the creep behavior as a material property in a mechanical finite element procedure.

The outline of the thesis is as follows. In Chapter 2 we present the thermodynamic basis for equilibrium vacancy concentration analysis. The vacancy diffusion problem is then coupled to elasticity formulation through creep strains computed from vacancy fluxes. Chapter 3 presents the finite elements formulation as well as the details of its numerical implementation. The attempts to reduce the computation time using the mesh refinement multipoint constraints and time series extrapolation are also described. We validate the numerical approach in Chapter 4 by modeling the stress relaxation in one-

Reproduced with permission of the copyright owner. Further reproduction prohibited without permission.

dimensional linear array of square grains. We compare the numerical predictions for the stress relaxation in the periodic square grain array to the analytical estimates based on Nabarro-Herring and Coble models. The effect of grain size on the diffusional creep response is studied using the model of 3x3 grain array subjected to externally applied stress. In Chapter 5 we present the model of a typical Cu-Ta-dielectric structure to illustrate the application of the technique to stress relaxation in interconnect structures subjected to thermal loads during manufacturing. The numerical results are compared with analytical predictions based on Nabarro-Herring and Coble mechanisms. Chapter 6 presents our effort to develop the numerical technique of equivalent viscoplastic finite elements to improve the efficiency of the diffusional creep modeling. Numerical experiments were performed to explore the creep behavior in various areas throughout the grain. Numerically obtained creep laws were then applied to the modeling of the stress relaxation in Cu grain assembly using the equivalent FEA creep analysis.

Reproduced with permission of the copyright owner. Further reproduction prohibited without permission.

CHAPTER 2

COUPLED FORMULATION OF TRANSIENT ELASTICITY-VACANCY DIFFUSION PROBLEM

The purpose of this chapter is to present the physical and mathematical formulation of the model for stress-driven mass flow in metals. This model must be able to predict both the vacancy diffusion as well as the thermomechanical stresses and strains that arise when modeled structures are subjected to elevated temperatures. The gradients in the stress field create the driving forces for mass flow which result in diffusional creep strains. These strains change geometry and affect the subsequent evolution of the stress field. This highly interdependent multiphysics process requires the coupled mathematical formulation that takes into account both diffusion and elasticity governing laws. The target implementation of the model presented in this chapter is the commercial software package MSC.Marc available in the Mechanical Engineering Department of the University of New Hampshire under the academic license.

Note that the diffusive mass flow occurs under certain ranges of stress, temperature and characteristic size of the structure in question, thus the important role of this chapter is to clearly outline the assumptions, limitations and ranges of applicability for the proposed model. In subsequent chapters, we will validate the model for idealized cases of grain assemblies and then apply the model to typical Cu interconnect structures.

Reproduced with permission of the copyright owner. Further reproduction prohibited without permission.

2.1. Equilibrium vacancy concentration and stress-induced mass flow

We develop the model which predicts inelastic deformations that arise from vacancy diffusion. The diffusivity of vacancies is defined by the frequency of attempts of an atom to jump into a neighboring vacancy site times Boltzmann factor $\exp(-Q_m/kT)$, which is essentially a probability that the atom's energy at temperature T is no less than activation energy for vacancy motion Q_m. We assume that the kinetics of species in a material is governed by Fick's law and vacancy fluxes are driven by vacancy concentration gradients. Physically the presence of vacancies is strongly dependent on the stress state. Vacancy formation is associated with broken bonds and the increase in internal energy and configurational entropy. To consider these effects, vacancy concentration is defined as minimum of Gibbs free energy according to the traditional treatment of equilibrium thermodynamics. In the model presented here the role of grain boundaries is emphasized as infinite sources/sinks of vacancies. Furthermore, the finite thickness regions adjacent to grain boundaries are treated as the regions of enhanced diffusivity.

2.1.1. Thermodynamic approach to equilibrium vacancy concentration

Thermodynamic relation between stress and the equilibrium concentration of vacancies C_v^{eq} is one of the key components for modelling of stress-driven diffusional mass flow. Porter and Easterling [48] provided the Arrhenius-type relation between atomic volume Ω, stress-free vacancy concentration C_0, temperature T, mean stress σ_h and C_v^{eq} in bulk metals

Reproduced with permission of the copyright owner. Further reproduction prohibited without permission.

$$C_v^{eq} = C_0 \exp(\sigma_h \Omega / kT) \qquad (2.1)$$

where k is the Boltzmann constant. This formula is obtained by considering the phase equilibrium of a solid in which the only two phases are material atoms and vacancies. The Gibbs free energy ΔG of such a solid can be written for dilute vacancy concentration C_v as

$$\Delta G = N_v \Delta G_v + kT(N_a \ln C_A + N_v \ln C_v) \qquad (2.2)$$

In this expression, N_a is number of atoms, N_v is number of vacancies, $C_A = 1 - C_v$ and ΔG_v is the Gibbs free energy of vacancies in a solid. Energy ΔG has a minimum at equilibrium, thus C_v^{eq} is obtained by minimizing ΔG with respect to N_v

$$C_v^{eq} = \exp(\Delta G_v / kT) \qquad (2.3)$$

The Gibbs free energy of vacancies ΔG_v is related to the enthalpy and entropy of vacancy formation ΔH_v and ΔS_v as $\Delta G_v = \Delta H_v - T\Delta S_v$. The estimate of ΔS_v for Cu is typically given in the literature as $\exp(\Delta S_v / k) \cong 3$. The enthalpy of vacancy formation is understood as the sum of energy of vacancy formation Q_f and the work required to create a vacancy that occupies atomic volume Ω

$$\Delta H_v = Q_f + \sigma_h \Omega \qquad (2.4)$$

It is important to understand the role of stress σ_h in Eqs. (2.1) and (2.4) to adequately model the stress-driven mass flow. The classical thermodynamics treatment presented so far assumed uniform properties of stress and vacancy concentration throughout a system. Conceptually, the process of vacancy creation/annihilation occurs throughout the grain and vacancy concentration is defined by the Boltzmann probability

Reproduced with permission of the copyright owner. Further reproduction prohibited without permission.

that energy in a point is no less than activation energy for vacancy generation, in this case $\sigma_h\Omega$ according to Eq.(2.1). However, we must depart from this assumption if we desire to model mass flow process which is driven by vacancy concentration gradients. The need for an alternative assumption can be illustrated by the idealized model of square grain solid subjected to uniform remotely applied load. Since there are no mean stress gradients in this example, the vacancy concentration gradients that drive Nabarro-Herring and Coble creep should not exist in this model. To account for the gradients in vacancy concentration, the theories developed by Nabarro, Herring and Coble [8-10] assumed that the equilibrium concentration in the region adjacent to the grain boundary is defined by σ_n, the stress normal to the boundary. This implicit assumption of classical diffusional creep theories is consistent with the physical description of the process of vacancy creation/annihilation, which can only take place at grain boundaries and not in the grain interior. With grain boundaries acting as vacancy sources/sinks, the vacancies are introduced or removed in the presence of a local normal traction σ_n. The qualitative difference in concentration fields produced by σ_h and σ_n is illustrated in Figure 2.1. Assuming that the vacancy concentration depends on σ_n, higher vacancy concentration is predicted at the grain boundaries with tensile normal traction as compared to the grain boundaries with compressive normal traction.

In what follows we assume that the local enthalpy of vacancy formation is $\Delta H_v = Q_f + \sigma_n\Omega$ which is consistent with the implicit assumptions of Nabarro, Herring, and Coble. Defining the temperature dependent stress-free vacancy concentration as

$$C_0 = \exp\left(\left(T\Delta S_v - Q_f\right)/kT\right) \cong 3\exp\left(-Q_f/kT\right) \qquad (2.5)$$

Reproduced with permission of the copyright owner. Further reproduction prohibited without permission.

we arrive at the following equation for local equilibrium vacancy concentration in grain boundary vacancy source/sink sites

$$C_v^{eq} = C_0 \exp(\sigma_n \Omega / kT) \tag{2.6}$$

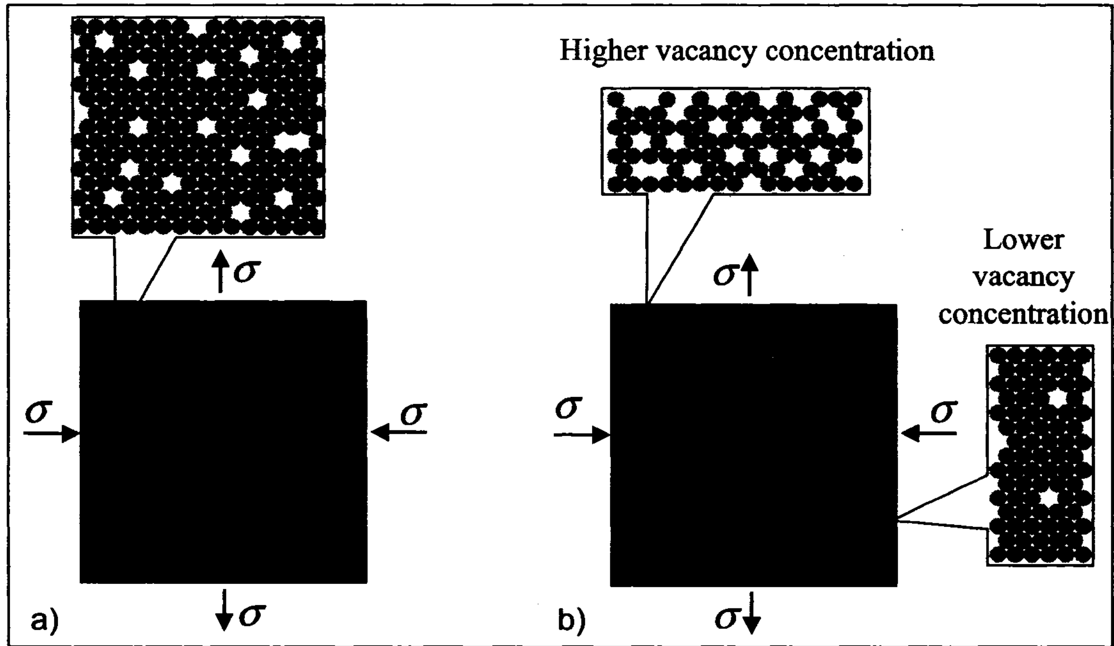

Figure 2.1. Qualitative illustration of equilibrium vacancy concentration defined by a) mean stress σ_h and b) traction σ_n normal to grain boundary.

Note that we ignore the contribution of dislocations in the grain interior as vacancy sources and sinks since they are rarely observed for nanoscale grains (see Kong et al. [14] and references therein). This assumption will still allow the applicability of our model to high density interconnect structures, since dislocation activity may not be relevant at interconnect size scales and processing temperature ranges, as suggested, for example, by Kobrinsky et al. [4]. Nevertheless, dislocations may be present at grain boundaries due to disordered atomic arrangement at grain interfaces which arises from misorientation of neighboring grains. Vacancy creation/annihilation at the grain boundary

Reproduced with permission of the copyright owner. Further reproduction prohibited without permission.

may result in the extension/contraction of dislocation atomic half-planes, causing the lattice planes to be created or destroyed by vacancy movement that results in lattice drift. Our model assumes the absence of lattice drift for the sake of simplified treatment.

2.1.2. Kinetics of stress-induced mass flow

The differences in vacancy concentration lead to vacancy fluxes $\mathbf{j}_v$. This is shown schematically in Figure 2.2 for the example case when horizontal compressive and vertical tensile stresses are externally applied to the idealized square grain. The vacancy fluxes obey the Fick's constitutive equation

$$\mathbf{j}_v = -D_v \nabla C_v \tag{2.7}$$

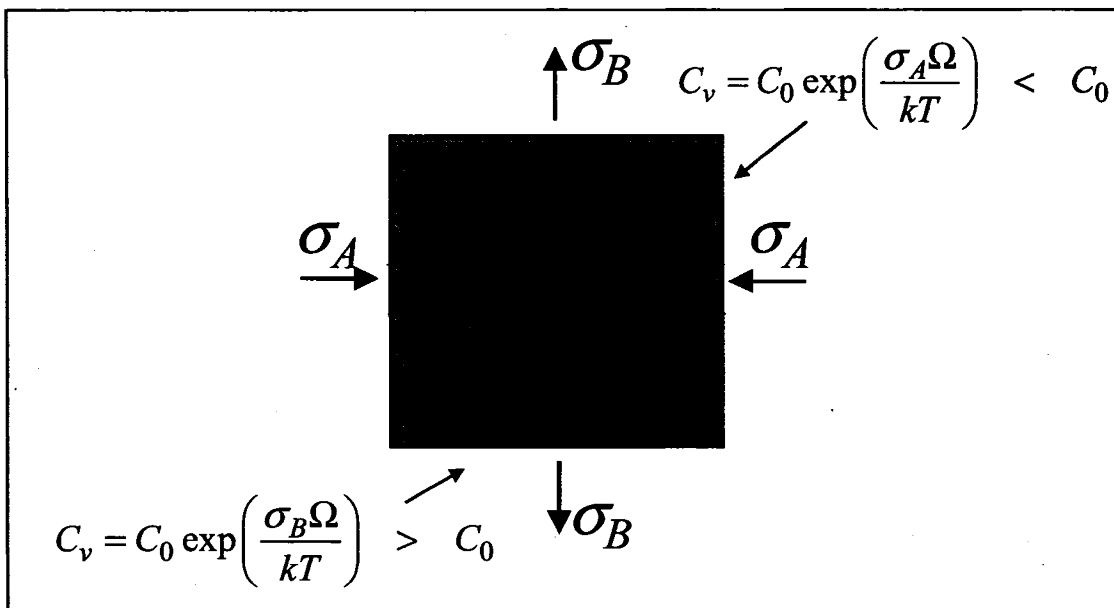

Figure 2.2. Vacancy fluxes due to concentration gradients within a grain.

The vacancy diffusivity in grain interior is given by $D_{v,L} = D_{0L} \exp\left(-Q_{m,L} / kT\right)$ where $Q_{m,L}$ is the activation energy for vacancy motion. We assume that $Q_{m,L}$ is less in a

Reproduced with permission of the copyright owner. Further reproduction prohibited without permission.

region adjacent to the grain boundary due to disorder near the interface and reduced elastic constraint. We choose the thickness of the enhanced diffusivity region as 3-4 atomic monolayers as schematically shown in Figure 2.3.

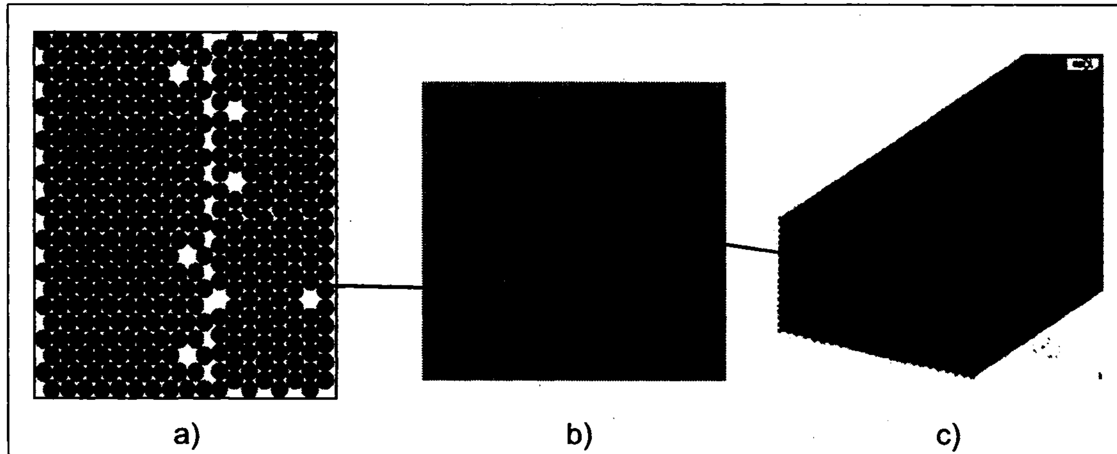

Figure 2.3. Schematic illustration of the enhanced diffusivity region at grain boundaries

We define the vacancy diffusivity at interfaces as $D_{v,gb} = D_{0gb} \exp\left(-Q_{m,gb}/kT\right)$ where $Q_{m,gb} = \alpha Q_{m,L}$ $(\alpha < 1)$. This reduction of activation energy for vacancy motion at grain boundaries and free surfaces has been postulated by Frost and Ashby [49]. We are not aware of a precise method to measure the activation energy for vacancy motion through the grain boundary and will treat it as an adjustable parameter that may be affected by impurities, grain boundary roughness, crystallographic orientation and whether the opposing interface has similar diffusivity. The selection of coefficient α dramatically affects the value of diffusivity in finite thickness grain boundary region, as shown in Figure 2.4 for $D_{0L} = D_{0gb} = 2.0 \cdot 10^{-5}\ m^2/s$, $Q_{m,b} = 109.7\ kJ/mol$.

The vacancy flow is governed by the following conservation law

Reproduced with permission of the copyright owner. Further reproduction prohibited without permission.

$$\frac{\partial C_v}{\partial t} + \nabla \cdot \mathbf{j}_v = 0 \tag{2.8}$$

Assuming that only vacancy defects are present in the polycrystal, the mass flow occurs by jumping of atoms into nearby empty lattice sites. The vacancy flux $\mathbf{j}_v$ and atomic flux $\mathbf{j}_a$ are related as

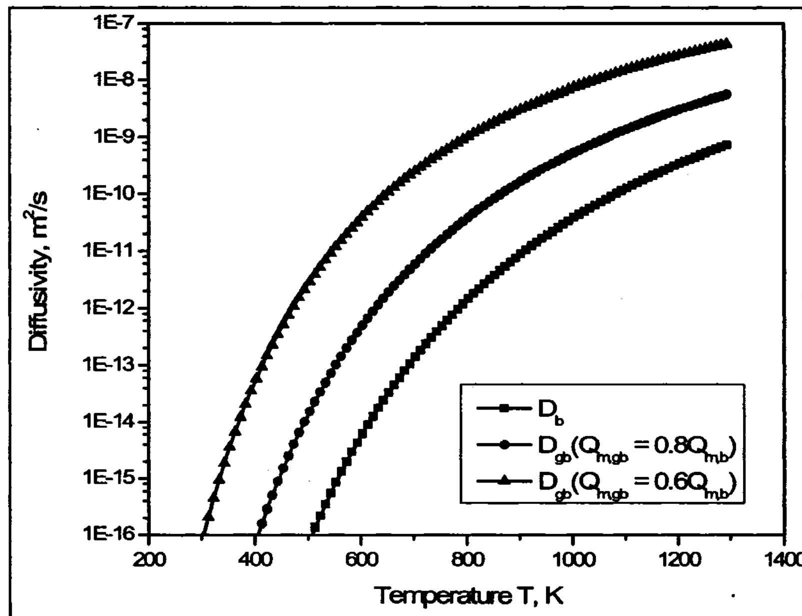

Figure 2.4. The enhancement of diffusivity in grain boundary region due to the reduction of the activation energy for vacancy motion.

$$\mathbf{j}_a = -\mathbf{j}_v \tag{2.9}$$

Atomic flux is responsible for the inelastic deformation and stress relaxation that occurs in Cu grains.

Reproduced with permission of the copyright owner. Further reproduction prohibited without permission.

2.2. Coupled governing equations of elasticity and vacancy diffusion

The purpose of the model introduced here is to predict diffusional creep and stress relaxation, which can occur in a body subjected to prescribed displacements or tractions. Usually, in stress relaxation problems, fixed displacement boundary condition is preserved throughout the simulation, while fixed traction applied to the boundary must be held constant to model creep.

Due to the diffusive nature of inelastic deformation, it is necessary to consider a coupled problem of vacancy diffusion and elasticity to track both the mass flow and the evolution of displacements and stresses. We have considered two scenarios of coupled formulation to account for this phenomenon. The first scenario considers coupling through vacancy fluxes. The second way to formulate the coupled problem is through diffusional creep strains. The results of both approaches are approximately identical, however the second approach is preferred because it allows to reduce the computation time.

We note that the formulation proposed here is based on the physical nature of diffusional creep process and does not assume any phenomenological relations between stresses and diffusional creep strains.

2.2.1. Coupling through grain boundary vacancy flux

We consider a solid under the following boundary conditions applied at time $t = 0$

$$\mathbf{u} = \mathbf{u}_0, \quad \mathbf{x} \in \Omega_u \tag{2.10}$$

$$\boldsymbol{\sigma} \cdot \mathbf{n} = \mathbf{t}_0, \quad \mathbf{x} \in \Omega_s \tag{2.11}$$

Reproduced with permission of the copyright owner. Further reproduction prohibited without permission.

where Ω_u and Ω_s are the parts of the boundary with prescribed displacements $\mathbf{u}_0$ and tractions $\mathbf{t}_0$. We assume that the initial application of boundary conditions (2.10) or (2.11) results in a purely elastic response. For the elastic stress and strain fields $\boldsymbol{\sigma}$ and $\boldsymbol{\varepsilon}$, the traditional set of governing equations is valid

$$\nabla \cdot \boldsymbol{\sigma} = 0 \tag{2.12}$$

$$\boldsymbol{\varepsilon} = \frac{1}{2}\left(\nabla \mathbf{u} + \nabla \mathbf{u}^T\right) \tag{2.13}$$

$$\boldsymbol{\sigma} = \mathbf{C} : \boldsymbol{\varepsilon} \tag{2.14}$$

where $\mathbf{C}$ is the elastic stiffness matrix. Note that Eq. (2.12) is written assuming the absence of body forces and Eq. (2.13) assumes small elastic strains.

We now discuss the approach to couple the elasticity formulation (2.12)-(2.14) and the vacancy flow problem governed by Eqs. (2.7)-(2.8). The idea of such coupling is to consider the effect of vacancy flow on inelastic strains and corresponding stress field. Introducing the notation $\mathbf{u}^{cr}$ for diffusion mass flow displacement, we propose to treat the atomic flux field $\mathbf{j}_a$ as the mass flow velocity field $d\mathbf{u}^{cr}/dt$ in the interior of a body that is statically fixed. Thus, we arrive to the equation

$$\frac{d\mathbf{u}_{cr}}{dt} = -\mathbf{j}_v \tag{2.15}$$

Equations (2.6) and (2.15) represent the coupling between the mass flow problem and mechanical problem. It is important to note that this method of coupling does not give explicit mathematical relation between the field variables of elasticity problem, such as elastic displacement $\mathbf{u}$, stress $\boldsymbol{\sigma}$, elastic strain $\boldsymbol{\varepsilon}$, and the field variables of vacancy flow problem, such as vacancy concentration C_v and vacancy flux $\mathbf{j}_v$. Taking into

Reproduced with permission of the copyright owner. Further reproduction prohibited without permission.

consideration the transient nature of the process, it is necessary to solve each of the boundary value problems independently on each time step while holding the variables of the other subproblem fixed, i.e. apply the so-called staggered procedure.

We start by assuming that at time $t = 0$ the concentration field is uniform and corresponds to zero stress. Note that some authors argue that stress-free vacancy concentration is higher in grain boundary regions, which may be attributed to segregation of vacancies in grain boundary regions to achieve equilibrium (see, for example, Garikipati et al. [26]). After the external boundary conditions (2.10) or (2.11) are applied, the vacancy concentration gradient leads to diffusive flow and accumulation or depletion of material in grain boundary regions, as shown schematically in Figure 2.5 for the case of horizontal compression. We assume that the accumulation of displacements caused by mass flow occurs in so-called "unloaded" configuration shown with dashed lines in Figure 2.5. This assumption is introduced for the purpose of tracking the stress relaxation due to mass flow. By reapplying boundary conditions to the "unloaded" configuration, the mass flow velocity field given by Eq. (2.15) will affect the evolution of stress field in the model. It is important to note that the coupling equations (2.15) and (2.6) do not ensure the evolution of stress field, hence it is necessary to keep track of unloaded configuration throughout the simulation.

Reproduced with permission of the copyright owner. Further reproduction prohibited without permission.

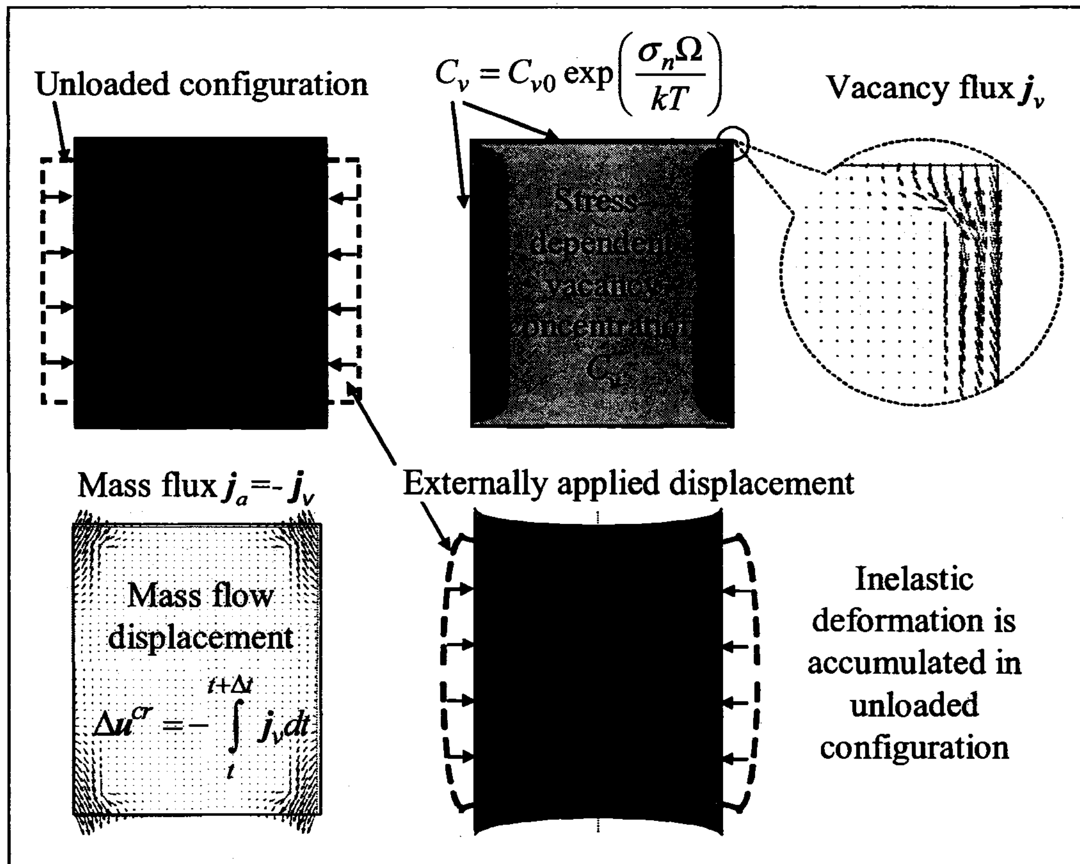

Figure 2.5. Simulation sequence performed on each time step. Elastic loading is followed by the solution of transient concentration problem resulting in the accumulation of diffusional creep displacements in the unloaded configuration.

The following sequence is performed on each time step:

1) The mechanical boundary conditions are applied, and the elasticity subproblem is solved to obtain the distribution of elastic stresses and strains, as well as the deformed shape of the solid.

2) The deformed shape obtained on the previous step is used as a domain to run the transient mass flow subproblem. The concentration boundary conditions are obtained from the coupling relation Eq. (2.6).

Reproduced with permission of the copyright owner. Further reproduction prohibited without permission.

3) The vacancy flux, obtained from transient mass flow subproblem, is integrated to give the displacements due to mass flow. We accumulate the mass flow deformations by applying these displacements to the original unloaded domain.

We then return to the first step of the sequence and obtain the deformed shape by applying the boundary conditions to the unloaded domain and enforcing the compatibility constraints between individual grains to ensure the continuity of deformed configuration. It is important to specify consistently the compatibility constraints in case of a body that contains several grains. This is schematically illustrated in Figure 2.6 for two neighboring grains. The accumulation/depletion of mass occurs in the neighboring grains leading to the formation of "gaps" or "overlaps" in unloaded configuration. The purpose of compatibility constraints is to account for such mass accumulation/depletion for

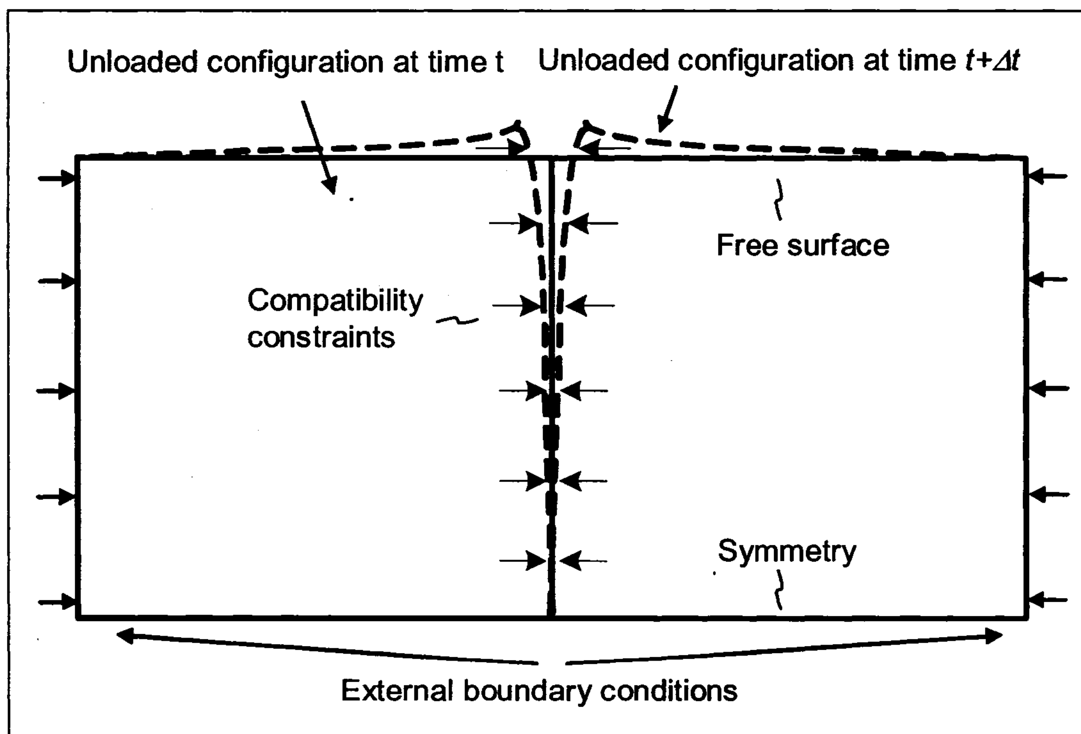

Figure 2.6. Schematic illustration of compatibility constraints that need to be applied in addition to external boundary conditions in a body that contains several neighboring grains.

Reproduced with permission of the copyright owner. Further reproduction prohibited without permission.

neighboring grains at the time the unloaded configuration is subjected to external boundary conditions (2.10)-(2.11) on each time step. The process is repeated for the prescribed number of steps to predict the time evolution of stress field and inelastic deformations.

Equation (2.15) provides the velocity field associated with mass flow in the grain interior. Further assumptions need to be introduced to define the relation of mass flux to mass flow velocity at grain boundaries. The velocity normal to the interface is the variable that reflects the mass accumulation/depletion and affects the stress relaxation or creep.

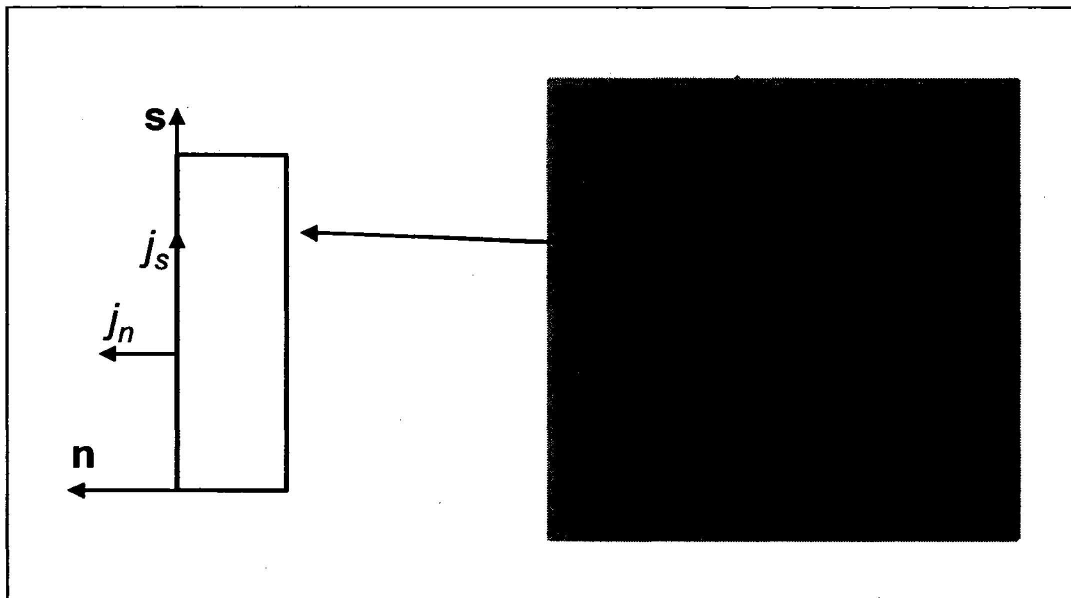

Figure 2.7. Normal and tangent components of surface vacancy flux at a grain boundary.

Let us consider normal and tangent components j_n and j_s of surface vacancy flux shown schematically in Figure 2.7. The velocity of mass flow normal to the grain boundary surface is derived from mass conservation written for the surface element [50].

Reproduced with permission of the copyright owner. Further reproduction prohibited without permission.

The velocity is affected by the divergence of flux tangent to the grain boundary and the component of vacancy flux normal to the grain boundary

$$u_{cr,n} = \left(\frac{\partial \mathbf{u}_{cr}}{\partial t} \right)_n = -\left(j_n + \frac{\partial j_s}{\partial s} \right) \tag{2.16}$$

To simplify the coupling of inelastic displacements to GB vacancy flux, we may assume that $u_{cr,n} \cong -j_n$.

We note that mass flow and resulting stress relaxation occurs in current loaded configuration. Hence the introduction of "unloaded" configuration is an artificial assumption which is necessary to implement the transient coupled formulation, when coupling is done through vacancy fluxes. The artificial nature of this concept leads to implementation difficulties illustrated here for the body consisting of several grains. In this case, the difficulties arise, which are associated with keeping track of unloaded configuration. The total elastic displacement will be a superposition of displacement arising from each individual compatibility constraint, as depicted in Figure 2.8. The compatibility constraints for this case need to be specified in the local coordinate system relative to each grain to obtain current loaded configuration from updated unloaded configuration.

Note that we limit ourselves to the small strains theory, and account for finite deformation by adjusting the shape of the domain. More rigorous formulation of the algorithm would account for large deformation and require computation of finite strain tensor.

Reproduced with permission of the copyright owner. Further reproduction prohibited without permission.

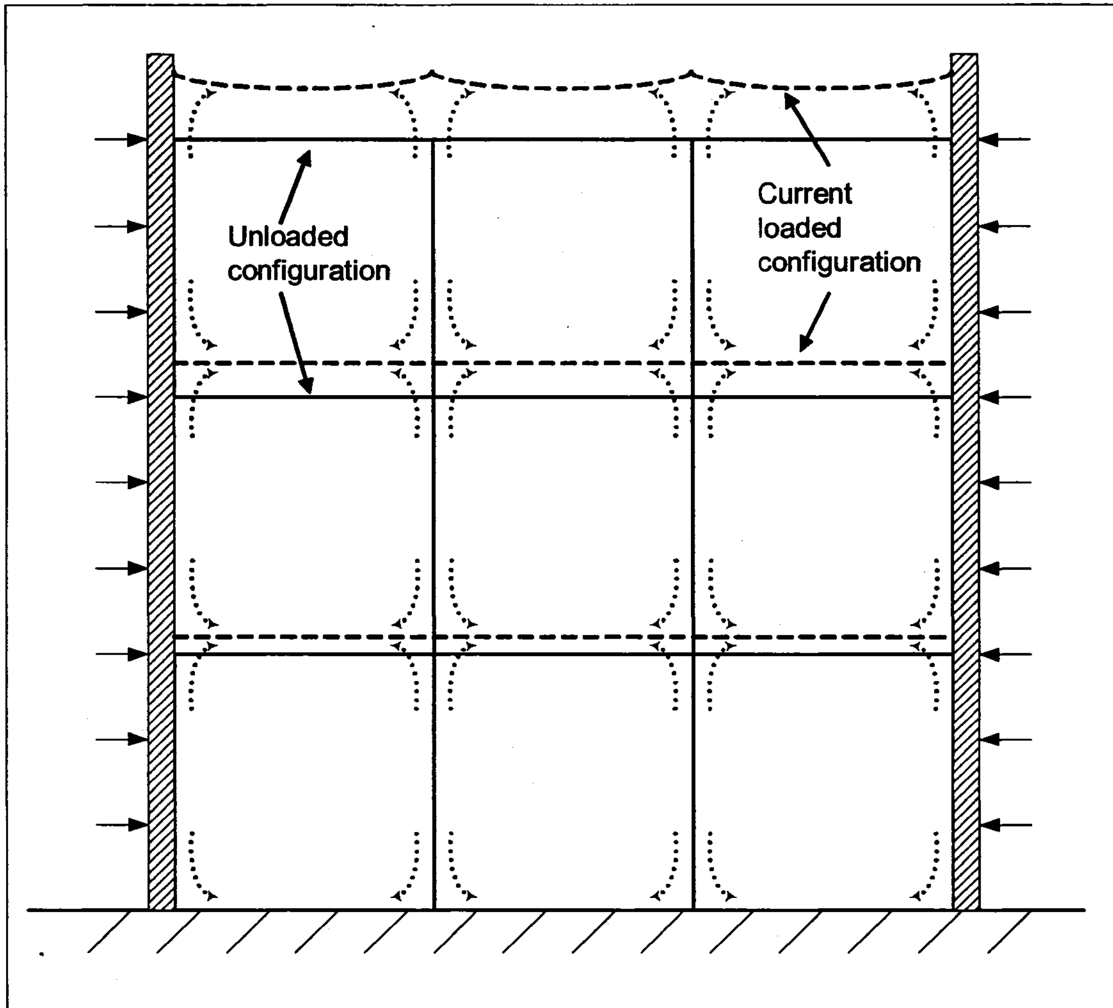

Figure 2.8. Unloaded and current loaded configurations for a body that contains multiple grains.

2.2.2. Coupling through diffusional creep strain rate

It is possible to provide an alternative way of coupling for the elasticity problem (2.12)-(2.14) and the vacancy flow problem (2.7)-(2.8). Following the assumption of the previous subsection, the atomic flux field can be treated as the velocity of diffusive mass flow in a body that is statically fixed. Assuming that the inelastic flow velocity is defined in this manner, the rate of diffusional creep deformation can be written as

$$\dot{\boldsymbol{\varepsilon}}_{cr} = -1/2\left(\nabla \mathbf{j}_v + \nabla \mathbf{j}_v^{\,T}\right) \qquad (2.17)$$

Reproduced with permission of the copyright owner. Further reproduction prohibited without permission.

This equation defines the Eulerian strain rate tensor (see, for example, [51]), and represents the symmetric part of the Eulerian gradient of the mass flow velocity. The creep strain field is defined by Eq. (2.17) in every point of the body under consideration, as schematically illustrated in Figure 2.9.

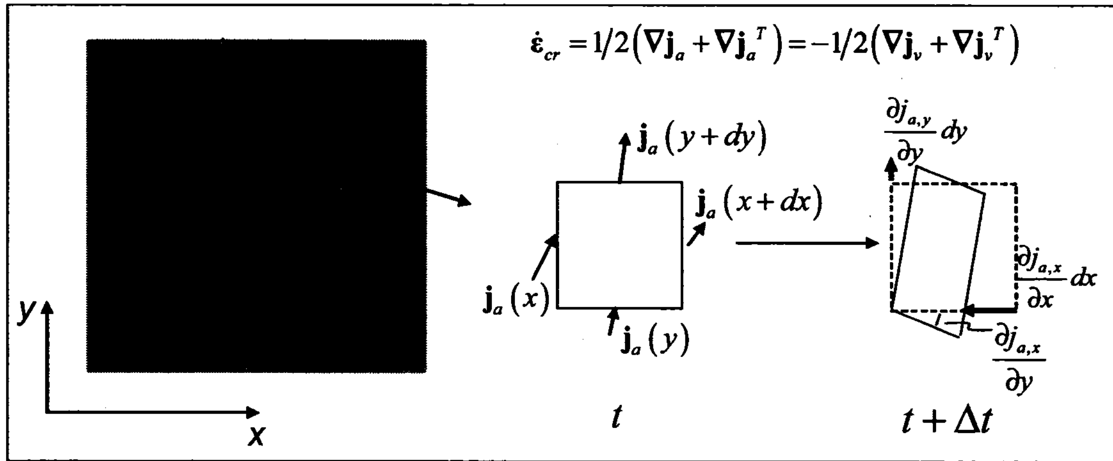

Figure 2.9. Schematic illustration of diffusion creep strain rate concept. The arrows that illustrate atomic flux $\mathbf{j}_a$ are understood as the mass flow velocities of material element faces.

Note that we implicitly assumed the Lagrangian kinematic description for elasticity subproblem. This is done for the sake of the simplicity to implement the elasticity governing equations in commercial finite element code, presented in the next chapter. However we anticipate that mass flow displacements may become large and the assumptions of small strains introduced for Eq. (2.13) may no longer be valid. It is possible to resolve this issue by adopting the updated Lagrandian formulation. We note that the updated Lagrangian technique enables to resolve the conflicting assumptions of Eulerian description for Eq. (2.16) and Lagrangian description for Eq. (2.13). The Eulerian description can be viewed as Lagrangian description at time t referred to the current fixed configuration. Thus, the elasticity equations (2.12)-(2.14) and kinematic

Reproduced with permission of the copyright owner. Further reproduction prohibited without permission.

mass flow description (2.17) can be used simultaneously in the incremental updated Lagrangian formulation.

The accumulation of pointwise creep strain can be obtained by integration of Eq. (2.17) on every time step. The accumulated creep strains will affect the evolution of stress state in the body. Assuming that total pointwise strain $\boldsymbol{\varepsilon}$ consists of elastic and creep components, the elastic part of the strain can be related to the total stress $\boldsymbol{\sigma}$ by Hooke's law

$$\boldsymbol{\sigma} = \mathbf{C} : (\boldsymbol{\varepsilon} - \boldsymbol{\varepsilon}_{cr}) \tag{2.18}$$

where $\mathbf{C}$ is the elastic stiffness matrix. Equation (2.18) gives explicit relation between the stress and vacancy flux, providing more direct coupling between two subproblems than the approach suggested in the previous subsection. One of the most significant advantages of coupling through creep strains is that this technique does not require to keep track of unloaded configuration throughout the simulation, eliminating the need to specify compatibility constraints between neighboring grains. Since both mass flow and stress relaxation occur in current loaded configuration, the formulation suggested here is consistent with the physics of the phenomenon. The coupled vacancy diffusion – elasticity problem governed by Eqs. (2.7)-(2.8), (2.12)-(2.14) and (2.17) is solved by the finite element technique presented in the next chapter.

Reproduced with permission of the copyright owner. Further reproduction prohibited without permission.

CHAPTER 3

NUMERICAL MODELING OF DIFFUSIONAL CREEP USING COMMERCIAL FINITE ELEMENT PACKAGE MSC.MARC

This chapter presents the details of the numerical implementation of coupled elasticity-mass flow boundary value problem adapted for commercial finite element package MSC.Marc. We describe the finite element types, features of mesh geometry and numerical procedures to solve the governing equations of the coupled problem. The numerical implementation presented in this chapter is later applied to the prediction of diffusional creep and stress relaxation response of typical interconnect structures, hence we expect to develop the procedures that demand reasonably affordable computer time and provide the time-stepping procedure which is computationally stable.

The length scale of grain boundary regions is several orders of magnitude smaller than the grain size. To account for the multiscale nature of the mass flow problem, we need to consider mesh refinement at grain boundaries and coarse mesh in grain interior. Because the model contains elements of different orders of magnitude and the diffusion is greatly enhanced in the nanoscale grain boundary region, the stability of time integration procedure is strongly dependent on the time step selection. We also note that although the finite element implementation assumes continuum treatment of coupled problem variables, typical interconnect line may contain several distinct grains per line width. This

Reproduced with permission of the copyright owner. Further reproduction prohibited without permission.

chapter presents the approach to consider the discrete structure in a continuum model using multipoint constraints.

3.1. Incremental solution of transient coupled governing equations

The finite element implementation of transient continuum mechanics problem typically involves the time integration of governing equation and the solution of boundary value problem on each time step. The procedure of time integration can be implicit, when the governing equation is written for time t_{s+1} and the values of unknown variables are found based on their values at time t_s. The procedure is unconditionally stable and allows for large time increments. However, we adopt the explicit time integration for the coupled formulation presented in the previous chapter due to the lack of general phenomenological constitutive relation between stress and creep strain rate. Rather, the coupling is based on kinematically defined creep strain rate, which necessitates the forward time integration of coupled equations written for time t_s. The elasticity and mass flow boundary value problems are treated in a staggered manner, when each subproblem is solved independently while holding the variables of the other subproblem fixed. We discuss the stability issues associated with the integration scheme, along with the details of incremental equation for principle of virtual work.

3.1.1. Incremental principle of virtual work and explicit time integration

During time step Δt the creep strain is incremented by $\Delta \boldsymbol{\varepsilon}^{cr}$ and total strain is incremented by $\Delta \boldsymbol{\varepsilon}$. We choose the displacement as the independent variable, hence $\Delta \boldsymbol{\varepsilon}$ needs to be expressed in terms of displacement increments $\Delta \mathbf{u}$. We employ the relation

Reproduced with permission of the copyright owner. Further reproduction prohibited without permission.

$$\Delta\varepsilon_{ij}^{cr} = 1/2\left(\Delta u_{i,j}^{cr} + \Delta u_{j,i}^{cr}\right) \tag{3.1}$$

where comma denotes partial differentiation with respect to the corresponding coordinate. Note that the small incremental strain assumption in Eq. (3.1) imposes small time step requirement to maintain the accuracy of iterative solution. For the simplicity of MSC.Marc implementation we employ the trapezoidal rule to compute the increment of inelastic displacement

$$\Delta\mathbf{u}^{cr} = 1/2\left(\mathbf{j}_t + \mathbf{j}_{t+\Delta t}\right)\Delta t \tag{3.2}$$

Thus we only use the vacancy fluxes $\mathbf{j}_{t+\Delta t}$ computed at the end of the increment, and reuse them as $\mathbf{j}_t$ at the beginning of the next increment.

The principle of virtual work may be written in incremental form as

$$\int_V \delta\boldsymbol{\varepsilon}^T : \mathbf{C} : \left(\Delta\boldsymbol{\varepsilon} - \Delta\boldsymbol{\varepsilon}^{cr}\right) dV = \Delta\mathbf{P}\cdot\delta\mathbf{u} \tag{3.3}$$

where $\Delta\mathbf{P}$ is the increment of the externally applied load. This equation is the basis for the finite element formulation of mechanical part of the problem. The following remarks should be made concerning the implementation of Eq. (3.3). The formulation is reduced to classical elasticity small strain problem by employing the initial strain technique, where a pseudo-load vector due to the creep strain increment is added to the right-hand side of the stiffness equation

$$\mathbf{K}\Delta\mathbf{u} = \Delta\mathbf{P} + \int_V \boldsymbol{\beta}^T \mathbf{C}\Delta\boldsymbol{\varepsilon}^{cr} dV \tag{3.4}$$

In this equation, $\mathbf{K}$ is the stiffness matrix and $\boldsymbol{\beta}$ is the strain-displacement matrix. The transient creep strain increment is obtained from the mass flow problem.

In MSC.Marc, the integration of Eq. (3.4) is done through explicit time integration procedure. For this scheme, the stiffness matrix and load vector in Eq.(3.4)

Reproduced with permission of the copyright owner. Further reproduction prohibited without permission.

are written at time t, and the equation is solved for displacement that occurs due to creep strain increment $\Delta\varepsilon_{cr}$ during time Δt. The drawback of explicit integration procedure is the requirement to select the time step small enough to ensure the stability of the integration and the absence of oscillations that lead to divergence.

3.1.2. MSC.Marc finite element mesh and element types

We consider the plane strain geometry to model the interconnect lines with length at least an order of magnitude greater than width and height (see Figure 2.3c). The element type of our choice is 4-node quadrilateral. We select this element both for the simplicity of meshing and for computationally efficient implementation. Since we expect to have fine mesh with element size on the order of Cu atomic radius in the grain boundary region, the number of elements will be large and the low-order element such as 4-node quadrilateral is desired. The typical finite element mesh of a single grain is shown in Figure 3.1. It consists of 1168 elements with 1256 nodes. Only a quarter of the grain may be modeled due to symmetry. Also, it is convenient to reduce the number of elements by using larger elements in the grain interior. This can be done without any significant loss of accuracy since the diffusivity in the grain interior is at least an order of magnitude smaller than in the grain boundary region where Coble creep strains are localized.

Reproduced with permission of the copyright owner. Further reproduction prohibited without permission.

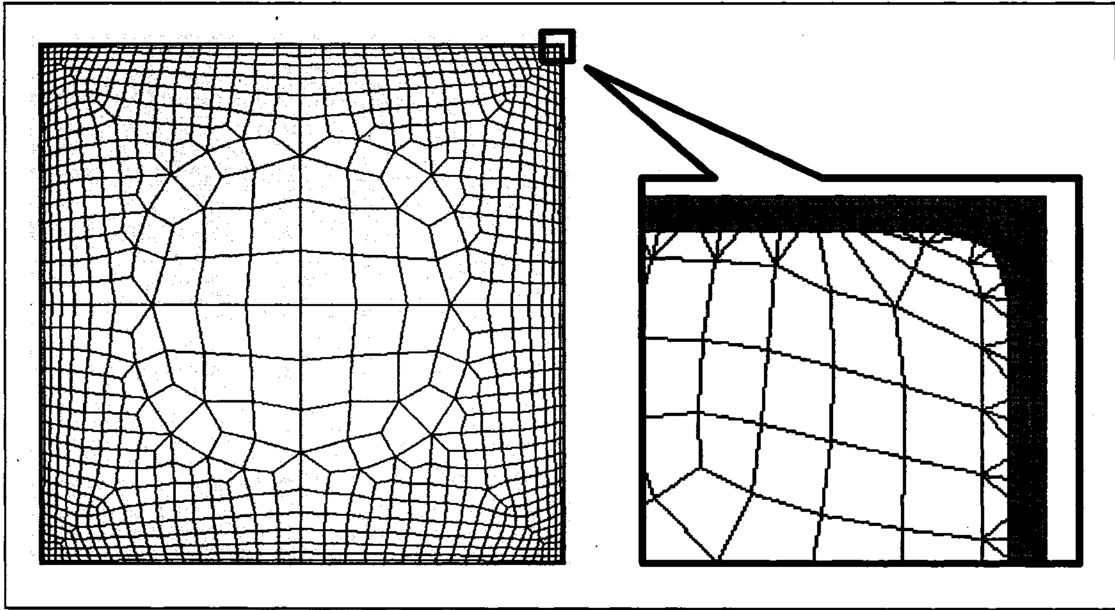

Figure 3.1. Finite element mesh of idealized square grain. The shaded area represents the grain boundary region with a typical thickness of 1 nm.

3.1.3. Treatment of discrete grain assembly in a continuum model using multipoint constraints

We note that in case the multigrain assembly is modeled as a single continuous body, the normal component of vacancy flux in the grain boundary nodes is canceled out as the integration point values of flux are averaged to compute nodal values. As a result, the creep strain increments are affected in the elements adjacent to the grain boundary assuming that these increments are computed from nodal mass flow displacements according to the Eq. (3.1). In order to adequately compute the interfacial vacancy flux and creep strain for adjacent grains we model each individual grain as a separate body. It is important to consider both the non-penetration condition and the atomic bonding that exists at grain interfaces. To avoid the computationally intensive implementation of contact body finite element procedures, we model bonded boundaries of grains using

Reproduced with permission of the copyright owner. Further reproduction prohibited without permission.

multipoint constraints between the tied degrees of freedom of two adjacent surfaces. Such implementation allows to specify different orientations for each individual grain.

In this treatment, the corresponding nodes of two adjacent grains are constrained for the displacement increments normal to the grain interface

$$(\Delta \boldsymbol{u}_A - \Delta \boldsymbol{u}_B) \cdot \boldsymbol{n} = 0 \tag{3.5}$$

The constrained degrees of freedom are schematically illustrated in Figure 3.2. This approach considers the non-penetration condition of adjacent grains and takes into account the atomic bonding which prevents grains from separation under tension.

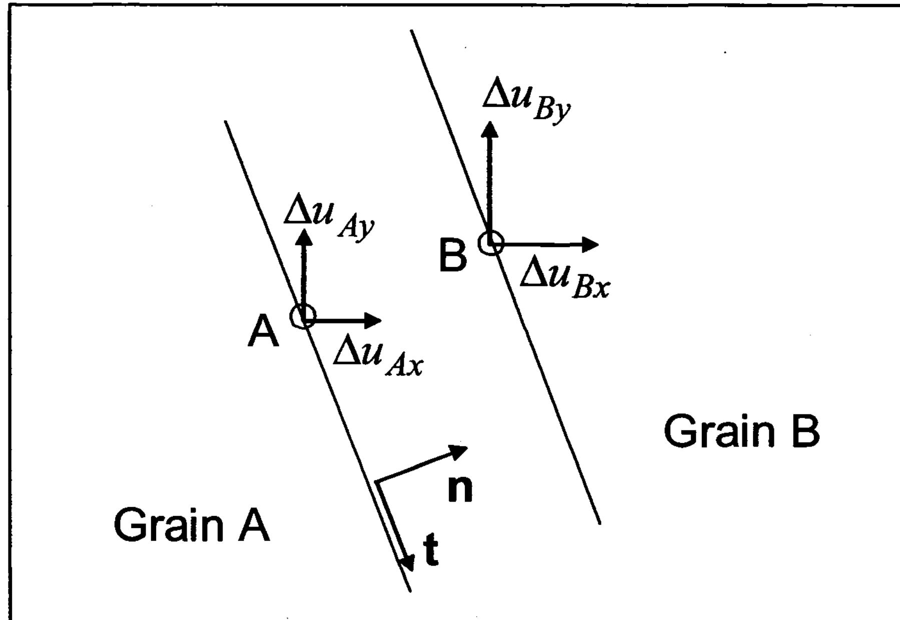

Figure 3.2. Degrees of freedom for adjacent nodes of neighboring grains constrained by Eq. (3.5).

To account for grain boundary sliding, it is possible to specify the relative velocity between adjacent grains and introduce another multipoint constraint for the component of displacement tangent to the grain interface:

$$(\Delta \mathbf{u}_A - \Delta \mathbf{u}_B) \cdot \mathbf{t} = \dot{U}(\tau, T, \lambda, h) \Delta t \tag{3.6}$$

Reproduced with permission of the copyright owner. Further reproduction prohibited without permission.

Here, $\dot{U}(\tau,T,\lambda,h)$ is the sliding velocity that depends on shear stress τ and temperature T, as well as grain interface parameters. Example of such parameters may be periodic wavelength λ and amplitude $h/2$ schematically shown in Figure 3.3. The effect of these parameters was taken into account in the sliding rate formula given by Raj and Ashby [20]

$$\dot{U}=\frac{8}{\pi}\frac{\tau\Omega}{kTh^2}\left[\lambda D_L+\pi\delta D_{GB}\right] \tag{3.7}$$

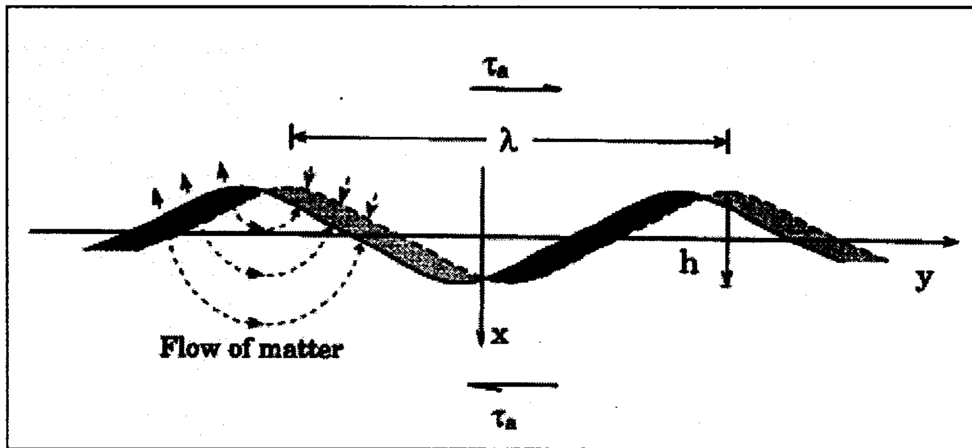

Figure 3.3. Grain boundary sliding model suggested by Raj and Ashby [20].

3.2. Reduction of computer computation time

It is important to note that the MSC.Marc finite element implementation outlined above requires a large amount of computer time. The computation is expensive due to multiple length scales present in the model with grain boundary region thickness 1-2 orders of magnitude smaller than the size of a typical nanoscale grain. Furthermore, a large difference between the diffusivities in grain interior and grain boundary region leads to ill-defined system of linear equations. Both the size of the smallest finite element

Reproduced with permission of the copyright owner. Further reproduction prohibited without permission.

in the model λ_{min} and the value of grain boundary diffusivity are limiting the maximum allowable time step, which can be estimated for a diffusion problem as (Huebner et al. [52])

$$\Delta t_{max} \sim \lambda_{min}^2 / D_{gb} \tag{3.8}$$

We also note that the diffusional creep feature is not common in the commercially available FEA packages. The implementation of this feature in MSC.Marc can be done through two alternative ways. The first method is to launch the FEA program separately on each time step for elasticity and mass flow subproblems. The output of each subproblem is adjusted to become the input data used by another subproblem. This can be done for the formulation where coupling is provided through grain boundary vacancy fluxes. The drawback of this implementation is the large amount of overhead computer time needed to launch the program twice on each iteration, as well as large amount of disk read/write operations.

An alternative method can be used for the formulation where coupling is done through diffusional creep strain rate. Both subproblems can be solved in a single launch of FEA code. The exchange of data between mass flow and elasticity subproblems is performed through user-defined subroutines listed in Appendix A.

We have implemented both approaches in MSC.Marc and used the simple test problem to compare the computation time it takes to run the simulation over the prescribed number of steps. Table 3.1 provides the test computation for the finite element model of a single Cu grain shown in the inset of Figure 3.4. As can be seen from the table, for this particular model the diffusional creep strain rate coupling approach

Reproduced with permission of the copyright owner. Further reproduction prohibited without permission.

provides more than 10-fold reduction of computation time. Figure 3.4 illustrates that the predictions of both coupling approaches are very close.

To further reduce the computation time, we employ the mesh refinement multipoint constraints, adjustable time step and time series extrapolation. The test simulations for these techniques use the values of temperature selected in the range from 673 K to 1000 K since the maximum allowable time step becomes particularly small at elevated temperatures according to Eq. (3.8).

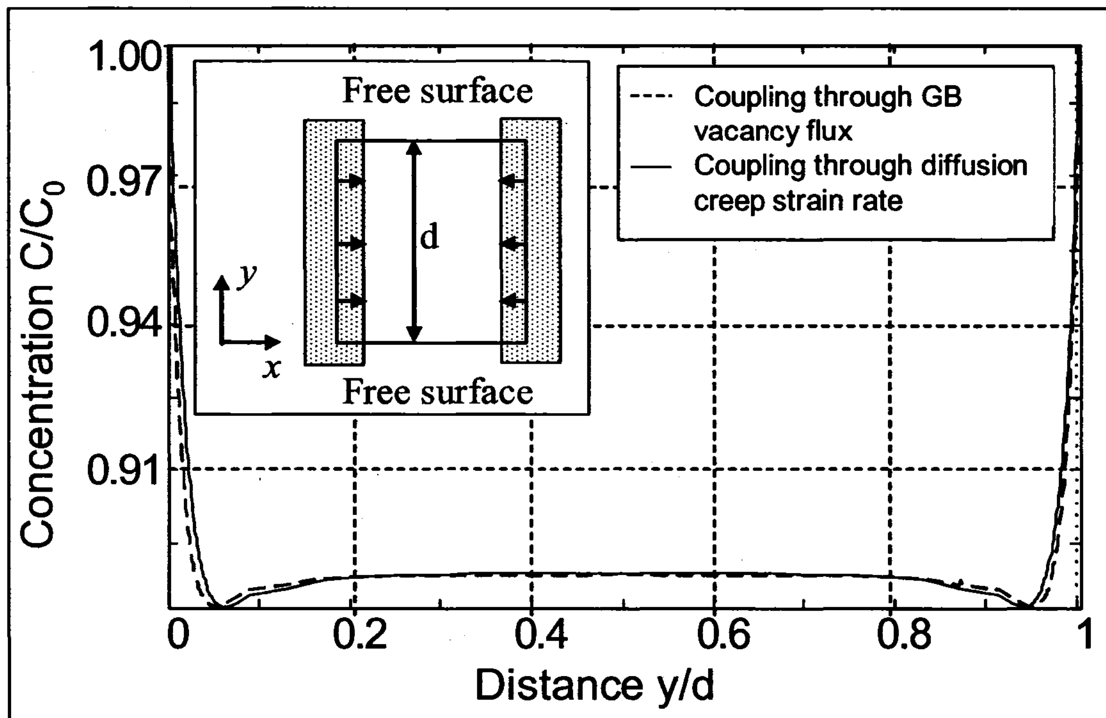

Figure 3.4. The predictions of concentration profile are close for both coupling approaches through GB vacancy flux and through creep strain rate.

Reproduced with permission of the copyright owner. Further reproduction prohibited without permission.

Table 3.1. Parameters of test computation to compare the performance of coupling approach through grain boundary flux and coupling through diffusional creep strain rate

Parameter	Value
Number of elements	2232
Number of nodes	2389
Temperature, K	873
Grain size, μm	1.0
Young's modulus, GPa	128
Poisson's ratio	0.33
Grain interior diffusivity, m^2/s	$5.46*10^{-12}$
Grain boundary diffusivity, m^2/s	$1.12*10^{-10}$
Horizontally applied fixed displacement, nm	0.1
Number of transient time steps	10000
Computation time with coupling through grain boundary fluxes, min	1200
Computation time with coupling through diffusional creep strain rate, min	90

3.2.1. Mesh refinement multipoint constraints

To reduce the number of finite elements in the grain interior mesh, we introduce the first order mesh refinement multipoint constraints into our finite element model. Figure 3.5 shows the mesh refinement approach for two-dimensional quadrilateral element with interior nodes on refined side tied to the corner nodes on the coarse side. The displacement and vacancy concentration of tied node is linearly interpolated between displacements and vacancy concentrations of retained nodes.

Note that the aforementioned mesh refinement multipoint constraints produce continuous displacement and concentration fields. We compare the predictions of two finite element models for periodic grain array subjected to fixed horizontal compressive strain $\varepsilon_x = 0.001$. The model with mesh refinement multipoint constraints contains 448 elements, and the model with continuous mesh has 648 elements. The simulation is

Reproduced with permission of the copyright owner. Further reproduction prohibited without permission.

performed for the temperature 800 K with time period of 0.01 s. The vacancy concentration field predictions are close for both models as shown in Figure 3.6. However the mesh refinement leads to discontinuities in stress field, as shown in Figure 3.7. This observation does not prevent the use of mesh refinement to predict the average stress relaxation since the evolution of the stress averaged over the volume of the model is not significantly different for continuous and refined meshes, as shown in Figure 3.7b.

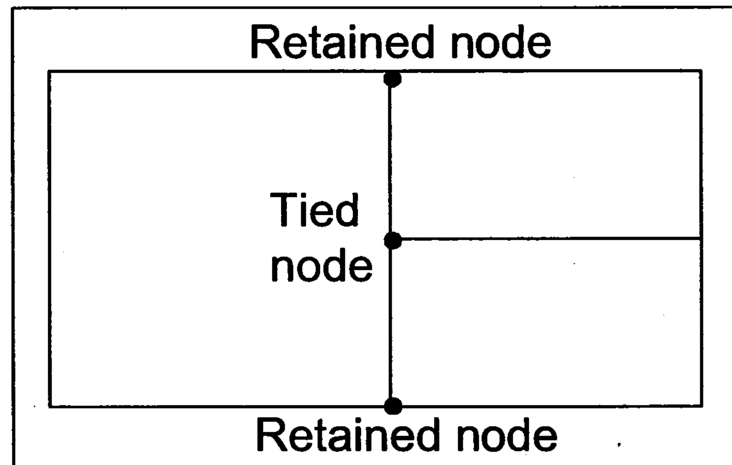

Figure 3.5. First order mesh refinement multipoint constraint.

The advantage of mesh refinement multipoint constraints in saving the computation cost is obvious considering that the time required to go through direct SLE solver in MSC.Marc varies roughly linearly with number of degrees of freedom (MSC.Marc manual [53]).

Reproduced with permission of the copyright owner. Further reproduction prohibited without permission.

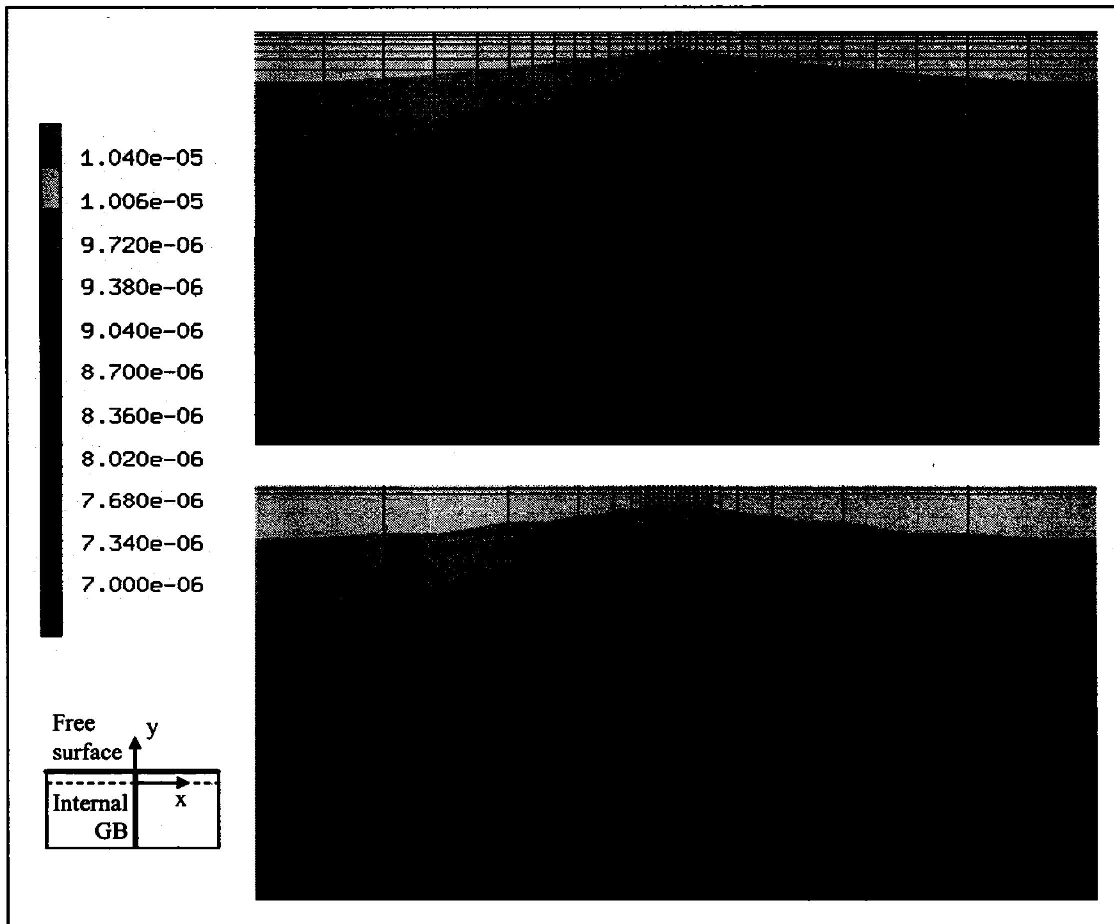

Figure 3.6. Comparison of vacancy concentration field predictions for FEA models with continuous mesh and mesh refinement multipoint constraints at temperature 800 K, time t = 0.01 s.

Reproduced with permission of the copyright owner. Further reproduction prohibited without permission.

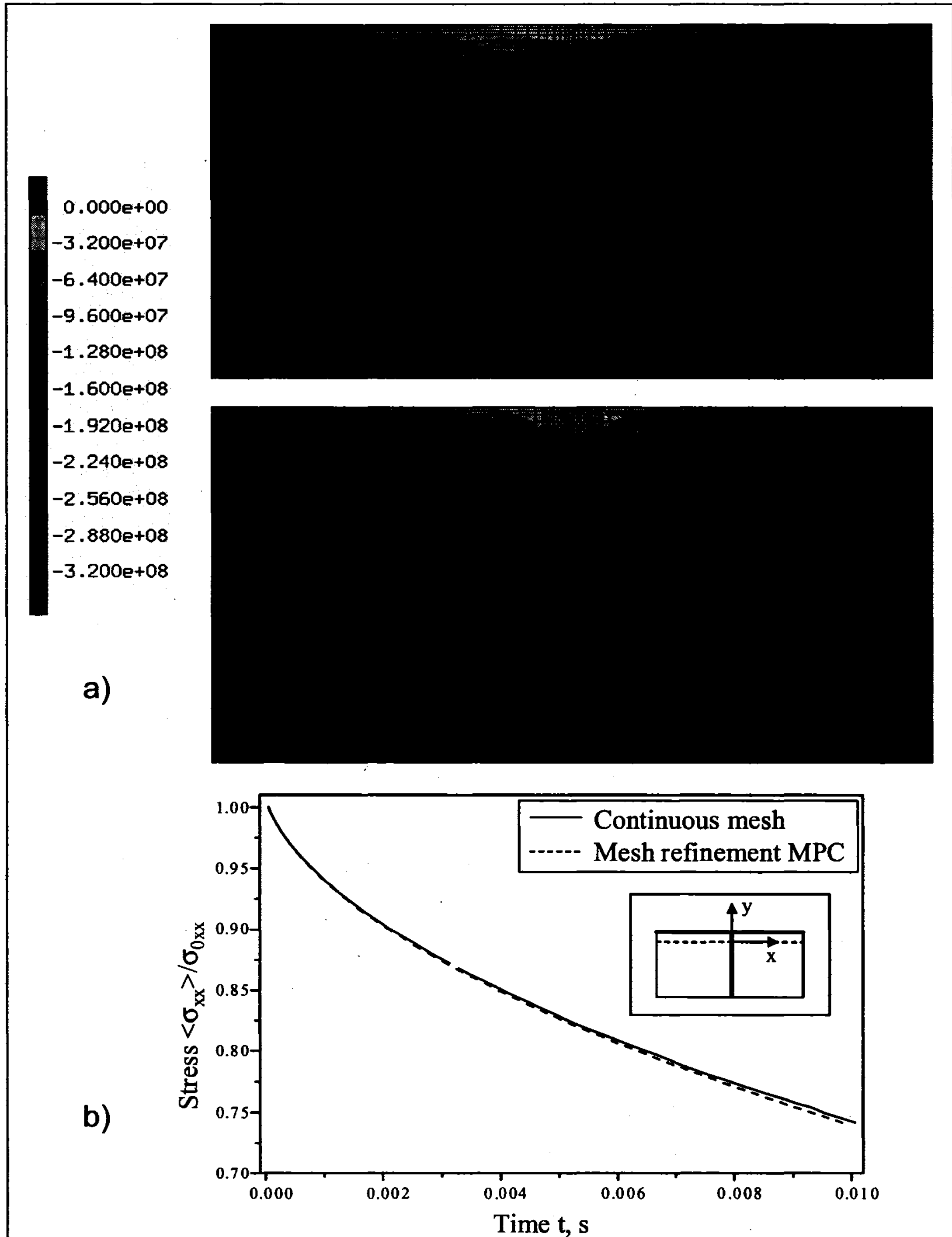

Figure 3.7. Comparison of stress σ_{xx} predictions for FEA models with continuous mesh and mesh refinement multipoint constraints at temperature 800 K, time t = 0.01 s. (a) Distribution of stresses. (b) Evolution of average stress.

Reproduced with permission of the copyright owner. Further reproduction prohibited without permission.

3.2.2. Selection of adjustable time step and stability of incremental procedure

The explicit time integration procedure outlined above requires the selection of the time step which is below some critical value. If the time step exceeds the critical value, the loss of stability occurs and oscillations are observed in the variables of the model such as displacements, stresses, vacancy concentrations. The example computation is shown in Figure 3.8 to illustrate the oscillations that signify the loss of stability in the finite element solution. The periodic array of 500 nm square grains is subjected to externally applied compressive displacements 0.1 nm at temperature 673 K. The time step is selected as $6.0 \cdot 10^{-5}$ s which results in the maximum increments of equivalent creep strain in the model $\Delta\bar{\varepsilon}_{cr}^{\max} = 3.7 \cdot 10^{-3}$. Figure 3.8 shows that the time step has to be smaller to avoid the growth of oscillations over a period of time $\Delta t = 0.012$ s.

It was determined through numerical experiments that the critical time step Δt^{*} that ensures stability of time integration should be such that the maximum equivalent creep strain increment in the model $\Delta\bar{\varepsilon}_{cr}^{\max}$ during the time step does not exceed the critical value $\Delta\bar{\varepsilon}_{cr}^{*} = 10^{-4}$. The creep strain rate strongly depends on temperature and applied stress, thus when the time step is selected based on the threshold value $\Delta\bar{\varepsilon}_{cr}^{*}$, the effects of temperature and applied stress on the critical time step are taken into account.

Note that in stress relaxation problems, the vacancy fluxes and corresponding diffusional creep strain increments are reduced with time, due to the reduction in stress gradients that drive the mass flow. Accordingly, the time step may be increased to maintain the maximum equivalent creep strain increment that occurs during time Δt as

Reproduced with permission of the copyright owner. Further reproduction prohibited without permission.

$\Delta\bar{\varepsilon}^{*}_{cr}$. We increase the time step proportionally to the reduction in creep strain increment to reduce the computation time without the loss of stability.

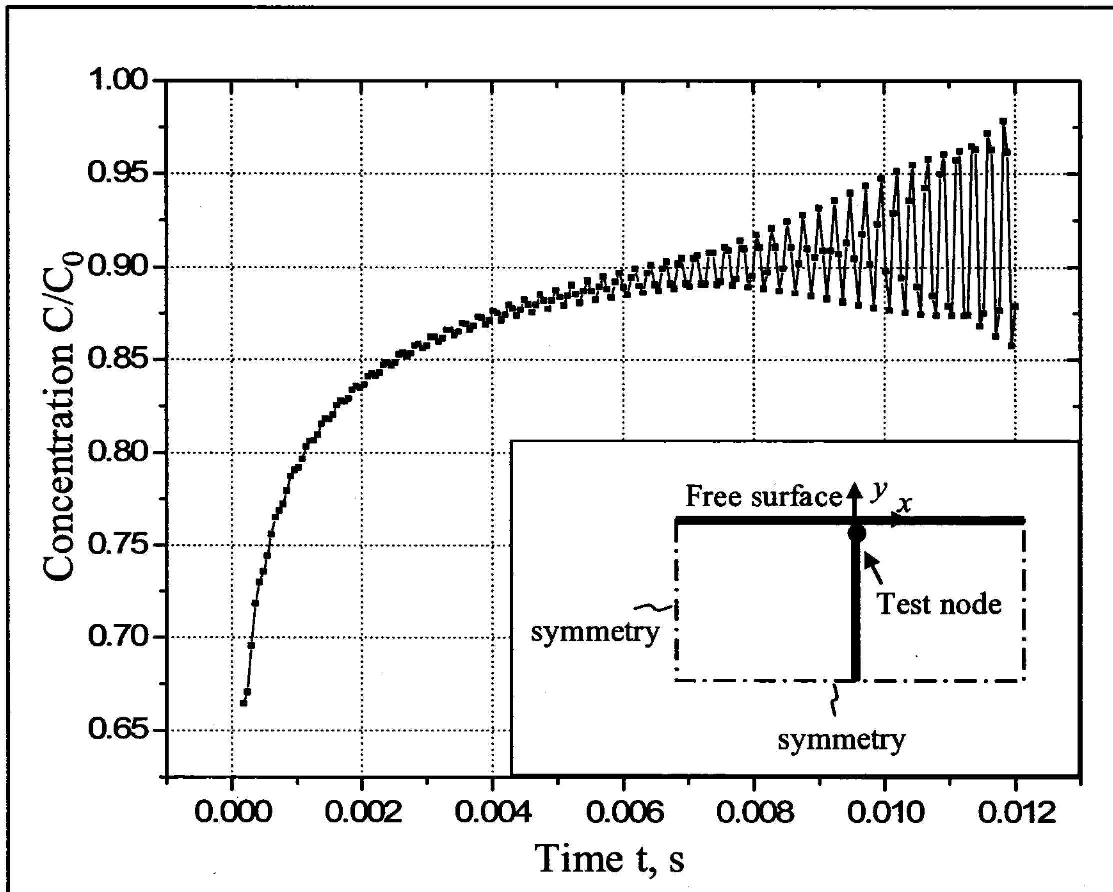

Figure 3.8. Example of the growth of oscillations that occurs during forward time integration when time step exceeds the critical value required for stability of explicit procedure.

3.2.3. Increase of computation efficiency using extrapolation

The computation time can be reduced by increasing the time step. However, as presented in the previous subchapter, there is a critical time step dependent on applied stress and temperature that must not be exceeded to maintain stability. Thus we turn to

Reproduced with permission of the copyright owner. Further reproduction prohibited without permission.

the time series extrapolation as an alternative method to reduce the computation cost. By extrapolating the nodal quantities such as displacements and vacancy concentrations, it is possible to reduce the number of time increments required to achieve stress relaxation.

This is done by using the FEA-computed results from several time steps to "skip" a certain number of time increments. The extrapolation of nodal variables in time predicts the values of nodal variables that contain errors depending on the length of extrapolation interval. To ensure the stability of the subsequent integration, a certain number of after-extrapolation stabilization steps or "recovery" steps is needed.

In stress relaxation problems, we assume that external fixed displacement is applied instantaneously. Sudden application of boundary conditions results in initially large rates of change for nodal concentration, stress and creep strain. These rates are dramatically reduced on later stages of stress relaxation, as illustrated in Figure 3.9 for vacancy concentration. Thus it is particularly attractive to apply the extrapolation for stress relaxation problems at the stage when the effect of sudden application of external fixed displacement is smoothed out.

When extrapolation is applied to coupled elasticity-mass flow boundary value problem, it is important to consider, among other technical issues, which method to use to minimize the extrapolation error, what number of steps to specify for after-extrapolation stabilization, and what variables to extrapolate. Regarding the selection of extrapolation variables, it is necessary to provide the extrapolation for both displacements and vacancy concentration in every node, since the coupled formulation presented in the previous chapter assumes both displacements and vacancy concentrations as primitive variables. Note that total nodal displacements can be obtained from finite element equations (3.4) if

Reproduced with permission of the copyright owner. Further reproduction prohibited without permission.

the creep strains that occur during the time step are known. Since creep strains can be integrated from Eqs (3.1)-(3.2) given the evolution of vacancy fluxes, we conclude that the variables that need to be extrapolated are the concentrations and vacancy fluxes.

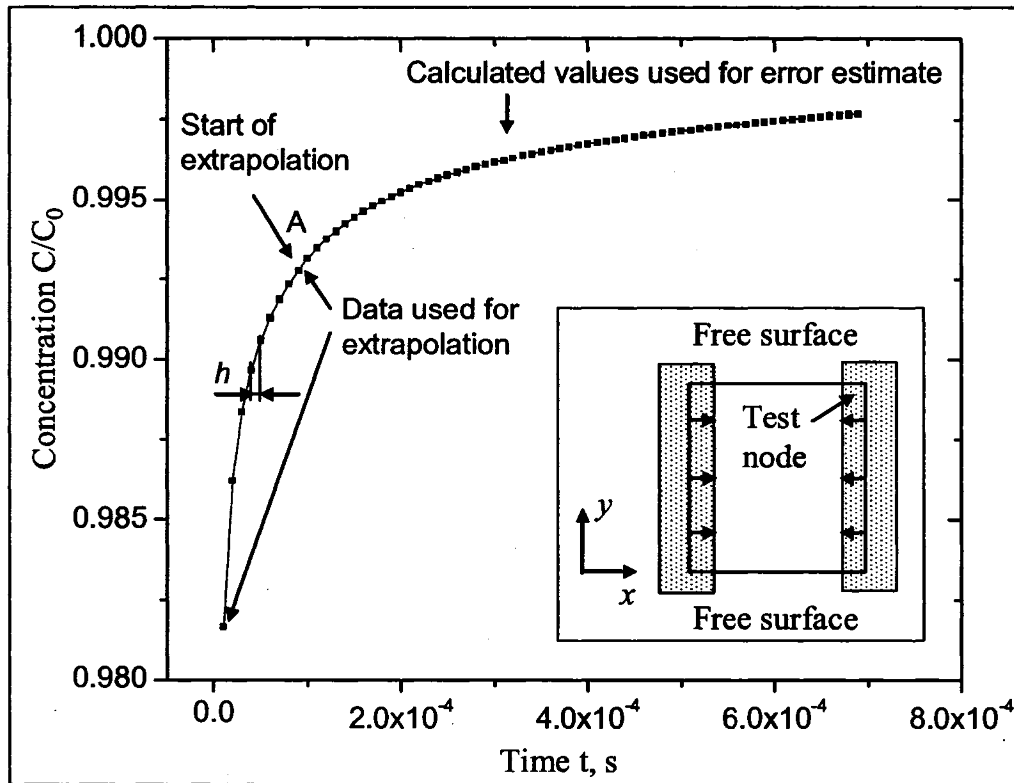

Figure 3.9. Test problem used to evaluate the performance of vacancy flux and concentration nodal time series extrapolation.

We have explored the stability and accuracy performance of several extrapolation methods through a number of numerical experiments. The computations have been performed for the test problem of single 1μm grain subjected to the compressive strains $\varepsilon_x = 5 \cdot 10^{-4}$ at temperature 1000 K. We selected the individual time step 10^{-8} s for the explicit time integration procedure. The extrapolating function is specified in the form of

Reproduced with permission of the copyright owner. Further reproduction prohibited without permission.

a Taylor series expansion around base point that corresponds to time $8 \cdot 10^{-5}$ s, i.e. 8000 time steps. The extrapolation base point A for explicitly integrated test node vacancy concentration C_{true} is shown in Figure 3.9. The time derivatives of function f in point A are evaluated using the finite difference expressions for equally spaced data points separated by interval h [54]:

$$\frac{df}{dt} = \frac{1}{60h}(10f_1 - 72f_2 + 225f_3 - 400f_4 + 450f_5 - 360f_6 + 147f_7)$$
$$\frac{d^2 f}{dt^2} = \frac{1}{180h^2}(137f_1 - 972f_2 + 2970f_3 - 5080f_4 + 5265f_5 - 3132f_6 + 812f_7) \quad (3.9)$$
$$\frac{d^3 f}{dt^3} = \frac{1}{8h^3}(15f_1 - 104f_2 + 307f_3 - 496f_4 + 461f_5 - 232f_6 + 49f_7)$$

These expressions are obtained by constructing the 6-th order interpolating polynomial that passes through 7 equally spaced data points taken from the computed extrapolation data preceding point A as indicated in Figure 3.9. The 7-point expression (3.9) uses backward interpolation from base point A, and results in the estimation of derivatives with the error $O\left(h^{7-n}\right)$, where n is the order of the derivative.

Note that the extrapolation error depends on the method used, the smoothness of data, the interval of extrapolation and other parameters. We have observed that if the error introduced into the explicit time integration scheme is sufficiently small, the numerical time integration procedure is self-stabilizing. Thus the error in extrapolated nodal quantities can be reduced if a number of "recovery" time integration steps is performed after extrapolation. However, if the extrapolation is repeated without sufficient number of "recovery" steps, the extrapolation error is growing and stability is not preserved. Thus, for each extrapolation method, after the concentration and vacancy flux are extrapolated, a certain number of "recovery" explicit time integration steps N_r is

Reproduced with permission of the copyright owner. Further reproduction prohibited without permission.

needed before the extrapolation can repeated. In what follows, we refer to both the extrapolation and subsequent "recovery" steps as the extrapolation sequence. For the first order Taylor series expansion of extrapolating function at base point A, Figure 3.10 shows how the error $(C - C_{true}) / C_{true}$ at the end of the extrapolation sequence depends on the fraction of recovery steps in total number of extrapolation sequence steps N_s. The error estimated at the end of the extrapolation sequence is vanishing as this ratio exceeds 0.5, i.e. the "recovery" time interval is the same as the extrapolation time interval. Such extrapolation sequence already results in twofold decrease of computation time. Note that the extrapolation sequence with the ratio $N_r / N_s = 0.5$ is stable up to the 3rd order extrapolating polynomial, as illustrated in Figure 3.11(a).

For practical applications, it is attractive to maximize the extrapolation interval and minimize the number of "recovery" steps. We explore the stability of extrapolation sequence with $N_r / N_s = 0.1$ which gives an order of magnitude saving for computation time. Figure 3.11(b)-(d) shows that for the extrapolation sequence with longer extrapolation intervals and smaller number of "recovery" steps, only the first order extrapolating polynomials provide stability for repeating extrapolation procedure. We attribute this behavior to better accuracy of 1st order extrapolating polynomial for the initial stage of stress relaxation, as shown in Figure 3.12(a). Less accurate predictions of higher order extrapolating polynomials for this stage may be explained by the sensitivity of finite difference expressions (3.9) to the deviation in the values of datapoints.

At later stages of stress relaxation, higher-order extrapolation polynomials provide more accurate extrapolation, as shown in Figure 3.12(b). Note that this observation prevents us from making a conclusion about which order of extrapolation

Reproduced with permission of the copyright owner. Further reproduction prohibited without permission.

polynomial is more appropriate since the extrapolation accuracy depends on the time that has elapsed since the sudden application of external load. However, we have observed that linear extrapolation ensures the stability for both initial and later stages of stress relaxation. Although it is clear that more efficient procedure would switch from linear to higher order extrapolation polynomial once the time derivatives of vacancy concentrations and fluxes is sufficiently small, we note that the transition between these regimes differs from node to node. For simplicity, we use linear extrapolation in the numerical models presented in the next chapters.

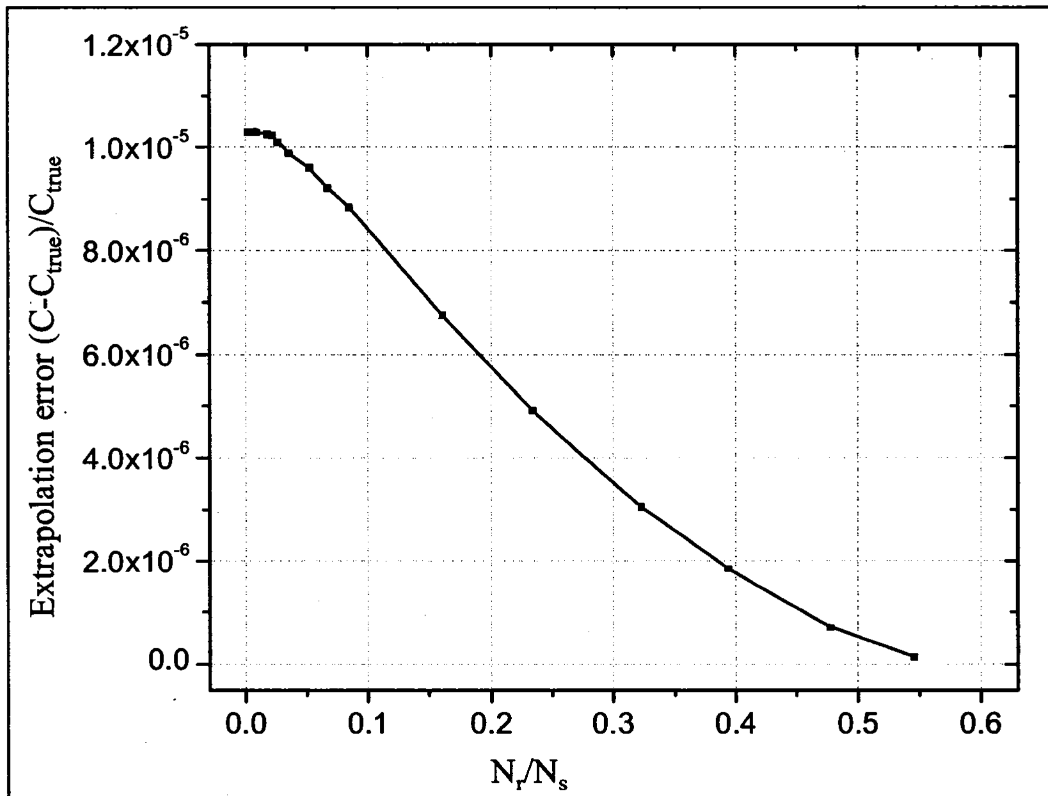

Figure 3.10. Dependence of the extrapolation error on the fraction of "recovery" steps in extrapolation sequence.

Reproduced with permission of the copyright owner. Further reproduction prohibited without permission.

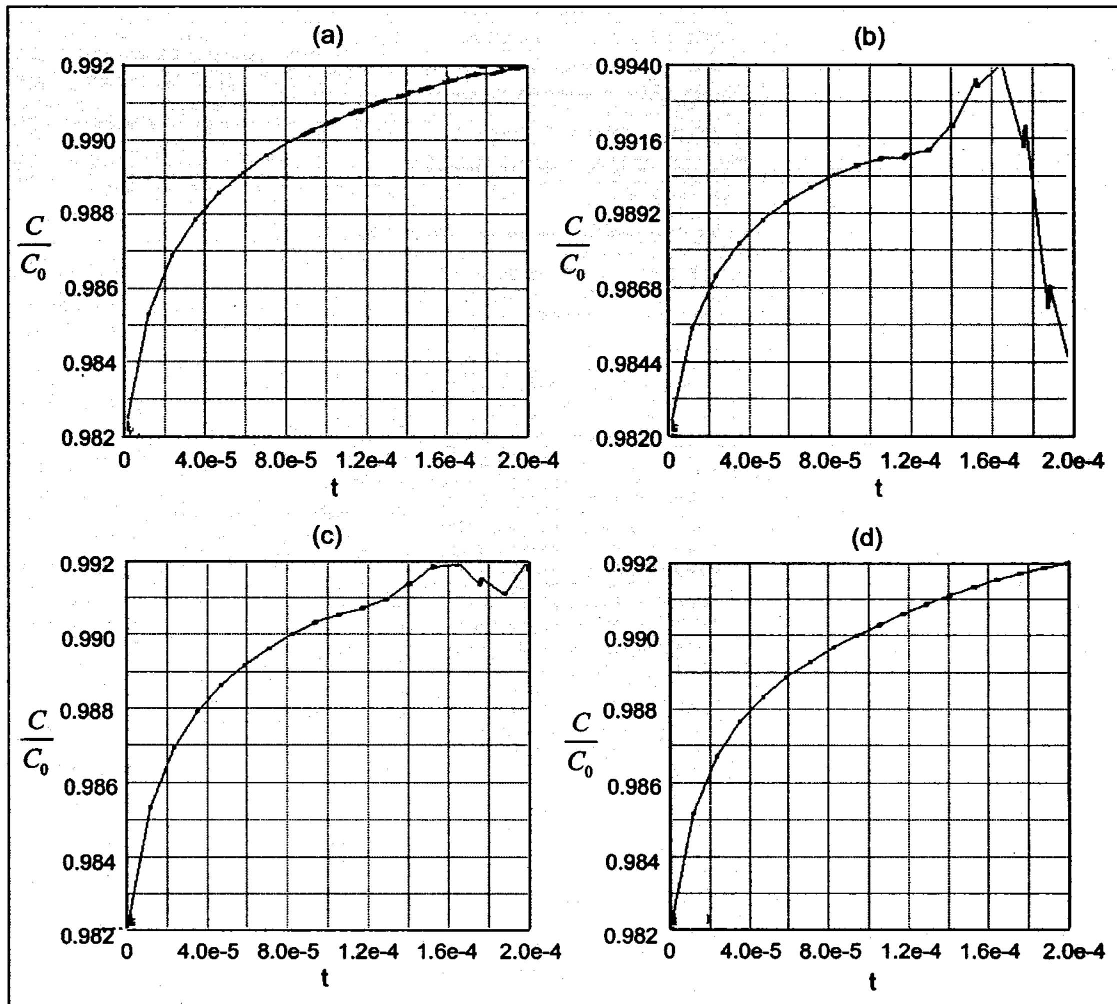

Figure 3.11. Stability of repeating extrapolation sequence for total number of sequence steps $N_s = 1000$. (a) third order extrapolation polynomial, $N_r = 500$. (b) third order extrapolation polynomial, $N_r = 900$. (c) second order extrapolation polynomial, $N_r = 900$. (d) first order extrapolation polynomial, $N_r = 900$.

Reproduced with permission of the copyright owner. Further reproduction prohibited without permission.

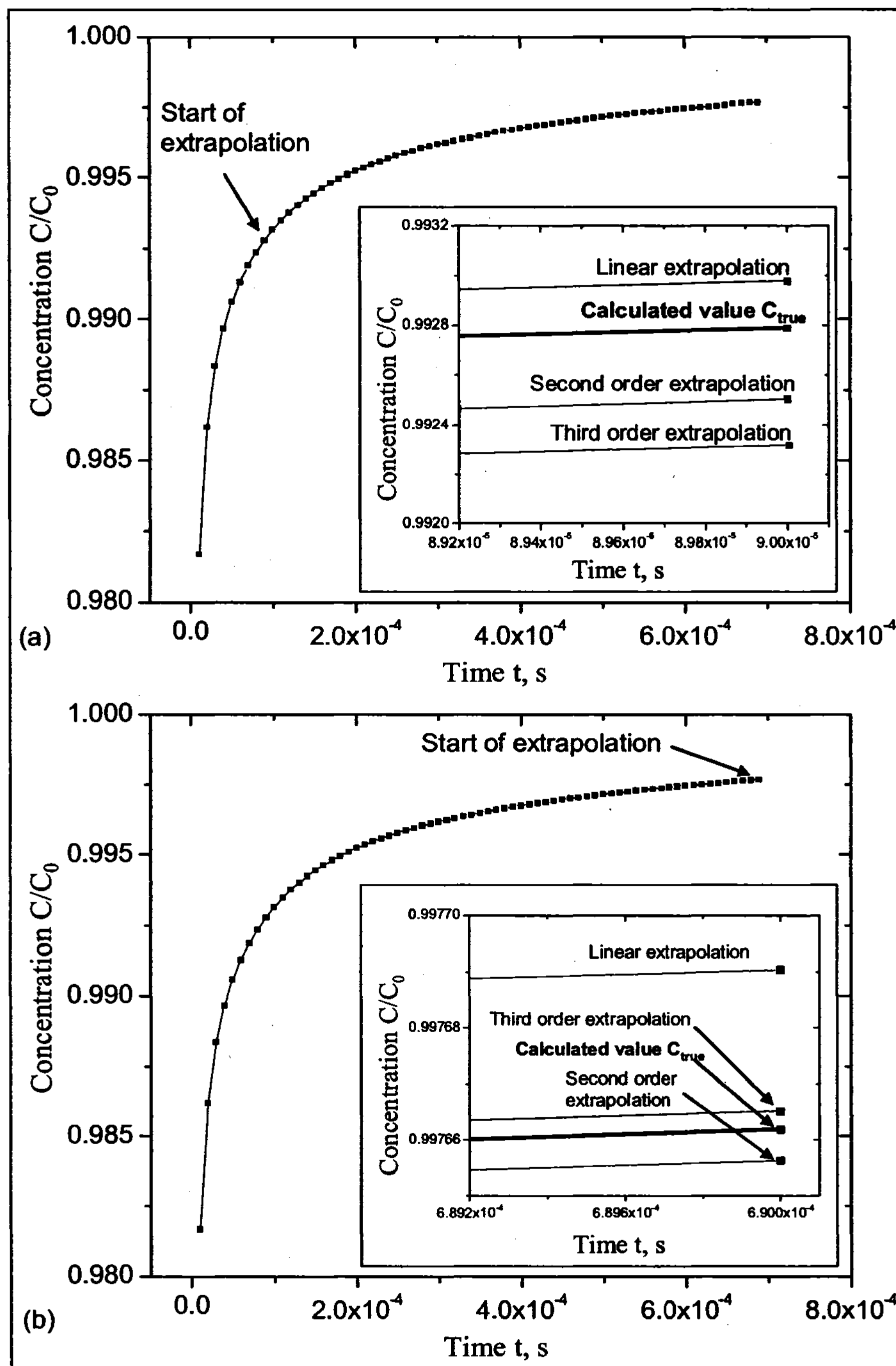

Figure 3.12. Dependence of extrapolation accuracy on the selection of extrapolation base point.

Reproduced with permission of the copyright owner. Further reproduction prohibited without permission.

CHAPTER 4

DIFFUSIONAL CREEP AND STRESS RELAXATION IN PERIODIC GRAIN ASSEMBLIES AND VALIDATION OF FINITE ELEMENT PROCEDURE

In this chapter we apply the coupled elasticity-mass flow finite element procedure to test problems of a single grain, linear grain array and two-dimensional 3x3 grain assembly. The primary purpose of the numerical computations is to validate the procedure presented in Chapter 3. To meet this goal, we provide the comparison of our finite element predictions to the modeling results of Garikipati et al. [26] and Gao et al. [17]. We also compare the numerical results to the theoretical predictions of established Nabarro-Herring and Coble creep models.

In the process of validation, we establish the patterns of strain, displacement and stress evolution. The idealized geometry of the problems considered in this chapter facilitates the observation of the effect of model parameters such as grain size and the thickness of enhanced diffusivity grain boundary region on the transient creep and stress relaxation response. We also study the dependence of the response on physical parameters such as temperature and activation energy of vacancy motion. We complete the chapter by applying the finite element model to the problem of grain boundary grooving for the grain array subjected to constant externally applied stress.

Reproduced with permission of the copyright owner. Further reproduction prohibited without permission.

4.1. Stress relaxation of Cu linear square grain array

We consider the simplified two-dimensional plane strain model of copper linear grain array in which a single layer of grains is periodically arranged along the horizontal direction. The grains are assumed to have idealized square shape, see Figure 4.1. To take advantage of the symmetry, we model the square grain array with the upper half resting on the substrate. This is equivalent to modeling of the entire grain array with vertical displacements fixed along the horizontal axis of symmetry. Similar simplified models are frequently used in the literature. The examples include the studies of displacement, strain and stress response by Gao et al. [17], Buehler et al. [19], and the investigation of the behavior of grain boundary grooving and surface diffusion in [37], [38], [41]. Possible practical applications of this simplified model include the stress relaxation and creep analysis of Cu thin films. However the computations presented here are used primarily for validation purposes and for establishing the patterns of mass flow and mechanical response that could be used to analyze the behavior of interconnect lines with several grains per line width.

Reproduced with permission of the copyright owner. Further reproduction prohibited without permission.

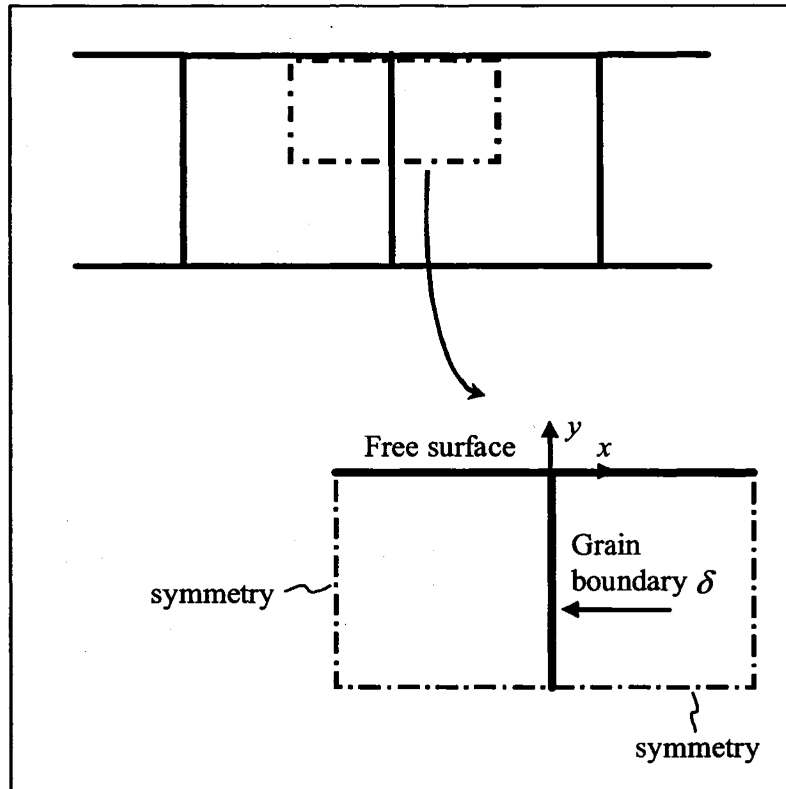

Figure 4.1. Model of periodic square grain array used for validation of finite element procedure.

4.1.1. Modeling assumptions and parameters

We consider the stress relaxation in a 2D (plane strain) grain array shown in Figure 4.1. The square shape of the grains allows to consider the periodic problem for only half of a single grain. Furthermore, if the vertical displacement is fixed along the horizontal axis of symmetry, it is possible to consider only a quarter of a grain. However, we choose to model two quarter-grains to test the performance of the multipoint constraints implementation of discrete grain assembly in a continuum model, presented in Section 3.1.3.

The numerical values of the parameters used in the computation are listed in Table 4.1. The value of atomic volume Ω is taken from Frost and Ashby [49], the

Reproduced with permission of the copyright owner. Further reproduction prohibited without permission.

activation energy for vacancy motion in the grain interior $Q_{m,b}$ is estimated as $Q_{m,b} = Q_b - Q_f$ where Q_b = 197 kJ/mol is the activation energy of vacancy diffusion in copper (Frost and Ashby [49]) that includes both the energies of vacancy formation and motion. The estimate of the energy of vacancy formation Q_f is the subject of ongoing research in the scientific community [55-58]. Measurements of this quantity are not readily available. However, the first-principles calculations for energy of vacancy formation exist in the literature. For the computations presented here we estimate Q_f as an intermediate value between the reported calculations for the temperature of 0 K (Sato et al. [57]) and 1000 K (Grochola et al. [58]). The thickness of enhanced diffusivity grain boundary region is selected as 1 nm which corresponds to ~4 Cu atomic monolayers. As described in Chapter 2, the activation energy for vacancy motion in the grain boundary region $Q_{m,gb}$ is treated as an adjustable parameter that may be affected by impurities, grain boundary roughness, crystallographic orientation and other factors. For the calculations presented in this chapter, we assume $Q_{m,gb} = 0.6Q_{m,b}$ to explore the stress relaxation response when the grain boundary activation energy is significantly reduced. This assumption results in considerable increase of grain boundary vacancy diffusivity compared to the diffusivity in the grain interior, as indicated in Figure 2.4. Thus, we can expect the dominance of Coble creep mode.

The model is subjected to instantaneously applied compressive strain $\varepsilon_x = 0.002$. The initial purely elastic deformation is schematically shown in Figure 4.2(a). Application of fixed horizontal strain ε_x results in initially uniform horizontal

Reproduced with permission of the copyright owner. Further reproduction prohibited without permission.

compressive stress σ_x = -236.8 MPa and vertical stress $\sigma_y = 0$. The out-of-plane stress is

$\sigma_z = \nu(\sigma_x + \sigma_y)$ = -78.1 MPa due to plane strain assumption.

Table 4.1. Values of parameters used in the stress relaxation modeling of periodic copper grain array to compare numerical and theoretical predictions.

Parameter	Value
Grain width d	100 nm
Burgers vector b	0.25 nm
Grain boundary region thickness δ	1 nm
Atomic volume Ω	$1.18 \cdot 10^{-29}$ m^3
Melting temperature T_m	1356 K
Young's modulus E	128 GPa
Poisson's ratio ν	0.33
Grain interior vacancy diffusion pre-exponential D_{0L}	$2 \cdot 10^{-5}$ m^2/s
Grain interior activation energy for vacancy motion $Q_{m,b}$	113.3 kJ/mole
Grain boundary vacancy diffusion pre-exponential $\delta_e D_{0gb}$	$5 \cdot 10^{-15}$ m^3/s
Grain boundary activation energy for vacancy motion $Q_{m,gb}$	67.98 kJ/mole
Grain boundary activation energy for vacancy formation Q_f	83.7 kJ/mole

According to the coupled formulation presented in Chapter 2, the material flows towards the interfaces with the lowest magnitude of interfacial normal stress. For the periodic grain array considered in this chapter, the smallest magnitude of normal stress is at the free surface. Thus we expect the evolution of the deformed shape during stress relaxation as schematically illustrated in Figure 4.2(b).

Reproduced with permission of the copyright owner. Further reproduction prohibited without permission.

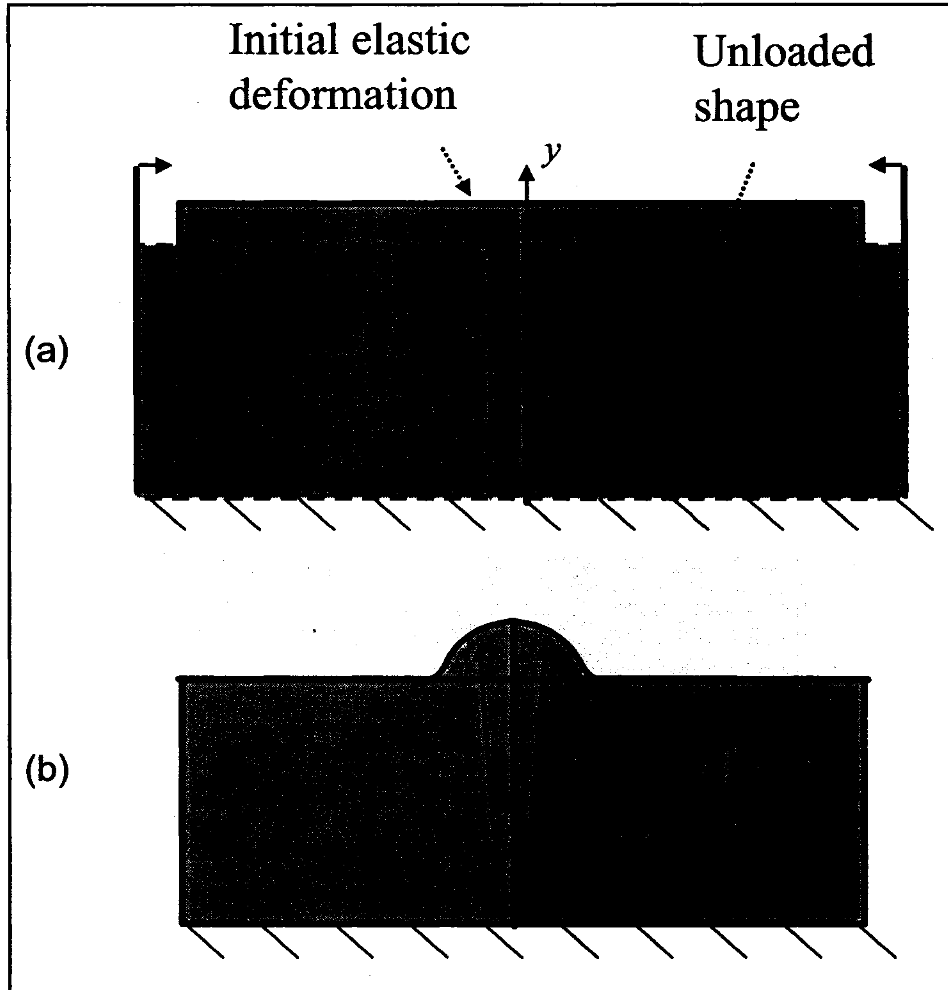

Figure 4.2. Periodic grain array subjected to fixed strain. (a) Initial purely elastic deformation after instantaneous application of ε_x at time t = 0. (b) Schematic of expected evolution of free surface profile due to mass flow.

4.1.2. Evolution of stress field in the grain array

We assume that the time dependence of stress averaged over volume V $\langle\sigma_{xx}\rangle = 1/V \int_V \sigma_{xx} dV$ can be approximated by Maxwell model relaxation function

$$\langle\sigma\rangle = \langle\sigma_0\rangle \exp(-t/\tau) \tag{4.1}$$

Reproduced with permission of the copyright owner. Further reproduction prohibited without permission.

where τ is the Maxwell model relaxation time and $\langle\sigma_0\rangle$ is the average stress at time t = 0. Relaxation time τ corresponds to $\langle\sigma\rangle/\langle\sigma_0\rangle = e^{-1}$, i.e. approximately 63% of averaged stress relaxation. We use the concept of relaxation time to characterize the time period of relaxation of average stress in the model and to scale the time t in the graphs throughout the rest of this section.

Figure 4.3 shows the stress σ_{xx} distribution along the internal grain boundary at different time instances ($t = 6\cdot10^{-4}\tau$, 0.01τ, 0.1τ and 0.5τ) at two different temperatures ($T = 0.3T_m$ and $0.7T_m$, where $T_m = 1356\,K$ is the melting temperature of Cu). It can be seen that the stress relaxation occurs almost instantaneously at the junction between grain boundary and free surface, and gradually advances along the internal grain boundary. We observe that the stress gradients are lower at high temperatures. This effect may be attributed to the contribution of Nabarro-Herring mechanism towards stress relaxation. Note that relaxation time τ is different for different temperatures, for example $\tau \sim 1$ s for $T = 0.5T_m$ and $\tau \sim 0.001$ s for $T = 0.7T_m$. Such variation is due to the fact that the vacancy diffusivities are strongly dependent on temperature and the diffusional creep strain rate responsible for stress relaxation is much higher at elevated temperatures.

We expect that the choice of tensile or compressive direction for externally applied strain affects the directions of elastic displacements and vacancy fluxes rather than their magnitudes. Therefore we assume that the predictions of time evolution for non-dimensionalized horizontal stress σ_{xx}/σ_0 are approximately the same for compression and tension. With this assumption at hand, we compare our results to the predictions for the polycrystalline film subjected to tensile externally applied strain

Reproduced with permission of the copyright owner. Further reproduction prohibited without permission.

according to the model of grain boundary diffusion wedges (Gao et al. [17]). Their model is schematically illustrated in Figure 4.4. The normal tractions on internal grain boundary were assumed to be relaxed by transporting the crack-like wedges from free surface into the grain boundary. The integro-differential eigenvalue problem was formulated to obtain the solution for opening displacement of the crack-like wedges and calculate the corresponding evolution of stress along the internal grain boundary. The stresses reported by Gao et al. [17] are depicted by triangles for time instances 0.01 τ and 0.1 τ in Figure 4.3, and demonstrate good correspondence of results obtained by two different methods.

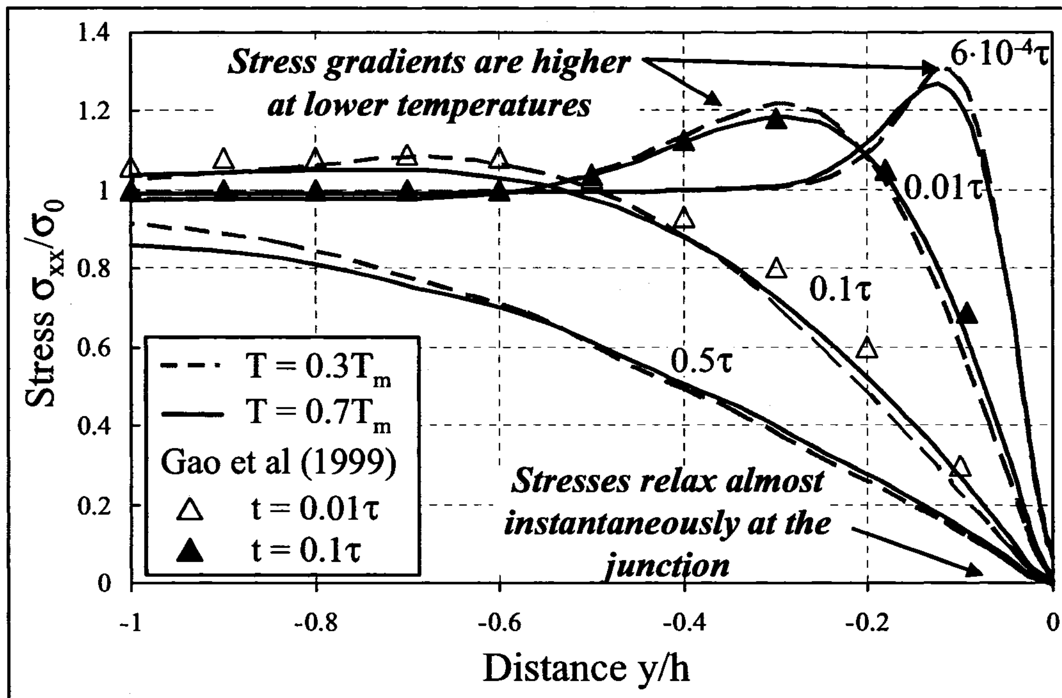

Figure 4.3. Evolution of normal stress distribution along the internal grain boundary (x = 0) at temperatures $T = 0.7T_m$ (solid lines) and $T = 0.3T_m$ (dashed lines). Predictions of Gao et al. [17] shown by triangles are reported as approximately independent of temperature.

As seen in Figure 4.3, the difference in stress evolution at different temperatures is not substantial for a one-dimensional array of grains. Hence the relaxation of average

Reproduced with permission of the copyright owner. Further reproduction prohibited without permission.

stress $\langle \sigma_{xx} \rangle$ as a function of t/τ can be plotted as a single curve, see Figure 4.5. The insets illustrate the time evolution of stress distribution σ_{xx} in the grain.

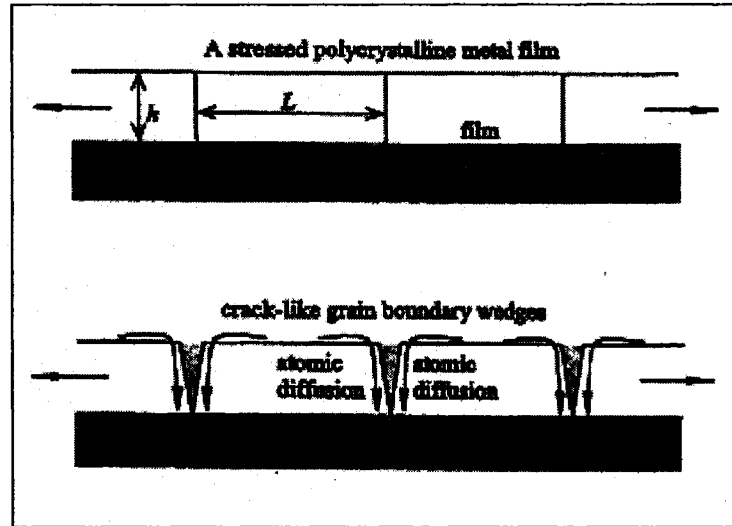

Figure 4.4. Grain boundary diffusion wedge model of polycrystalline film subjected to uniform externally applied strain (Gao et al. [17]).

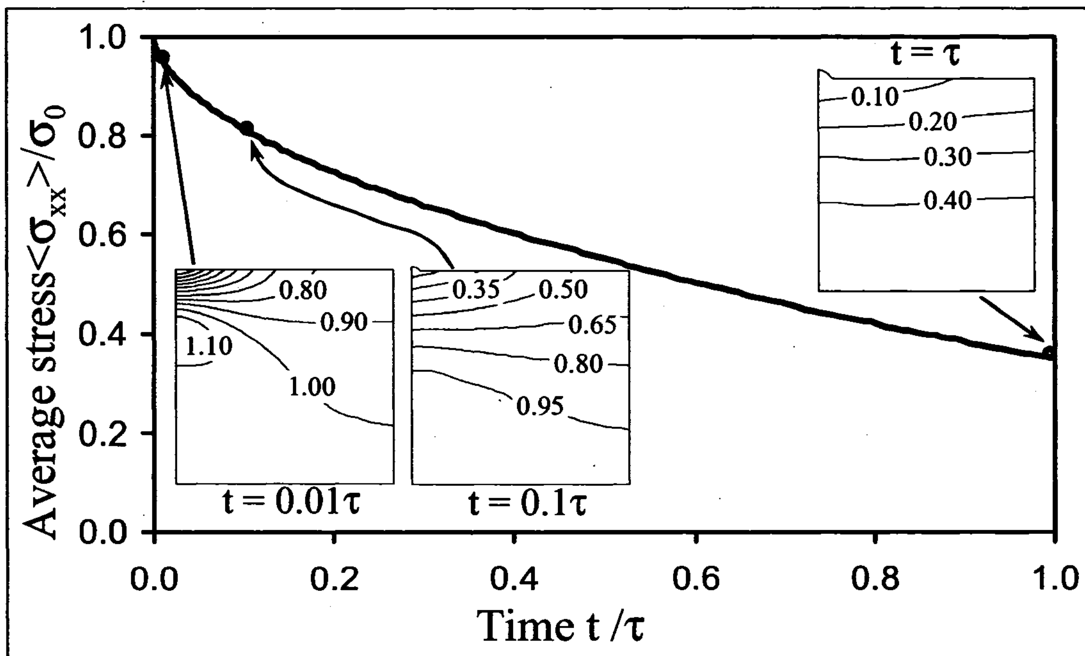

Figure 4.5. Relaxation of average stress $\langle \sigma_{xx} \rangle$. Insets show the distribution of σ_{xx} at selected time instances.

Reproduced with permission of the copyright owner. Further reproduction prohibited without permission.

4.1.3. Temperature dependence of free surface profile and contribution of Nabarro-Herring and Coble creep mechanisms

The free surface profiles resulting from the accumulation of material along the free surface due to stress-driven mass flow at various temperatures are shown in Figure 4.6. The lump at the grain junction region results from material migration along the grain boundary (Coble mechanism). The height of the lump is approximately the same for all considered temperatures. This observation can be explained by the fact that the increased diffusivity at elevated temperatures is compensated by higher rate of vacancy flow according to Fick's law (2.7). We also observe the increased accumulation of material along the free surface at high temperatures ($T > 0.5T_m$). This effect can be explained by contribution of vacancy diffusion in the grain interior (Nabarro-Herring mechanism).

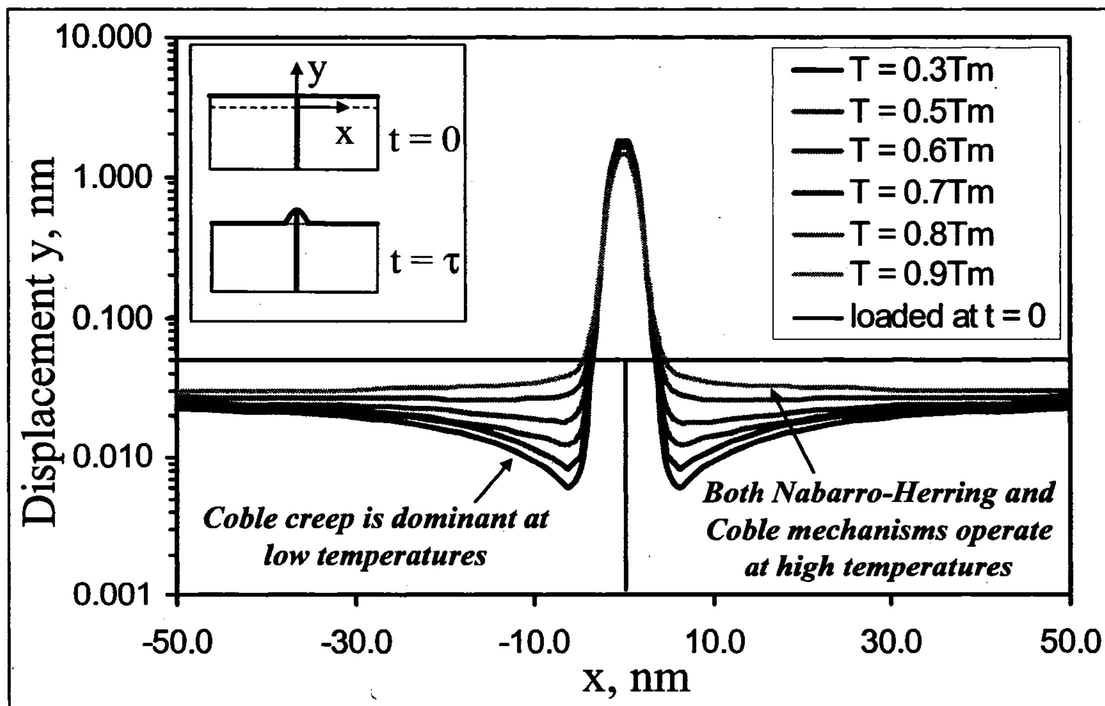

Figure 4.6. Free surface profile at time $t = \tau$ for stress relaxation at different temperatures.

Reproduced with permission of the copyright owner. Further reproduction prohibited without permission.

4.1.4. Estimate of relaxation time

The finite element prediction of relaxation curve for average stress shown in Figure 4.5 can be conveniently approximated by Maxwell model relaxation function given by Eq. (4.1). Maxwell model is an idealized model of a viscoelastic material that consists of linear elastic spring element and linear viscous dashpot element connected in a series, as in Figure 4.7. The stress-strain relation of spring and stress-strain rate relation of dashpot are, respectively

$$\sigma = E\varepsilon \tag{4.2}$$

$$\sigma = \eta\dot{\gamma} \tag{4.3}$$

where E is the Young's modulus of the spring and η is the dashpot viscosity. The relaxation time τ used in Maxwell model relaxation function (4.1) can be estimated as

$$\tau = \eta / E \tag{4.4}$$

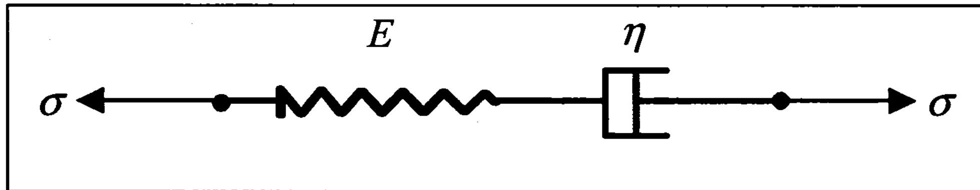

Figure 4.7. Maxwell model of a solid.

Using Eq. (4.4), it is possible to obtain the theoretical estimate of relaxation time according to classical dimensional creep models of Nabarro-Herring and Coble. For simultaneously acting Nabarro-Herring and Coble creep mechanisms, the creep rate formula is given by Frost and Ashby [49] as

$$\dot{\gamma} = \frac{42\sigma\Omega}{kTd^2} D_L \left(1 + \pi \frac{\delta_e D_{gb}}{dD_L} \right) \tag{4.5}$$

Reproduced with permission of the copyright owner. Further reproduction prohibited without permission.

where $\dot{\gamma}$ is the diffusional creep strain rate, d is the grain width, δ_e is the effective thickness of the grain boundary (on the order of magnitude of Burgers vector b) and σ is the applied stress. Note that the diffusivities D_L and D_{gb} in (4.5) are based on the energy of both formation and motion of vacancies

$$D_L = D_{0L} \exp\left(-\frac{Q_{m,b} + Q_f}{kT}\right) \tag{4.6}$$

$$\delta_e D_{gb} = \delta D_{0gb} \exp\left(-\frac{Q_{m,gb} + Q_f}{kT}\right) \tag{4.7}$$

These diffusivities are different from the "vacancy motion only" diffusivities $D_{v,b}$ and $D_{v,gb}$ used in our finite element formulation. The effect of vacancy formation energy Q_f is considered in the finite element approach through Eqs. (2.5)-(2.6) for stress dependence of equilibrium vacancy concentration.

We obtain the theoretical estimate of relaxation time τ from Eqs. (4.3)-(4.5) as

$$\tau = \frac{1}{E}\left[\frac{42\Omega}{kTd^2} D_L \left(1 + \pi \frac{\delta D_{gb}}{d D_L}\right)\right]^{-1} \tag{4.8}$$

The estimate of τ from Eq. (4.8) is compared to the finite element predictions in Figure 4.8. To obtain the relaxation time from the finite element solution, we have performed a number of stress relaxation simulations for a range of temperatures between $0.3T_m$ and T_m. The numerical prediction of τ is estimated by fitting the exponential function (4.1) to the FEA average stress relaxation curve.

Figure 4.8 shows good agreement of theoretical (Frost and Ashby [49] results combined with Maxwell model) and numerical predictions for stress relaxation time. The largest difference is in the range of 600-900 K, and does not exceed 30% of theoretical

Reproduced with permission of the copyright owner. Further reproduction prohibited without permission.

values. Note that the creep strain rate in Eq. (4.5) accounts for the contribution of both Nabarro-Herring and Coble mechanisms to creep rate, which is consistent with the finite element computations performed in this chapter since both diffusion within grain interior and grain boundary region contributes to the mass flow.

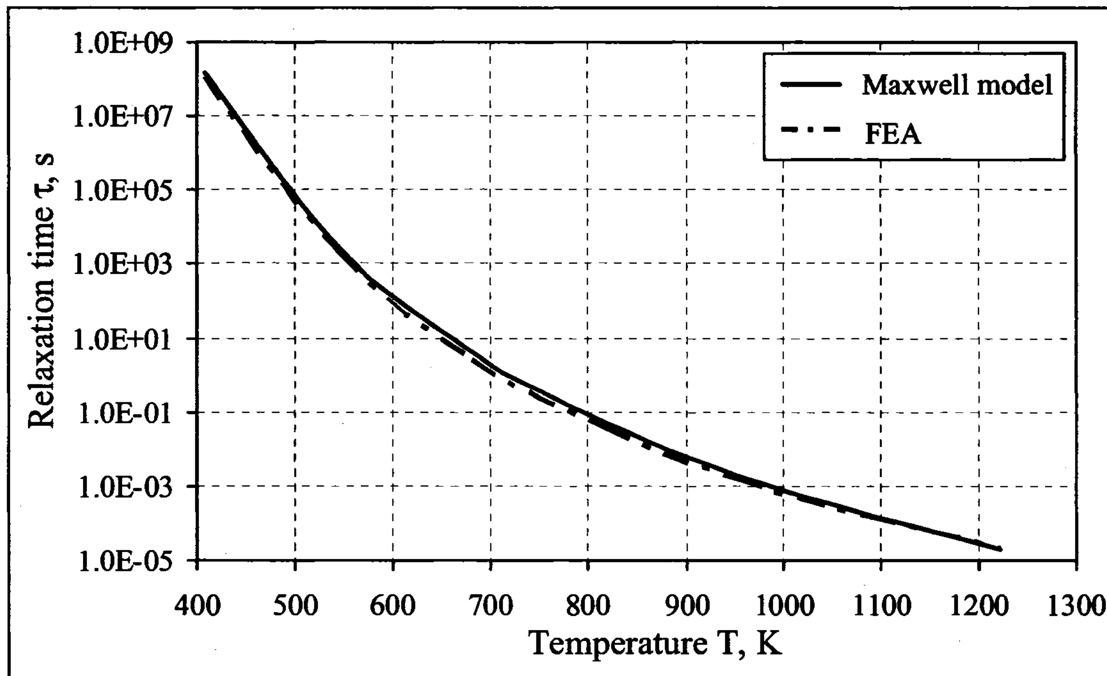

Figure 4.8. Comparison of diffusional creep theoretical estimate of relaxation time τ to the finite element predictions.

4.2. Diffusional creep in 3x3 grain assembly

The classical models of Nabarro, Herring and Coble diffusional creep (Nabarro [8], Herring [9], Coble [10]) provide the analytical expressions for macroscopic diffusional creep rate of a polycrystalline material. These expressions are derived by considering a single grain of idealized shape assuming that the macroscopic body is represented by infinitely periodic grain arrangement. In this section, we study the dependence of macroscopic creep rate on grain size and grain boundary region thickness

Reproduced with permission of the copyright owner. Further reproduction prohibited without permission.

using the FEA modeling approach presented in the previous chapter. To ensure that the finite element model predictions can be compared to the response from classical dimensional models, we need to reduce the effect of boundaries in the FEA simulation. For this purpose, we consider the simplified two-dimensional plane strain model of 3x3 copper grain assembly. The response of internal grain is assumed to represent the behavior of individual grain within a polycrystal.

4.2.1. Evolution of tractions on internal grain boundaries

Let us consider the creep of an idealized two-dimensional (plane strain) periodic array of square grains subjected to biaxial externally applied stress as shown in Figure 4.9. The external loading consists of compressive stress σ applied horizontally and tensile stress of the same magnitude applied vertically. Due to the symmetry of the square grain shape, it is possible to consider only a quarter of the model with appropriate displacement and vacancy flux boundary conditions. Uniform isotropic elastic properties are assumed. The Young's modulus, Poisson ratio and other parameters used in this computation are specified in Table 4.2. Note that the 100 nm thickness of grain boundary region is physically unrealistic and is used in this work exclusively for subsequent comparison of internal grain boundary tractions to the published predictions of Garikipati et al. [26].

We assume initial stress in the solid to be equal to zero. Application of external load results in purely elastic deformation and initially uniform stress state. Creep strains accumulating with time result in the horizontal contraction and vertical elongation of each individual grain in the periodic array while the rectangular shape of the grains is preserved. Thus, to model the periodic grain array, we need to ensure that the grains

Reproduced with permission of the copyright owner. Further reproduction prohibited without permission.

adjacent to the boundary of the 3x3 grain assembly are properly constrained. For this purpose we employ multipoint constraints for the top, bottom and lateral surfaces of the 3x3 grain model.

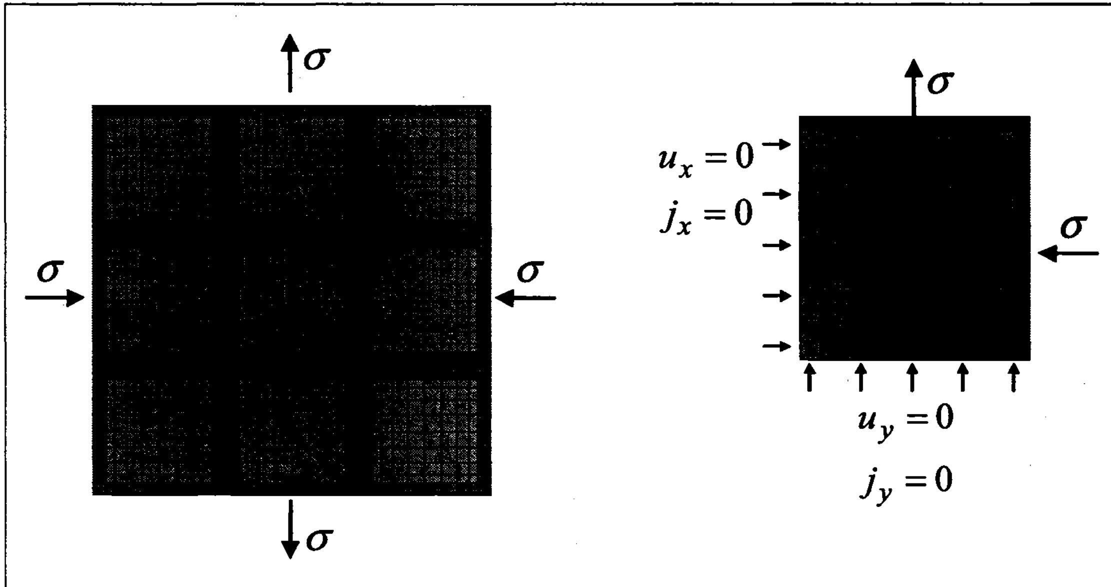

Figure 4.9. FEA model of 3x3 grain assembly. Symmetry allows to reduce the number of elements in the model by 75 %.

The contour plots in Figure 4.10 present the stress field at time $t = 500$ s for external load $\sigma_{ext} = 60$ MPa applied to the grain assembly containing the grains of size 1 μm. Finite element simulation results show that the magnitude of normal stress on the plane orthogonal to the direction of a grain boundary is rapidly decreasing in grain boundary regions due to diffusional creep strains. The behavior of traction normal to the boundary of center grain is shown in Figure 4.11 at time $t = 500$ s. Since the externally applied load is constant, the reduction of traction in the vicinity of the grain boundary junctions is compensated by the increase of traction in the central part of the grain.

Reproduced with permission of the copyright owner. Further reproduction prohibited without permission.

Table 4.2. Numerical values of parameters for creep response modeling of 3x3 grain assembly to compare the model predictions to the results of Garikipati et al. [26].

Parameter	Value
Grain width d	1 μm
Grain boundary region thickness δ	100 nm
Externally applied traction σ_{ext}	60 MPa
Temperature T	473 K
Young's modulus E	60 GPa
Poisson's ratio ν	0.3
Vacancy diffusion pre-exponential D_{0L}	$2 \cdot 10^{-5}$ m^2/s
Grain interior activation energy for vacancy motion $Q_{m,b}$	64.7 kJ/mole
Grain boundary activation energy for vacancy motion $Q_{m,gb}$	60.1 kJ/mole

We provide the comparison of our finite element predictions to numerical computations presented in Garikipati et al. [26] for the model with the same geometry and elastic material properties. The diffusion is considered by Garikipati et al. [26] using the concept of chemical potential and spatial distribution of vacancy formation energy (rather than vacancy motion energy, as in our model). The values for vacancy motion activation energies in our computation are taken based on their published vacancy formation energy parameters.

The finite element approach adopted by Garikipati et al. [26] is based on the formulation of coupled elasticity and vacancy flow problems and subsequent staggered numerical solution of the governing equations. However, they assume that the grain boundaries as sources/sinks of vacancies have a certain strength, or effectivity. Note that the finite element prediction of traction evolution in our model has been obtained assuming that the grain boundaries act as infinite sources/sinks of vacancies. In Garikipati's approach, the vacancy flow governing equation (2.8) is modified to include the vacancy source/sink term

Reproduced with permission of the copyright owner. Further reproduction prohibited without permission.

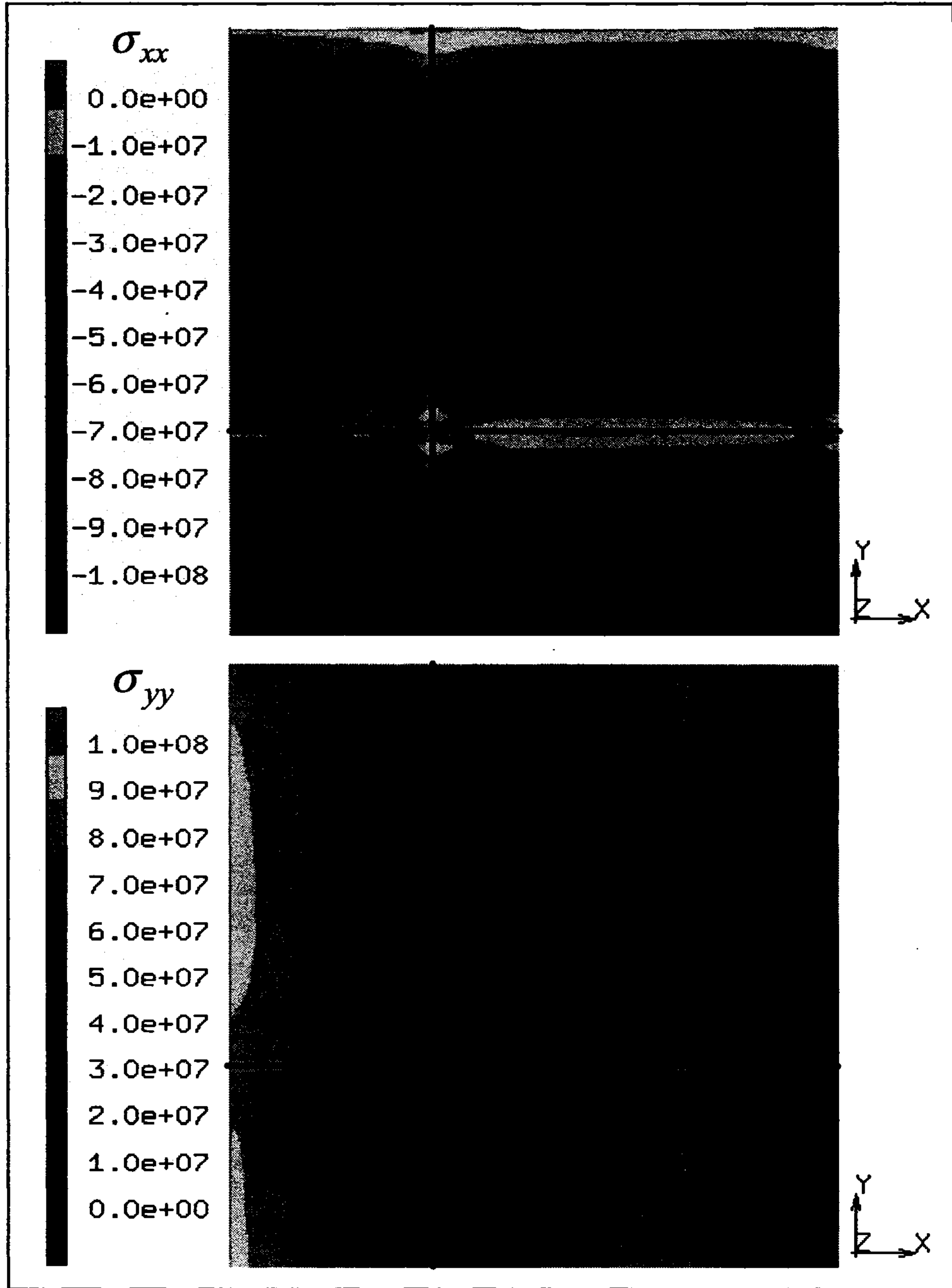

Figure 4.10. Stress distribution at time $t = 500$ s in 3x3 grain assembly subjected to externally applied biaxial traction. Parameters for this computation are specified in Table 4.2.

Reproduced with permission of the copyright owner. Further reproduction prohibited without permission.

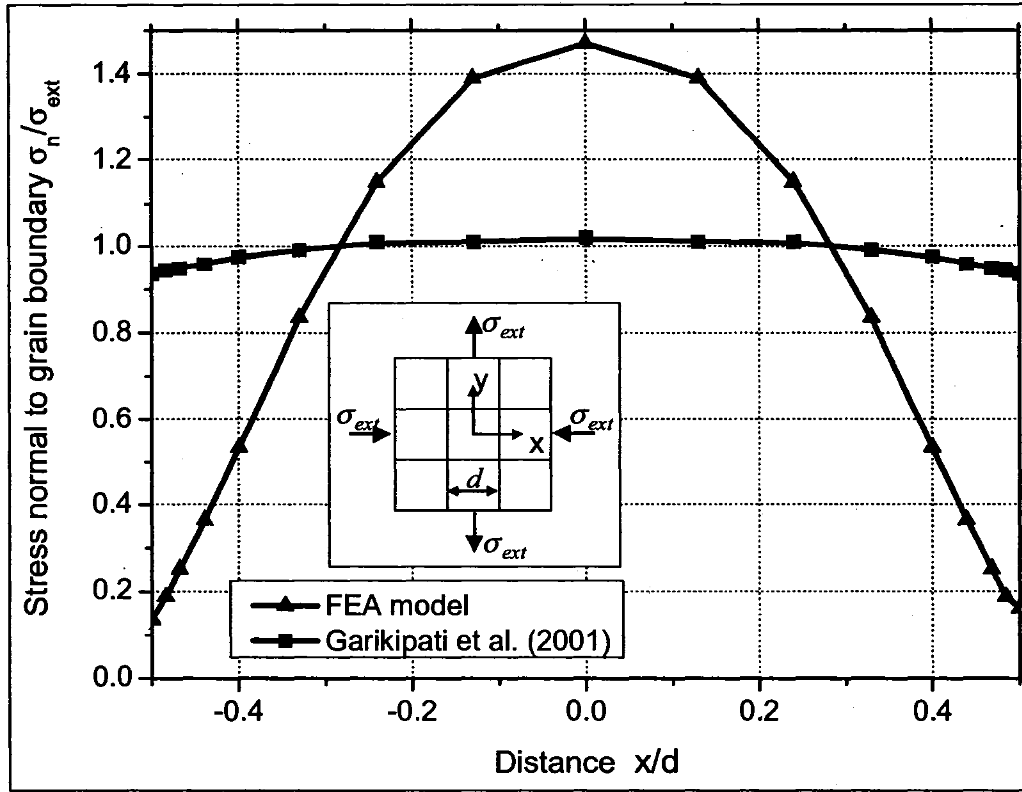

Figure 4.11. Traction normal to internal grain boundary of center grain at time $t = 500$ s.

$$\frac{\partial C_v}{\partial t} + \nabla \cdot \mathbf{j}_v + \frac{1}{\tau}\left(C_v - C_v^{eq}\right)\chi = 0 \tag{4.9}$$

Here, $\chi = 1$ at grain boundaries and $\chi = 0$ elsewhere. Large values of parameter τ are used to specify a slow-acting source/sink and smaller values of τ results in a more rapidly acting source/sink. Even though the normal stress averaged over the grain boundary is predicted to be approximately the same in both simulations, the approach of Garikipati et al. [26] predicts slower evolution of grain boundary traction, as shown in Figure 4.11. A possible explanation of this behavior is the finite value of vacancy source/sink strength used in their calculations, in addition to the different theoretical

Reproduced with permission of the copyright owner. Further reproduction prohibited without permission.

background for vacancy diffusion treatment in their approach. We also note that the redistribution of traction along the internal grain boundary is moderate compared to the model with infinite sources/sinks of vacancies, since the tractions on internal boundaries are not decreasing to zero value at the grain boundary junctions.

4.2.2. Dependence of diffusional creep rate on grain size

Grain size is one of the parameters that affect creep in metals. Burton and Greenwood [59] provided the experimental evidence for Nabarro-Herring and Coble creep rate dependence on grain size. This effect is also present beyond the range of stresses and temperatures where diffusional creep is believed to be dominant, as observed by Wilshire and Palmer [60].

To study the dependence of diffusional creep rate predictions on grain size for our modeling approach, we perform finite element simulations for the 3x3 grain assembly shown in Figure 4.9. The elastic and diffusion properties of the material are specified in Table 4.1. Series of computations is performed for various values of grain size subjected to externally applied load $\sigma_{ext} = 100$ MPa at temperature 673 K.

Figure 4.12 shows how the numerical predictions of creep rate depend on grain size. Since for all considered cases of grain size the grain boundary region thickness was taken as 1 nm, the fraction of GB region varies from 36% to 0.8% for the grain size range of 10-500 nm. Dashed lines in Figure 4.12 correspond to analytical predictions of Nabarro-Herring and Coble given by the first and second term of Eq. (4.5), correspondingly. As can be seen, the FEA results for smaller grain size are in good agreement with the Coble creep predictions of $1/d^3$ dependence of creep rate. Note that

Reproduced with permission of the copyright owner. Further reproduction prohibited without permission.

the behavior of nanoscale Cu grains is of practical interest as the current technology is capable of manufacturing the first level interconnect lines having thickness on the order of 100 nm. These lines typically exhibit the bamboo structure, i.e. single grain per line width, which is caused by abnormal grain growth in electroplated Cu (see, for example, Harper et al. [61]).

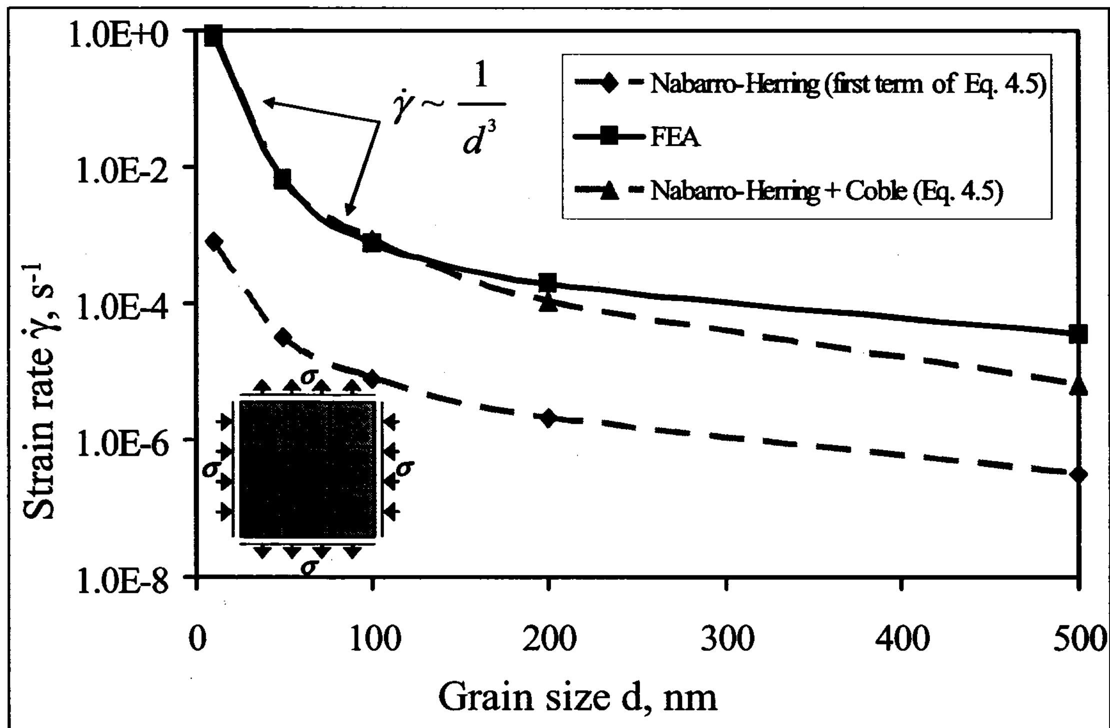

Figure 4.12. Creep rate dependence on grain size at temperature T = 673 K and applied stress 100 MPa. Comparison of finite element results to theoretical predictions of Nabarro-Herring and Coble.

4.2.3. Effect of grain boundary thickness on diffusional creep rate predictions

To illustrate how the choice of GB region thickness affects the predicted creep rate, we have varied the value of this parameter from b to $8b$ for the grain size of 100 nm, where b is the length of Burgers vector for copper. The finite element simulations

Reproduced with permission of the copyright owner. Further reproduction prohibited without permission.

are performed for the 3x3 grain assembly shown in Figure 4.9. The model subjected to externally applied load $\sigma_{ext} = 100$ MPa at temperature 673 K. Elastic and diffusion properties of the material are specified in Table 4.1. The results of numerical simulations presented in Figure 4.13 show that the increase in grain boundary region thickness, which results in larger area of enhanced vacancy flow, facilitates diffusional creep in the grain. Note that the theoretical predictions of Coble creep model can be affected in a similar way when parameter δ of Eq. (4.5) is varied. We have assumed that δ is equal to the magnitude of Burgers vector of copper [49] to obtain Coble creep model strain rate shown in Figure 4.13. Since measured values of GB thickness for polycrystalline Cu are not readily available, it is recommended to calibrate the FEA models for this parameter using the appropriate experimental data.

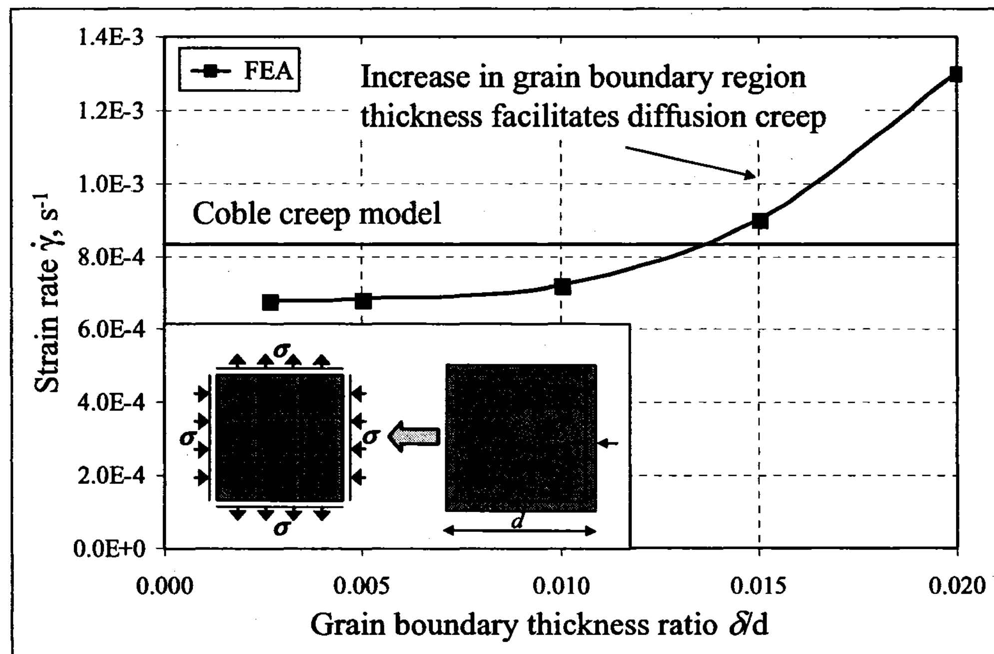

Figure 4.13. Creep rate dependence on the choice of grain boundary region thickness for the 100 nm grain.

Reproduced with permission of the copyright owner. Further reproduction prohibited without permission.

CHAPTER 5

SEVERAL EXAMPLES OF FINITE ELEMENT PREDICTIONS OF STRESS RELAXATION IN TYPICAL COPPER INTERCONNECT STRUCTURES

In this chapter we apply the coupled elasticity-mass flow finite element technique to predict the stress relaxation response in copper interconnect structures. The behavior of interconnects is of practical interest for microelectronics industry. Interconnect lines are encapsulated and annealed at high temperatures up to 400 °C. Due to the mismatch of thermal expansion coefficients of Cu, Ta, dielectric and passivation materials, high stresses develop during processing stage that may lead to the initiation of voids and cracks while the circuit is heated to elevated temperature and then cooled to room temperature. To control the stress state in copper lines during the processing stage, it is of practical interest to predict the time needed for stress relaxation of Cu interconnect lines at elevated temperatures.

We apply our approach to predict the stress field evolution with time. During the stress relaxation modeling, we study the accumulation of material at the free surface. We also provide the FEA computations that reveal the dependence of stress relaxation on the activation energy for vacancy motion in the grain boundary region as an adjustable parameter of the finite element model.

Reproduced with permission of the copyright owner. Further reproduction prohibited without permission.

5.1. Modeling of single-level structure subjected to thermal load

A typical single-level copper interconnect structure is shown in Figure 5.1. The figure shows the periodicity cell assuming the structure is periodic in the horizontal direction. We can assume plane strain model since the length of a typical interconnect line is about an order of magnitude larger than line thickness and width. Copper is encapsulated in thin Ta layer which acts as the diffusion barrier between Cu and dielectric. For simplicity, we consider the case of a single Cu grain per line width. This is typical for nanoscale interconnect structures with line thickness less than 100 nm. We will consider both cases of free surface and passivation layer on top of Cu in a typical interconnect structure. Table 5.1 adapted from [3] lists the properties of the materials in a typical interconnect line.

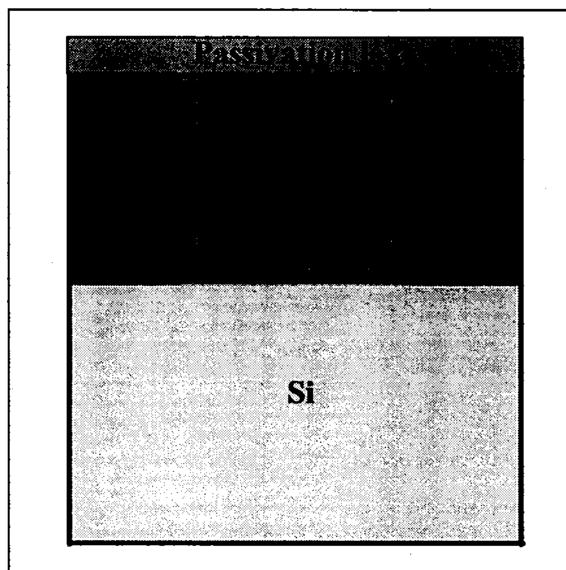

Figure 5.1. Schematic illustration of cross-section of a typical single-level interconnect structure.

Note that the selection of dielectric material is an important design parameter that affects the performance and reliability of integrated circuits. The current trend in

Reproduced with permission of the copyright owner. Further reproduction prohibited without permission.

microelectronics industry is to select the dielectric material with lower dielectric constants to minimize the product of interconnect line resistance and capacitance (RC) which is responsible for signal propagation delay. Low-k dielectrics have low Young's moduli and high coefficients of thermal expansion, which makes the integrated circuits susceptible to failure and necessitates additional research on reliability of such structures.

Table 5.1. Mechanical properties of materials used in a typical interconnect line.

Material	Young's modulus E (GPa)	Poisson's ratio ν	CTE (ppm/K)
Copper (Cu)	128	0.36	16.5
Tantalum (Ta)	186	0.34	6.5
Silicon dioxide (SiO_2)	66	0.25	2.5
Low-k dielectric	~1-10	~0.3	~10-100
Silicon (Si)	165	0.22	2.3

5.1.1. Elastic stress field in interconnect lines subjected to thermal load

We begin this chapter by studying the difference in the character of stress and deformation between the previous technology where SiO_2 was used as the dielectric, and current technology where low-k dielectric material is used. The FEA modeling is performed for the sample structure with the geometry shown in Figure 5.2a. It is assumed that the structure is initially stress-free at room temperature T = 293 K. We assume that the thermal expansion of the Si base layer is not constrained. Therefore the stress state in the Si wafer is zero at elevated temperatures with the exception of the thin layer on top of Si where the back-end interconnect lines and front-end devices are located. To model the thermomechanical loading for the single-level interconnect structure, it is necessary to apply both the increase in temperature ΔT and the horizontal displacement

Reproduced with permission of the copyright owner. Further reproduction prohibited without permission.

$\Delta u_x = (1+\nu_{Si})\alpha_{Si} L \Delta T$ which is the kinematic constraint that arises due to the thermal expansion of the Si base layer. The coefficient $(1+\nu_{Si})$ arises due to the plane strain assumption. Using the symmetry of the periodic structure we model only a half of the interconnect line. The mechanical boundary conditions are shown in Figure 5.2b.

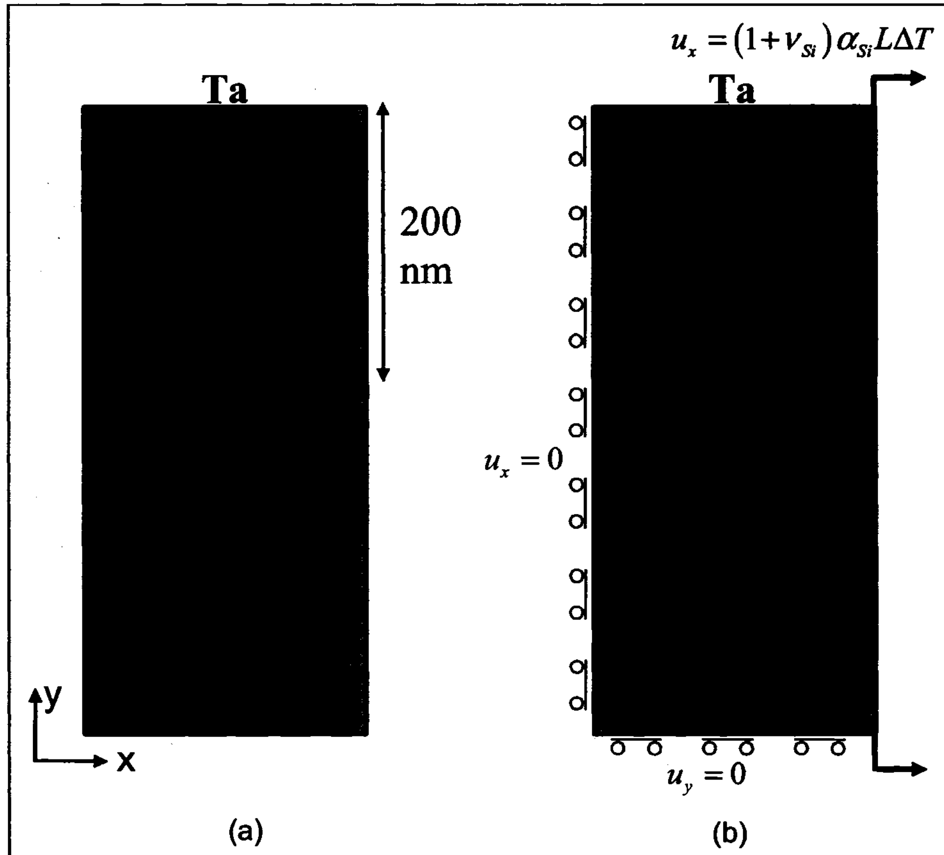

Figure 5.2. Two-dimensional plane strain model of periodic interconnect unit cell. (a) Geometry and (b) thermomechanical loading.

We model the response of the structure to applied temperature increment ΔT = 380 K which gives rise to thermal strains and stresses due to the mismatch in thermal expansion coefficients of interconnect line materials. The Young's modulus, Poisson's ratio and CTE of low-k material are taken as $E = 2.5$ GPa, $\nu = 0.34$ and $\alpha = 60$ ppm/K.

Reproduced with permission of the copyright owner. Further reproduction prohibited without permission.

Figures 5.3-5.5 illustrate the stress σ_{xx}, σ_{yy} and σ_{xy} as well as the deformed shape of thermally loaded interconnect structure. The results are obtained using the FEA mesh with 715 elements. Due to significant difference in elastic properties and coefficients of thermal expansion, the deformation of low-k dielectric material is much larger than the deformation of SiO_2, which results in opposite direction of grain boundary sliding. We also note higher stress σ_{xx} at the free surface-Cu-Ta junction for the low-k dielectric structure compared to the stress in SiO_2 structure. Thermal stress σ_{yy} is approximately 2 times larger in the structure containing low-k material.

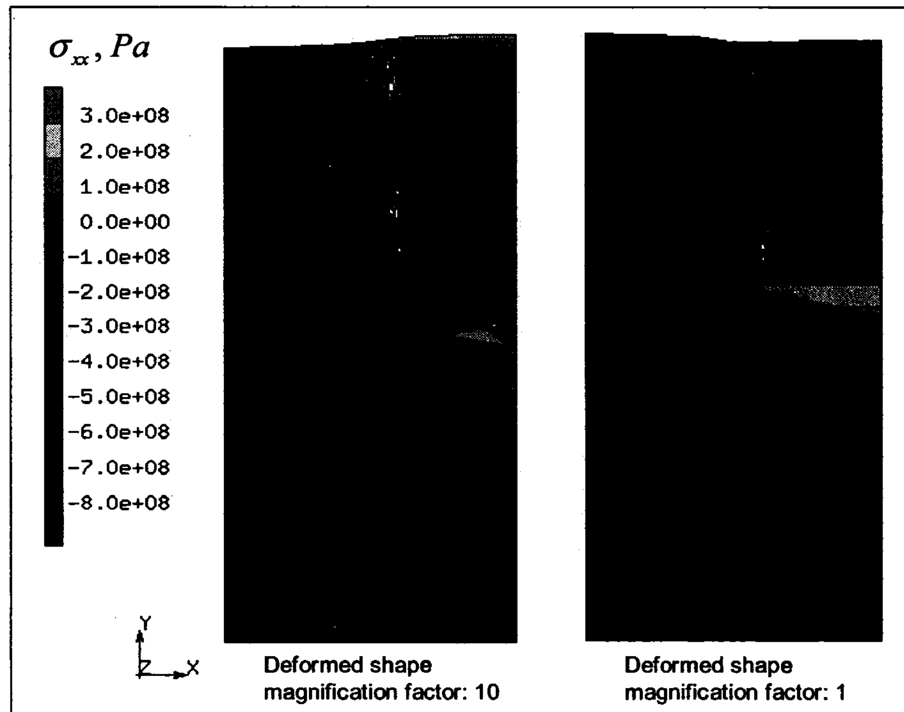

Figure 5.3. Contour plots of stress σ_{xx} in thermally loaded single-level interconnect structure.

Reproduced with permission of the copyright owner. Further reproduction prohibited without permission.

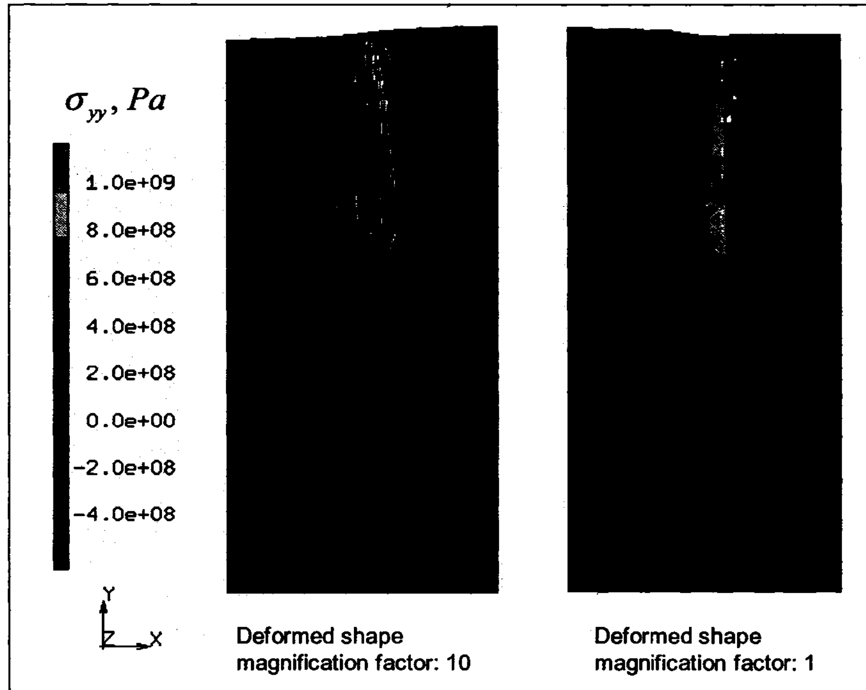

Figure 5.4. Contour plots of stress σ_{yy} in thermally loaded single-level interconnect structure.

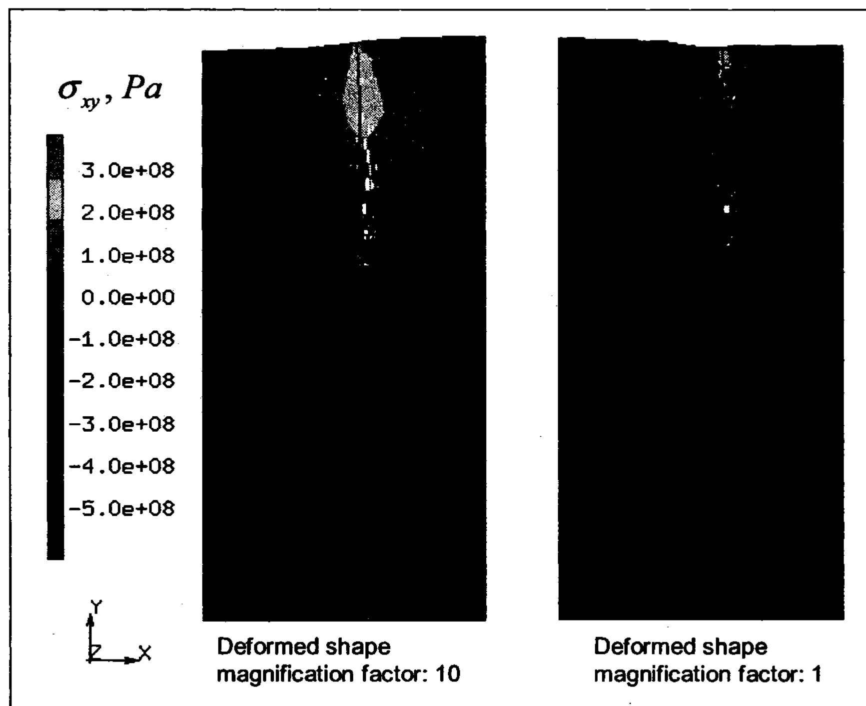

Figure 5.5. Contour plots of stress σ_{xy} in thermally loaded single-level interconnect structure.

Reproduced with permission of the copyright owner. Further reproduction prohibited without permission.

5.1.2. Modeling of transient stress relaxation using coupled finite element approach

After the integrated circuit is thermally loaded, relaxation of thermal stresses in interconnect lines occurs with time. Stress relaxation can be attributed to various mechanisms, including diffusional creep and grain boundary sliding. In this chapter we study only the effect of diffusional mass flow on stress relaxation. We consider the test structure shown in Figure 5.2 with SiO_2 selected as the dielectric material. The mechanical properties of interconnect line materials are specified in Table 5.1. To model the stress-driven diffusional mass flow in copper, we select the thickness of enhanced diffusivity grain boundary region to be 1 nm. The vacancy diffusion properties of copper are selected as specified in Table 4.1.

We assume that the structure was initially stress-free at room temperature $T = 293$ K. We model the transient stress relaxation that occurs after the structure is instantaneously subjected to elevated temperature 673 K. Figure 5.6 depicts the evolution of stress σ_{xx} averaged over volume of the structure. Thus the coupled finite element procedure predicts stress relaxation in interconnects when diffusional creep is assumed as the only acting mechanism of nanoscale deformation.

The insets in Figure 5.6 illustrate the accumulation of material at the free surface due to diffusional mass flow. Note that the increased diffusivity in the Cu grain boundary region results in the preferential accumulation of material at the free surface – grain boundary junction. The height of the accumulated material is predicted as ~ 1 nm. Note that due to simultaneously acting diffusional creep and grain boundary sliding it would not be possible to distinguish between these two modes in case experiments are performed to measure nanoscale deformation during thermal cycle. In order to

Reproduced with permission of the copyright owner. Further reproduction prohibited without permission.

experimentally verify the effect of diffusional creep, the FEA simulation that considers both nanoscale deformation mechanisms is needed.

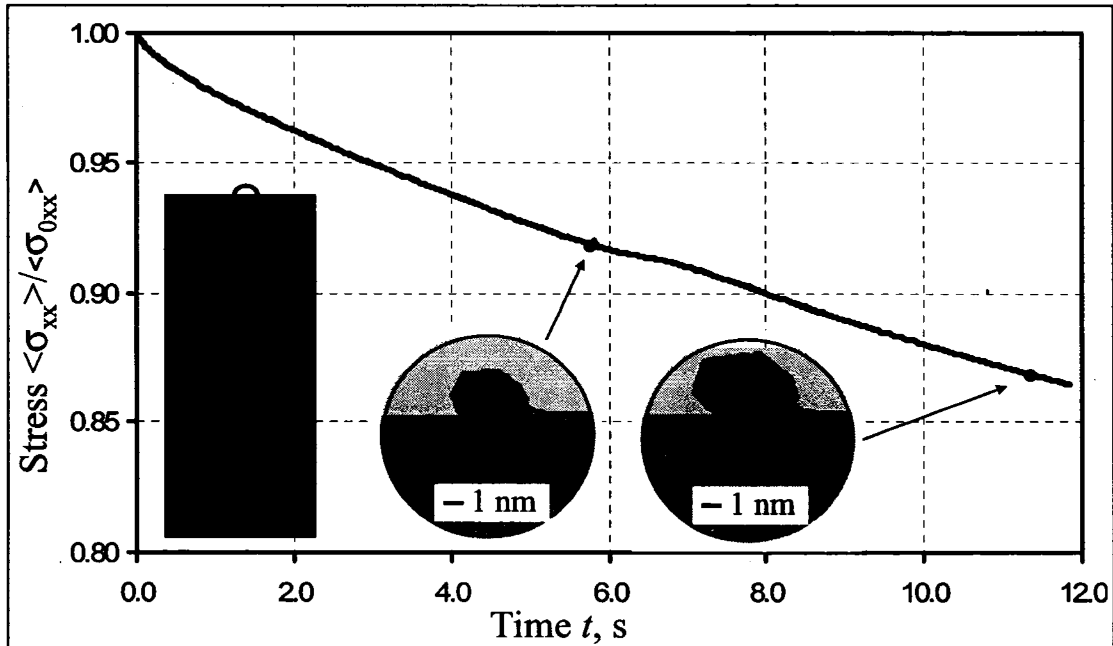

Figure 5.6. Evolution of average stress and deformed shape for a typical Cu-Ta-dielectric structure under thermal loading.

Before we proceed with the study of interconnect stress relaxation dependence on design parameters, it is of interest to compare the finite element predictions to the experimental observations reported in the literature for stress relaxation in copper interconnect lines. We consider the interconnect structure experimentally studied by Singh et al. [29] which is shown in Figure 5.7a. The copper line is encapsulated in a Ta diffusion barrier deposited on top of SiO_2 base layer. SiOF is used as a dielectric. For this material, the Young's modulus is $E = 71.7$ GPa, Poisson's ratio is $\nu = 0.16$ and the coefficient of thermal expansion is

Reproduced with permission of the copyright owner. Further reproduction prohibited without permission.

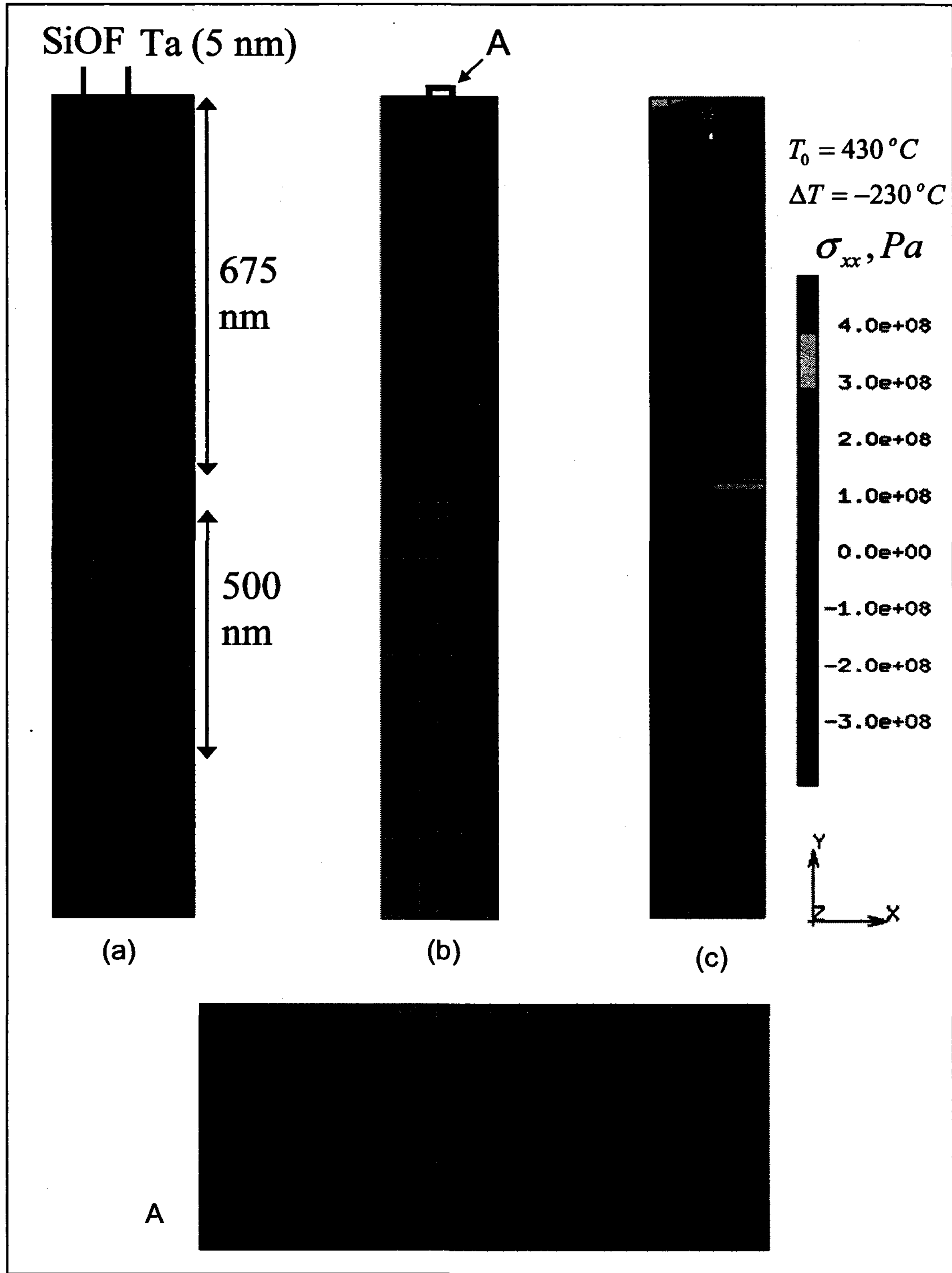

Figure 5.7. Two-dimensional model of periodic interconnect line structure experimentally studied by Singh et al. [29]. (a) Geometry. (b) Finite element mesh. (c) Initial stress σ_{xx} after application of thermal load.

Reproduced with permission of the copyright owner. Further reproduction prohibited without permission.

$\alpha = 0.94$ ppm/K. The structure is periodic in the horizontal direction and only half of the structure needs to be modeled due to symmetry. In the experimental procedure of Singh et al. [29], the specimen was heated from room temperature to 430 °C at the rate of 4 °C per minute. The structure is then thermally annealed at 430 °C, followed by cooling to 200 °C at the rate of 2 °C per minute. Although some stress may be present when the cooling starts, we follow the assumption of Singh et al. [29] that the structure is fully relaxed after the thermal annealing. Therefore the tensile stress is predicted to develop with cooling due to the thermal contraction. The assumptions of zero stress state at 430 °C and instantaneous cooling to 200 °C give a conservative estimate of the stress relaxation time.

Due to large thickness-to-width ratio of the copper line in the specimen and the modeling requirement of 1 nm thickness of the enhanced diffusivity region in copper, the number of elements in the finite element mesh for this model may be on the order of thousands of elements, which makes the calculations very lengthy. We reduce the number of elements by using first order mesh refinement multipoint constraints described in Section 3.2.1 and employing the elements with a large aspect ratio, as shown in Figure 5.7b. The contour plots in Figure 5.7c present the stress field σ_{xx} after the thermal load is instantaneously applied to the structure.

The finite element predictions of average stress relaxation are shown in Figure 5.8 for two values of vacancy motion activation energy in grain boundary region. Note that in order to obtain correspondence with experimental results, we selected the values of vacancy motion energy which are considerably lower than the values reported in the literature (as, for example, in Frost and Ashby [49]). This may be attributed to the

Reproduced with permission of the copyright owner. Further reproduction prohibited without permission.

assumption of our modeling approach to consider diffusional creep as the only mechanism of stress relaxation. We believe that the consideration of grain boundary sliding would facilitate stress relaxation and allow us to use higher values of grain boundary vacancy motion activation energy (between $0.6Q_{m,b}$ and $0.8Q_{m,b}$) to obtain correspondence with experimental predictions.

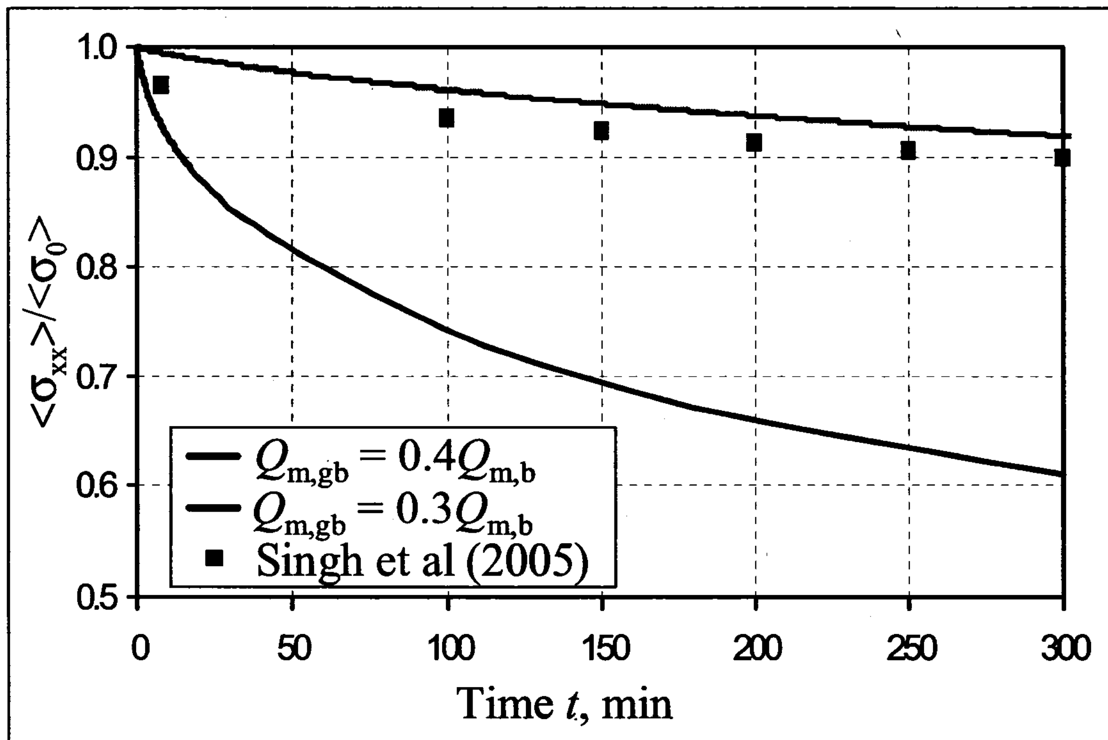

Figure 5.8. Comparison of finite element predictions to experimental results of Singh et al. [29].

Reproduced with permission of the copyright owner. Further reproduction prohibited without permission.

CHAPTER 6

MODELING OF DIFFUSIONAL CREEP CONSTITUTIVE BEHAVIOR WITH EQUIVALENT VISCOPLASTIC FINITE ELEMENTS

In this chapter we describe the numerical technique of equivalent viscoplastic finite elements to improve the computational efficiency of the diffusional creep modeling. We explore the possibility of the mechanical FEA treatment that captures the manner in which the vacancy flow phenomenon affects the stress-strain state in the model. We adopt the approach developed by the classical Nabarro-Herring and Coble theories, where the diffusional creep mechanical response is described with the stress-strain rate constitutive relation. The consideration of the diffusional creep process from purely mechanical point of view must improve the efficiency of computation by reducing the coupled elasticity-mass flow problem to the equivalent mechanical creep analysis.

We perform a series of numerical experiments to explore the variation of the creep behavior throughout the grain and to establish the equivalent creep laws. The numerically obtained creep laws are then applied to model the stress relaxation of Cu grain using the equivalent FEA creep analysis. The predictions of the equivalent model are compared to the stress relaxation results obtained through coupled elasticity-mass flow FEA procedure presented in the previous chapters.

Reproduced with permission of the copyright owner. Further reproduction prohibited without permission.

6.1. Computational challenges of diffusional creep modeling

The direct finite element modeling of diffusional creep for nanoscale copper grains with realistic values of grain boundary (GB) region thickness ($\cong$ 1 nm) requires excessively large amount of computer time. The test computations were made using the high-performance computing server with dual core Intel Xeon 1.8 GHz, 400 MHz front side bus processor and 4 Gb RAM available in the Department of Mechanical Engineering, University of New Hampshire. The simulation of the stress relaxation response for the periodic square grain array described in the previous chapter required the average computer time of 50 hours. The coupled FEA simulation of stress relaxation for typical Cu interconnect structure presented in Chapter 6 took approximately 120 hours.

As noted previously, the transient solution of coupled elasticity-mass flow problem using the procedure presented in Chapter 3 requires small time steps. The key factors that contribute to this requirement include (a) the small size of elements needed to model the 1 nm thick GB region, and (b) the large difference in the diffusivities of GB region and grain interior (see Eq. 3.8). It is possible to enhance the computational efficiency using the equivalent elastoplastic elements to model the region adjacent to the grain boundary.

The proposed equivalent finite elements allow to reduce the computation time by approximating the coupled description of diffusional creep with equivalent mechanical formulation. Therefore the computational efficiency can be increased without changing the FEA mesh used in the coupled simulation. We also consider the equivalent elements that are larger than the thickness of GB region, and represent the grain boundary layer which is understood as both a portion of GB region and the adjacent portion of grain

Reproduced with permission of the copyright owner. Further reproduction prohibited without permission.

interior. There are at least two advantages of using large equivalent elements in the finite element simulation of diffusional creep. First, large maximum allowable time step, which is roughly proportional to the element area according to Eq. (3.8), results in fewer time steps required for the transient simulation. Second, using the elements of larger size leads to the reduction of the number of degrees of freedom in the finite element model, and consequently the reduction of the time needed for the solution of SLE in the finite element procedure.

Large equivalent elements represent the areas with inhomogeneous diffusivities. Such elements must be assigned the effective material properties that provide the diffusional creep response equivalent to the response of the approximated region. In this chapter, we consider two possible ways to introduce the average (or effective) material properties of equivalent elements. The first approach is to approximate the diffusion-based mechanical response of the area adjacent to the grain boundaries with the average or equivalent creep law. An alternative way is to compute effective diffusivities of the grain boundary layer and apply the coupled elasticity-mass flow procedure presented in the previous Chapters to the finite element model containing equivalent elements.

6.2. Mathematical description of diffusional creep constitutive behavior

We note that the creep phenomenon can be treated mechanically if the vacancy flow effects are directly incorporated in the diffusional creep law of the material. The general formula for creep law can be presented as

$$\dot{\varepsilon}^{cr} = F\left(\bar{\sigma}, \bar{\varepsilon}^{cr}, T, t\right) \tag{6.1}$$

Reproduced with permission of the copyright owner. Further reproduction prohibited without permission.

where equivalent creep strain rate $\dot{\bar{\varepsilon}}^{cr}$ is dependent on equivalent stress $\bar{\sigma}$, accumulated equivalent creep strain $\bar{\varepsilon}^{cr}$, temperature T and time t.

The equivalent strain rate, equivalent strain and equivalent stress are computed as

$$\dot{\bar{\varepsilon}} = \sqrt{\frac{2}{3}\dot{\varepsilon}_{ij}\dot{\varepsilon}_{ij}}\ ,\ \bar{\varepsilon} = \sqrt{\frac{2}{3}\varepsilon_{ij}\varepsilon_{ij}}\ ,\ \bar{\sigma} = \sqrt{\frac{3}{2}\sigma_{ij}^{d}\sigma_{ij}^{d}} \tag{6.2}$$

Here, ε_{ij} is the strain tensor, $\dot{\varepsilon}_{ij}$ is the strain rate tensor and σ_{ij}^{d} is the stress deviator defined as

$$\sigma_{ij}^{d} = \sigma_{ij} - \frac{1}{3}\delta_{ij}\sigma_{kk} \tag{6.3}$$

In Eqs. (6.2) and (6.3), summation is performed over repeating indices and δ_{ij} is the Kronecker symbol.

The general creep law equation (6.1) is implemented in MSC.Marc in the form

$$\dot{\bar{\varepsilon}}^{cr} = A\bar{\sigma}^{n} f\left(\bar{\varepsilon}^{cr}\right) g(T) h(t) \tag{6.4}$$

Here, A and n are material constants, and $f\left(\bar{\varepsilon}^{cr}\right)$, $g(T)$, $h(t)$ can be given in the form of a power-law dependence or more general user-supplied function. An alternative way to specify a creep law is to provide the piecewise-linear dependence between equivalent creep strain rate $\dot{\bar{\varepsilon}}$, equivalent stress $\bar{\sigma}$ and, possibly, other variables. In the following sections we explore various methods to approximate the effective (averaged) behavior of Cu within the grain and at the grain boundary by the diffusional creep law in the form of Eq. (6.4) and piecewise-linear $\dot{\bar{\varepsilon}} \sim \bar{\sigma}$ dependence.

Reproduced with permission of the copyright owner. Further reproduction prohibited without permission.

6.3. Effective diffusional creep law for grain boundary layer and grain interior

To establish the effective diffusional creep law we perform the numerical experiment of stress relaxation in the region of interest. Creep strain rate $\dot{\bar{\varepsilon}}$ and stress $\bar{\sigma}$ are averaged over (1) the grain corner region, (2) grain boundary layer and then (3) over the grain interior. We use the computations for one-dimensional linear grain array described in the previous chapter to validate the predictions of equivalent element technique. Therefore, the grain boundary region thickness, temperature and material properties are selected to match the computation described in Section 4.1. Note that the average (or effective) creep law or diffusivity can be dependent on the geometry of the approximated region, i.e. size, aspect ratio, selection of grain boundary thickness, location of the approximated region in the grain and other parameters. The choice of these parameters has to be justified for each particular simulation.

6.3.1. Stress relaxation numerical experiment for grain corner region

At the initial application of compressive load, the vacancy concentration gradient in the square grain array considered previously is the highest at the grain boundary-free surface junction. This effect, combined with the enhanced diffusivity of grain boundary region, results in large creep strain rate in the corner of a square grain model. Besides, intense accumulation of creep strains occurs only in the corner adjacent to the free surface, as shown in Figure 4.6. This leads to additional computational challenges associated with remeshing. It would be a considerable saving of computation time to approximate the diffusional creep response of this area using the equivalent finite element with effective creep law.

Reproduced with permission of the copyright owner. Further reproduction prohibited without permission.

The size of the corner region has been selected as 5 nm x 5 nm. This area is comparable with the geometric dimensions of the entire grain model, thus the representation of this region with an equivalent finite element increases the computational efficiency. The finite element model and boundary conditions are shown in Figure 6.1. The model is subjected to externally applied compressive strain $\varepsilon_x = 0.002$. The vacancy concentrations on left and on top surfaces are dependent on the stress normal to the grain boundary plane according to Eq. (2.6). We assume that the concentration gradient is small and therefore vacancy fluxes can be neglected at the distance 5δ away from grain boundary, where δ is the GB region thickness. Thus zero fluxes are specified on the right edge of the grain corner model. Although the fluxes on the bottom surface of the grain corner region may be significant, it is not clear how to specify these fluxes when the grain corner region is considered separately from the rest of the grain. In our initial effort to establish the effective creep law, we neglect the fluxes at the bottom surface of the grain corner region and assume that vacancy flow occurs from top surface to lateral internal grain boundary. More accurate representation of vacancy fluxes will be provided later for the model of grain boundary layer.

The application of externally applied strain ε_x is followed by the transient stress relaxation. At each time increment we compute the equivalent stress $\langle \bar{\sigma}(t) \rangle$ and equivalent strain rate $\langle \dot{\bar{\varepsilon}}(t) \rangle$ averaged over the area of the grain corner region. Eliminating the parametric time variable t and plotting average strain rate versus average stress in Figure 6.2, we obtain the piecewise-linear approximation of the creep law.

Reproduced with permission of the copyright owner. Further reproduction prohibited without permission.

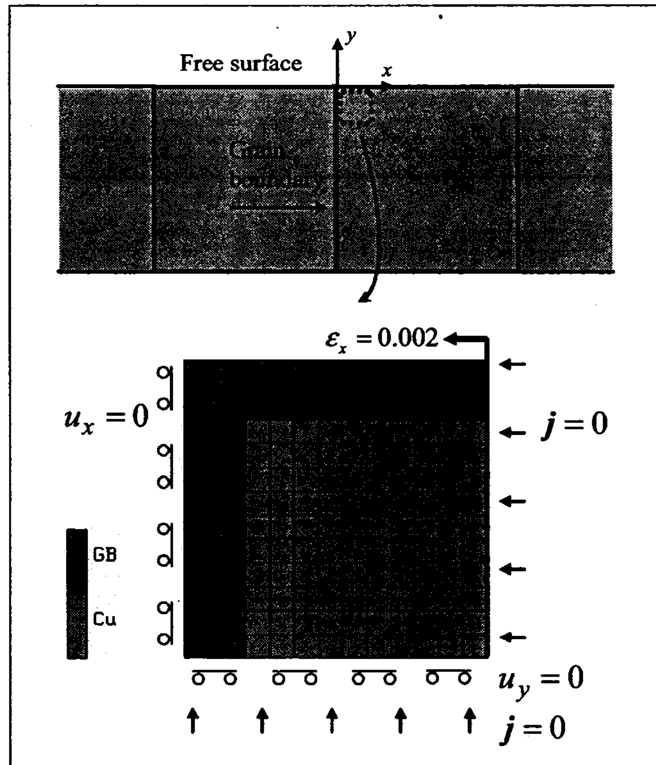

Figure 6.1. Finite element model used to establish effective creep law for grain corner region assuming that stress relaxation occurs due to vacancy fluxes from top surface to internal grain boundary.

The logarithmic plot reveals similar shape of isothermal creep law curves for temperatures in the range 473 K - 1073 K. We found that these curves can be approximated by the power law dependence

$$\frac{\dot{\varepsilon}^{cr} - \dot{\varepsilon}_{\infty}(T)}{A(T)} = (\bar{\sigma} - \bar{\sigma}_{\infty})^n \qquad (6.5)$$

where $A(T)$, $\dot{\varepsilon}_{\infty}(T)$, $\bar{\sigma}_{\infty}$, n are the material parameters that can be determined from the numerical experiments. The physical meaning of fitting parameters $\bar{\sigma}_{\infty}$ and $\dot{\varepsilon}$ could be the average residual stress in the grain after a long period of stress relaxation and the average strain rate corresponding to the residual stress $\bar{\sigma}_{\infty}$. The creep law curves

Reproduced with permission of the copyright owner. Further reproduction prohibited without permission.

computed for the temperature range between 473 K and 1073 K were fitted with Eq. (6.5) as shown by the dashed lines in Figure 6.2. The fitting was performed using fixed values of $n = 0.737$ and $\bar{\sigma}_\infty = 21.8\ MPa$. To obtain these numerical values for n and $\bar{\sigma}_\infty$, we fitted the creep law curve computed for temperature $T = 473$ K and varied all four parameters A, $\dot{\bar{\varepsilon}}_\infty$, $\bar{\sigma}_\infty$ and n in Eq. (6.5). To reproduce the creep law curves computed for temperatures above 473 K, we varied only A and $\dot{\bar{\varepsilon}}_\infty$. The fitted values of these two temperature-dependent parameters are shown in Figure 6.3. Thus the power coefficient n and residual stress $\bar{\sigma}_\infty$ in the approximate expression (6.5) for equivalent creep law were found to be independent from temperature T for grain corner region.

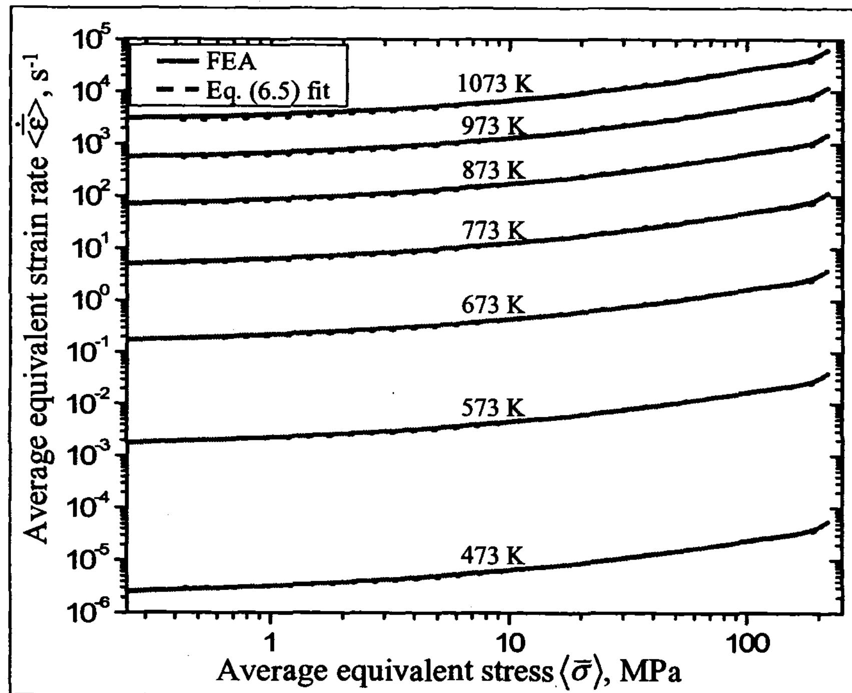

Figure 6.2. FEA predictions of effective creep law for grain corner region in the temperature range from 473K to 1073K. The computed data is fitted with power law equation (6.5).

Reproduced with permission of the copyright owner. Further reproduction prohibited without permission.

As depicted in Figure 6.2, the FEA predictions of creep law can be fitted with Eq. (6.5) except for the portion of the creep law curves that corresponds to initial stage of stress relaxation (the right side of the graph which corresponds to the stress levels $\langle\bar{\sigma}\rangle$>200MPa). We attribute this deviation of FEA predictions from Eq. (6.5) to the effect of idealized application of external strain. As the average equivalent stress in the grain corner model is reduced, the effect of instantaneously applied external load is smoothed out and Eq. (6.5) accurately fits the creep law curves.

The performance of the effective creep law established for the grain corner region is tested by modeling the stress relaxation of Cu grain at temperature T = 673 K. We create the finite element model shown in Figure 6.4a with the creep behavior in the grain corner element specified according to Eq. (6.5).

The adjustable parameters of Eq. (6.5) were found using the coupled FEA analysis of 5nm x 5nm grain corner region at temperature 673 K. The following values were obtained: $n = 0.737$, $\bar{\sigma}_\infty$ = 21.8 MPa, $\dot{\bar{\varepsilon}}_\infty = 0.158\, s^{-1}$ and $A = 1.87 \cdot 10^{-6}$. For simplicity, the material properties for the rest of the model are assumed purely elastic. Note that the explicitly specified diffusional creep law in the model is assumed to reproduce the transient mechanical response to diffusional mass flow. Therefore we consider only mechanical FEA analysis for the model shown in Figure 6.4a. The geometry, boundary conditions and the elastic material properties are as specified in Chapter 4 for the model of one-dimensional linear grain array.

After the application of external strain $\varepsilon_x = 0.002$, stress relaxation occurs due to diffusional creep in the grain corner. The distribution of stress σ_{xx} at time $t = 3 \cdot 10^{-3}$ s is shown in Fig.6.4b. The "benchmark" simulation of chapter 4 shown in Figure 6.4(c)-(d)

Reproduced with permission of the copyright owner. Further reproduction prohibited without permission.

for comparison. We conclude that it is possible to approximate the coupled "benchmark" predictions for the initial stages of stress relaxation with purely mechanical solution obtained using the effective creep law specified in the grain corner. In the following sections we compute the effective creep law in the grain boundary layer and grain interior to model the stress relaxation elsewhere in the grain.

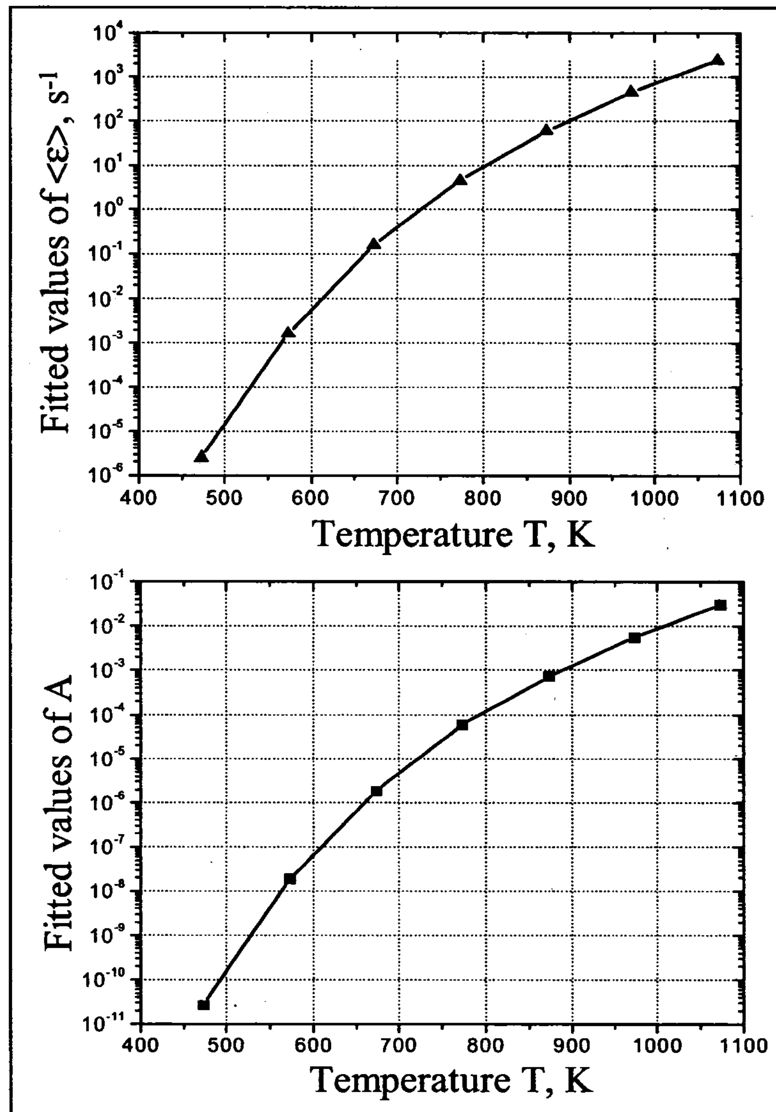

Figure 6.3. Temperature dependence of parameters A and $\dot{\varepsilon}_{\infty}$ obtained by fitting Eq. (6.5) to FEA predictions of creep law curves shown in Figure 6.2.

Reproduced with permission of the copyright owner. Further reproduction prohibited without permission.

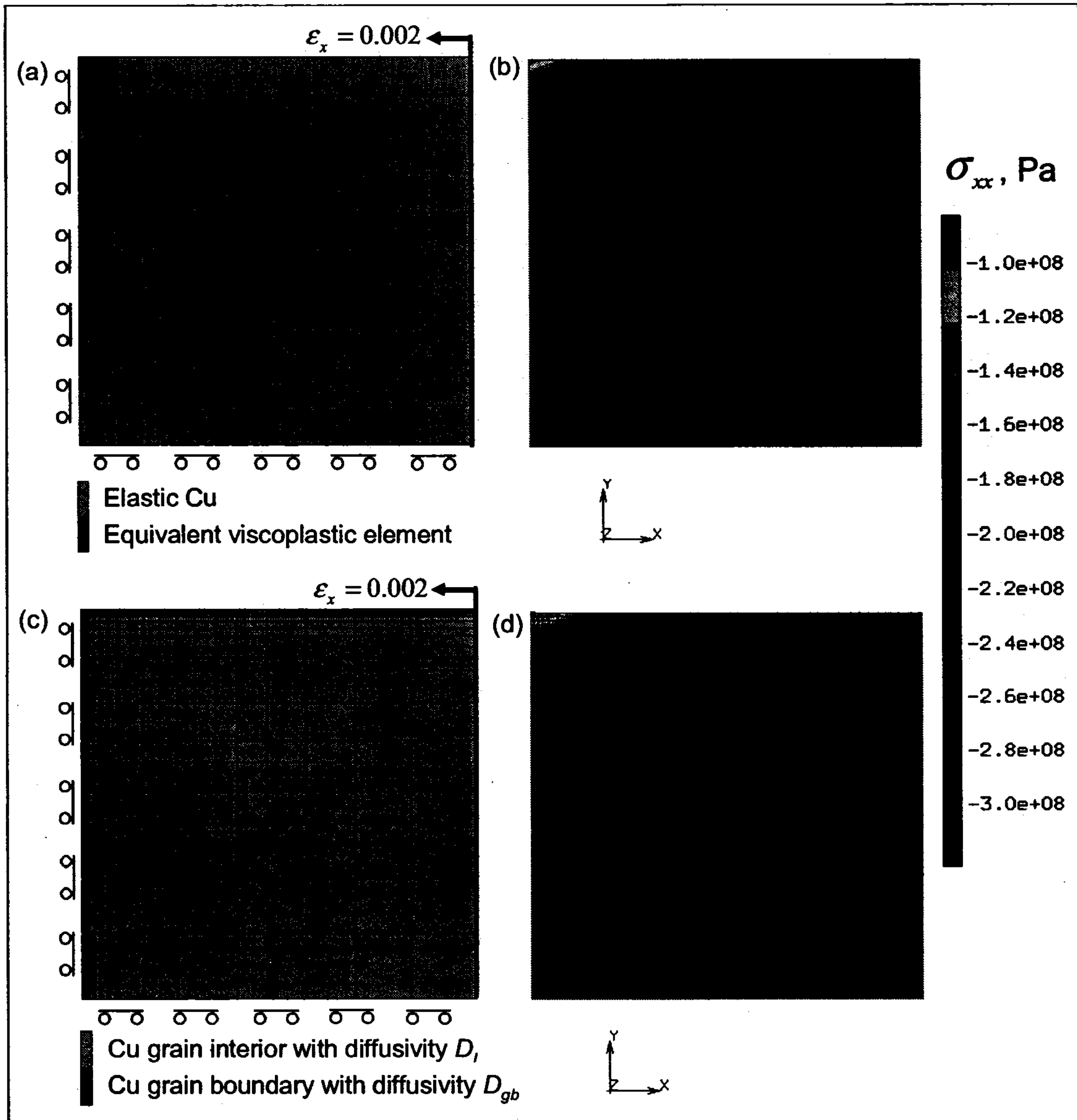

Figure 6.4. Comparison of stress σ_{xx} at time $t = 3.0 \cdot 10^{-3}$ s computed according to (a,b) equivalent viscoplastic element technique and (c,d) coupled FEA formulation.

6.3.2. Stress relaxation numerical experiment for grain boundary layer

In the numerical experiment shown in Figure 6.4, the stress relaxation is restricted only to the top layer of Cu grain. This is due to our assumption of purely elastic material properties outside of grain corner region. To consider the stress relaxation elsewhere in

Reproduced with permission of the copyright owner. Further reproduction prohibited without permission.

the grain, it is necessary to obtain the equivalent diffusional creep law for the regions other than the grain corner. The creep law can be established by modeling the region of interest using the coupled finite element technique with appropriate mechanical and mass flow boundary conditions.

In this section, we compute the creep law for the middle portion of the grain in the vicinity of internal grain boundary. Unlike the grain corner area considered in the previous section, this region does not have the free surface. Therefore, care must be taken to ensure that the mass flow boundary conditions correspond to the appropriate vacancy concentration gradient across the region. For example, it is incorrect to specify zero fluxes at the boundaries of the region as in the previous section, since in this case the stress relaxation does not occur due to the absence of mass flow. The stress relaxation would be possible if nonuniform vacancy concentrations or nonuniform vacancy fluxes are specified along the boundary of the region. It is not immediately clear how to select the adequate distribution of boundary concentrations or vacancy fluxes for the region selected inside the grain. This ambiguity can be avoided by considering the coupled FEA model of the grain boundary layer shown in Figure 6.5.

The width of the layer is selected as 5 nm. This choice is dictated by the following two considerations. First, the size of the region has to be comparable with the geometric dimensions of the entire grain to increase the computational efficiency of the equivalent model as compared to the coupled model with thin GB region that requires the finite elements of bad aspect ratio. Second, the selection of the GB layer width equal to 5δ, where δ is the thickness of the GB region, allows to assume zero vacancy fluxes at the right edge of the GB layer. The mechanical and mass flow boundary conditions for this

Reproduced with permission of the copyright owner. Further reproduction prohibited without permission.

model are specified in the same way as for the grain corner region considered in the previous section.

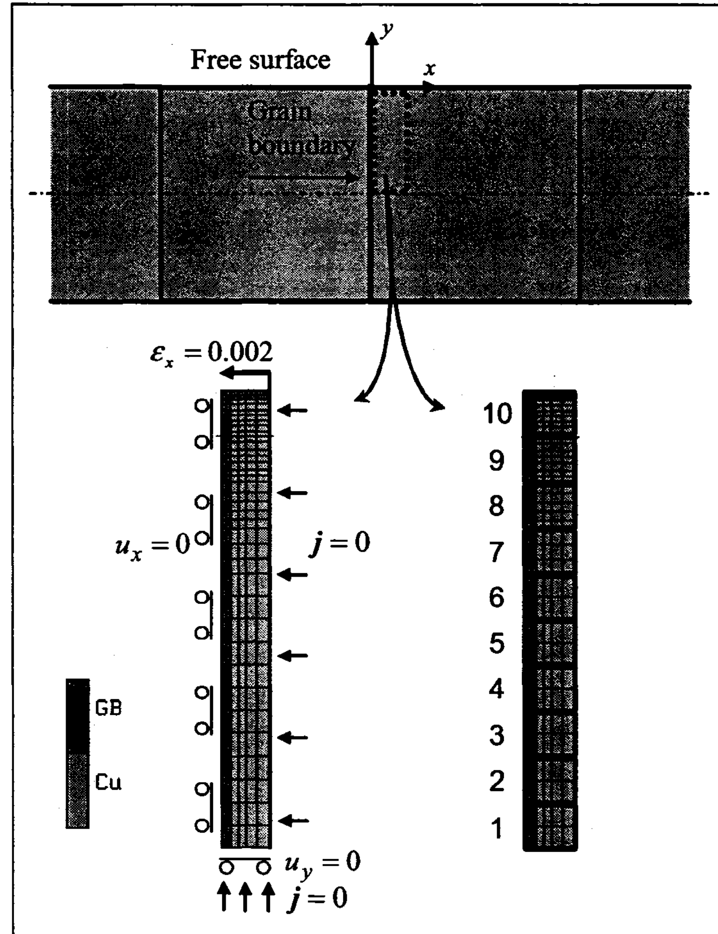

Figure 6.5. Finite element model used to establish effective creep law behavior for GB layer. Equivalent stress and strain rate are averaged over the regions numbered 1 through 10.

We performed the stress relaxation FEA simulation for the GB layer with temperature selected as $T = 673$ K. To ensure stability of time integration, the time step was selected as $1.9 \cdot 10^{-5}$ s. Full stress relaxation in the model was achieved after $8 \cdot 10^{4}$ increments at time $t = 1.52$ s. To complete this simulation for the GB layer model containing 295 nodes and 216 elements, the computation time on Intel Xeon dual core 2.66 GHz, 667 MHz front side bus processor was 4793.28 s. We conclude that the

Reproduced with permission of the copyright owner. Further reproduction prohibited without permission.

coupled elasticity-mass flow simulation for the FEA model of GB layer is computationally affordable compared to the coupled simulation of the entire grain.

The coupled FEA simulation for the internal GB layer allows to establish the effective creep law for this area. To explore whether the creep law varies along the GB layer, we divide the layer into the regions numbered 1 through 10 as shown in Figure 6.5. The equivalent creep strain rate and equivalent stress were averaged separately over each of these areas. To obtain the effective creep law FEA predictions we eliminate the parametric time variable and relate each value of equivalent stress to the corresponding value of equivalent strain rate. Figure 6.6 shows the equivalent creep strain rate plotted vs equivalent stress for each of the regions 1-10. The following remarks can be made regarding the effective creep law for GB layer.

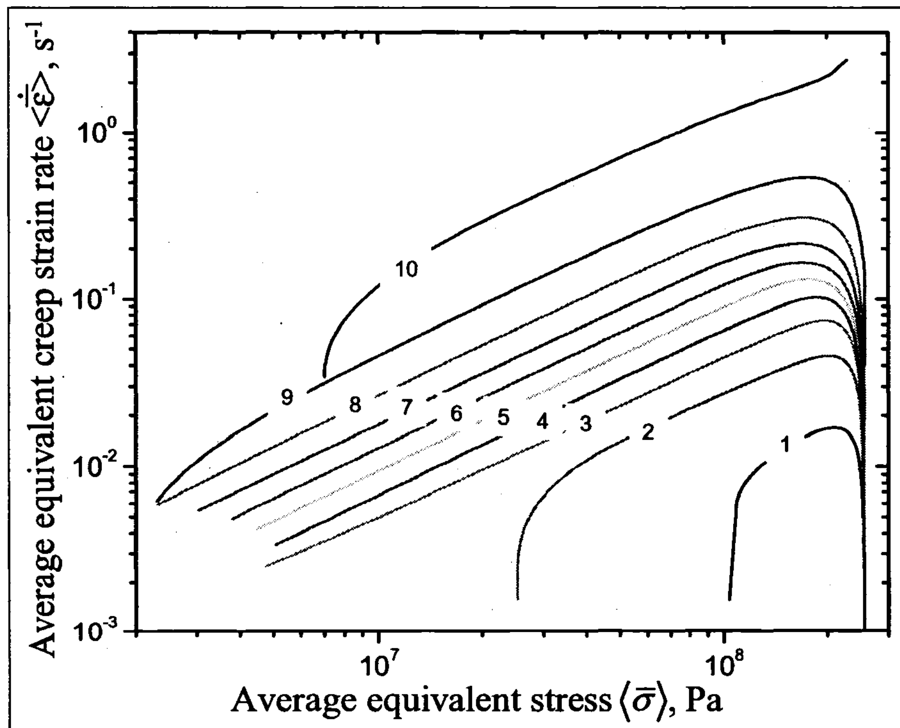

Figure 6.6. FEA predictions of effective creep law for grain boundary layer at temperature 673 K. Creep laws are shown for the regions numbered 1 through 10 in Figure 6.5.

Reproduced with permission of the copyright owner. Further reproduction prohibited without permission.

The creep law is different for each of the considered regions. This may be attributed to the difference in vacancy concentration gradients over the height of GB layer. As shown in Figure 6.7, the vacancy concentration gradient is higher near the free surface compared to the concentration gradient in the middle of internal GB at each time instance throughout the FEA simulation. The vacancy concentration gradient affects the vacancy flux (Eq. 2.7) and thus determines the diffusional creep strain rate (Eq. 2.17). Thus for the same value of equivalent stress $\bar{\sigma}$, the creep strain rate is in the regions close to the free surface than in the middle of the internal grain boundary, as depicted in Figure 6.6.

As shown in Fig. 6.6, the strain rate is close to zero when the equivalent stress $\bar{\sigma}$ is equal to $\bar{\sigma}_0$. This value of equivalent stress corresponds to the uniform distribution of stress $\bar{\sigma}_{xx}$ immediately after the sudden application of external compressive strain. The nearly small value of creep strain rate at $\bar{\sigma} = \bar{\sigma}_0$ may be attributed to negligibly small vacancy concentration gradients everywhere except near the free surface. This is shown in Figure 6.7b for time $t = 0.001$ s which corresponds to the initial stage of stress relaxation. Therefore at $\bar{\sigma} = \bar{\sigma}_0$ the vacancy fluxes arise only near the free surface and creep strains are nonzero only in region 10.

Note that the straight lines on log-log plot in Figure 6.6 indicate that the creep law curves for regions 1 through 10 may be approximated by power law equation similar to Eq. (6.5). Since the slope of the creep law curves is approximately the same, we may conclude that the exponent of power law approximation is not dependent on the location within the GB layer model. We can make another interesting observation if we compare the predictions of the effective creep law for region 10 of GB layer and for the grain

Reproduced with permission of the copyright owner. Further reproduction prohibited without permission.

corner model considered in the previous section. The power law approximation of the equivalent creep laws for both models is approximately the same as shown in Figure 6.8. Therefore, we conclude that it is possible to use the grain corner model to predict the power law exponent which can be used to approximate effective creep law in the entire GB layer.

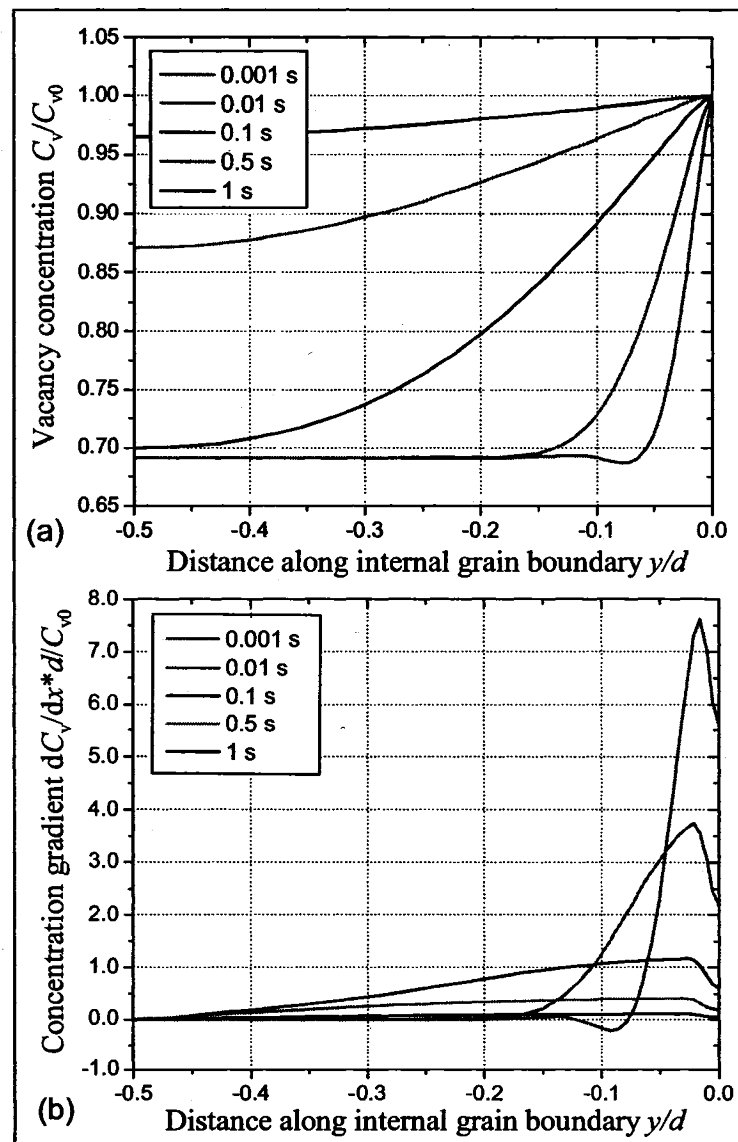

Figure 6.7. Distribution of (a) vacancy concentration and (b) concentration gradient along the internal grain boundary during the transient stress relaxation of GB layer.

Reproduced with permission of the copyright owner. Further reproduction prohibited without permission.

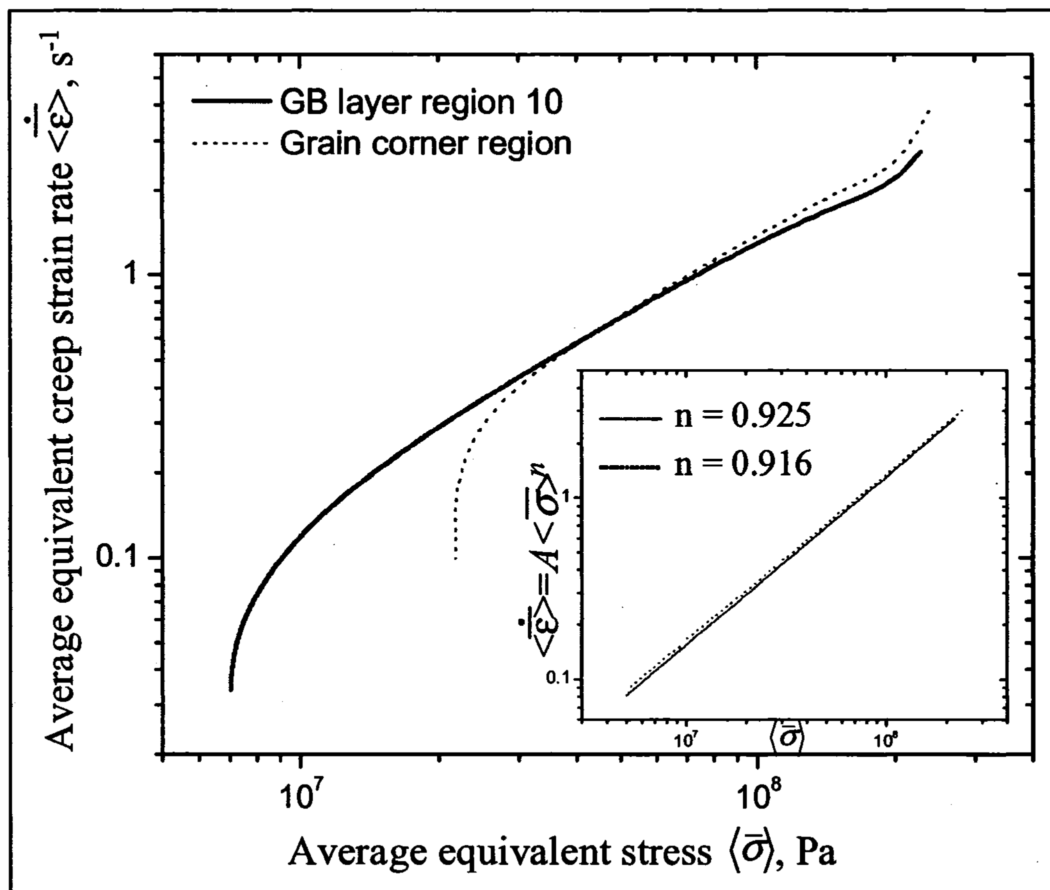

Figure 6.8. Comparison of equivalent creep law predictions for GB layer and grain corner region.

We explore the performance of effective creep law computed for the GB layer by modeling the stress relaxation of Cu grain at temperature T = 673 K. The equivalent FEA model is shown in Figure 6.9a. The creep behavior for each of the GB layer equivalent elements is specified using the piecewise-linear creep law dependence shown in Figure 6.6. Coupled simulations could be performed to establish the effective creep laws for the rest of the Cu grain model. However we expect that the contribution of creep strains in the GB layer is dominant for the stress relaxation in the model shown in Figure 6.9, therefore we assume elastic material properties for the grain interior. The mechanical FEA analysis for the model shown in Figure 6.9a is compared to the coupled FEA

Reproduced with permission of the copyright owner. Further reproduction prohibited without permission.

analysis of "benchmark" model depicted in Figure 6.9b. The geometry, boundary conditions and the elastic material properties are as specified in Chapter 4 for the model of one-dimensional linear grain array.

After the application of external strain $\varepsilon_x = 0.002$, the stress relaxation occurs in the equivalent FEA model of Cu grain due to diffusional creep in the GB layer. The distribution of stress σ_{xx} corresponding to the initial, intermediate and final stages of stress relaxation is shown in Fig.6.10 (a-c) for time instances $t = 0.1$ s, $t = 1$ s and $t = 2.5$ s. The stress field is compared to the "benchmark" simulation of chapter 4 shown in Figure 6.10(d)-(e). It can be seen that the evolution of stress field in the coupled problem can be qualitatively reproduced by the equivalent FEA model with diffusional creep law in the GB layer.

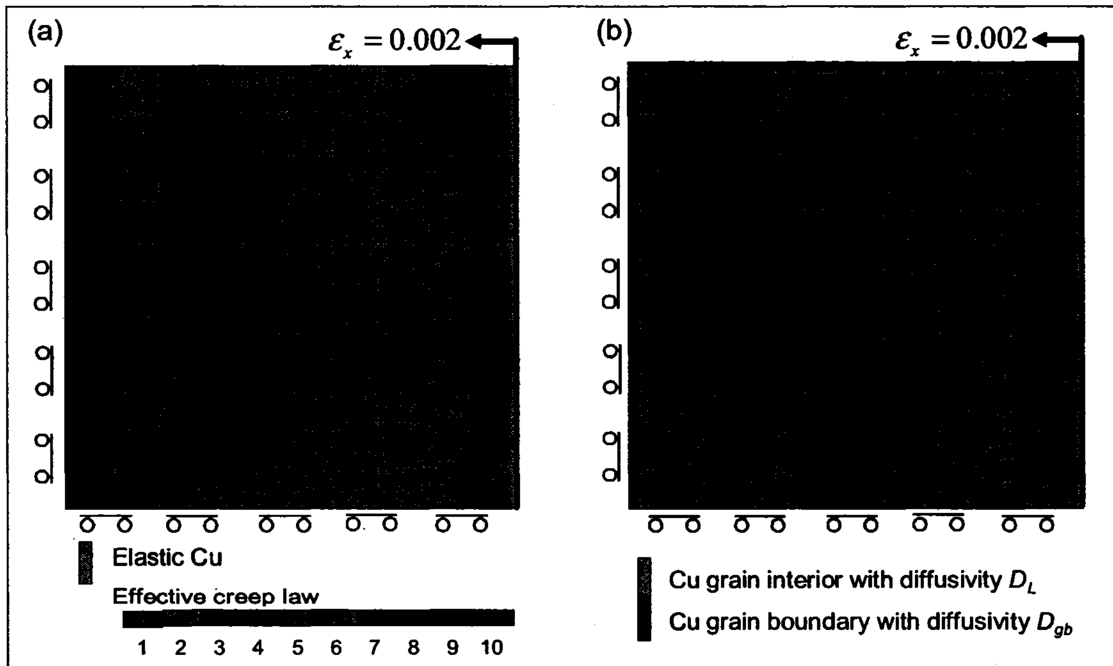

Figure 6.9. (a) Equivalent FEA model of Cu ¼ grain with diffusional creep laws in the GB layer as shown in Figure 6.6 (b) "benchmark" coupled elasticity-mass flow FEA model.

Reproduced with permission of the copyright owner. Further reproduction prohibited without permission.

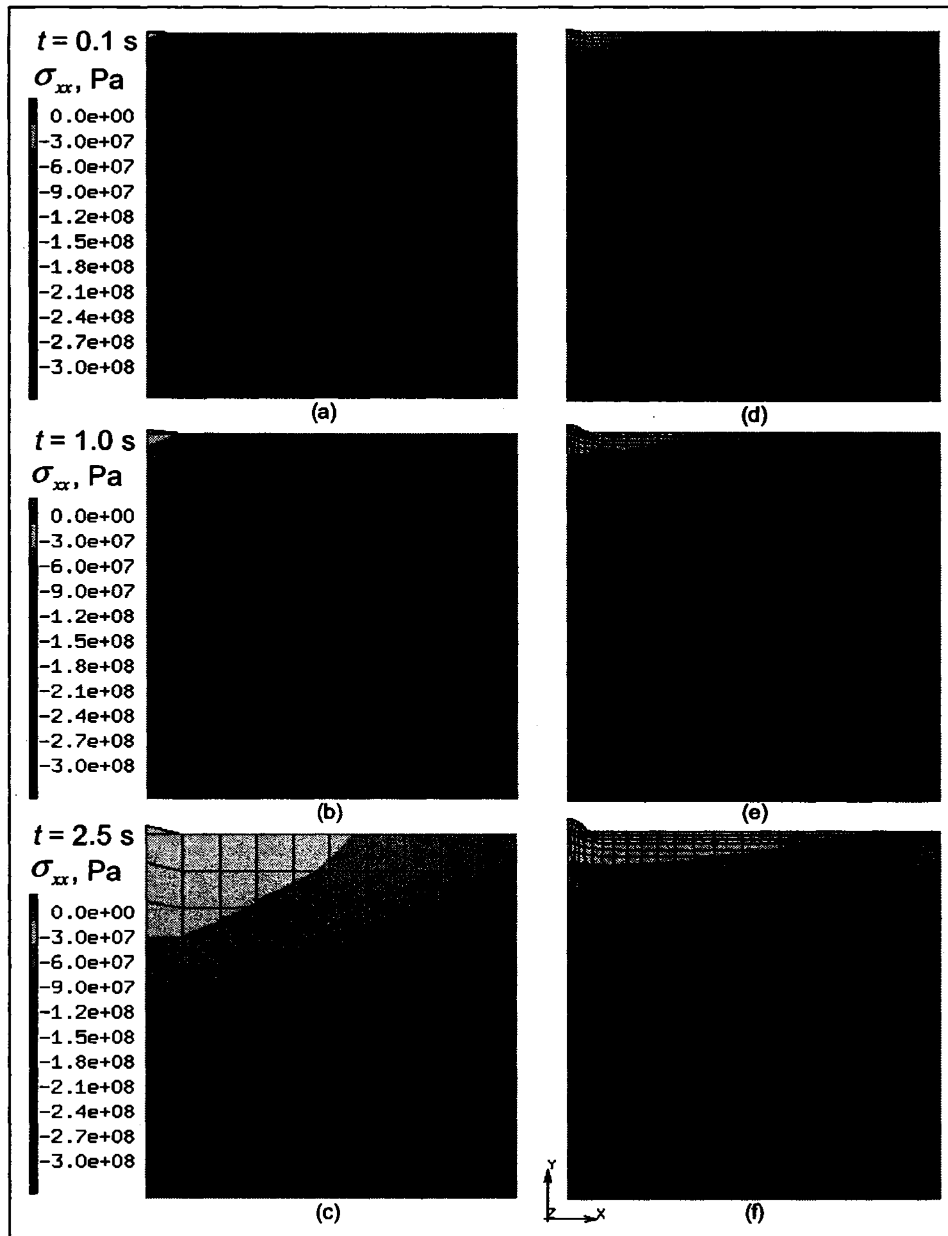

Figure 6.10. Comparison of stress σ_{xx} at the initial, intermediate and final stages of stress relaxation; (a)-(c): equivalent FEA model with effective creep law in GB layer, (d)-(f): "benchmark" coupled elasticity-mass flow FEA model.

The quantitative comparison of stress relaxation predictions is given in Figure 6.11 for the average stress in the model $\langle\sigma_{xx}\rangle$ and in Figure 6.12 for the stress σ_{xx} in the

Reproduced with permission of the copyright owner. Further reproduction prohibited without permission.

top left corner and in the center of the model. The stress evolution computed using the equivalent FEA model follows the predictions of coupled elasticity-mass flow simulation.

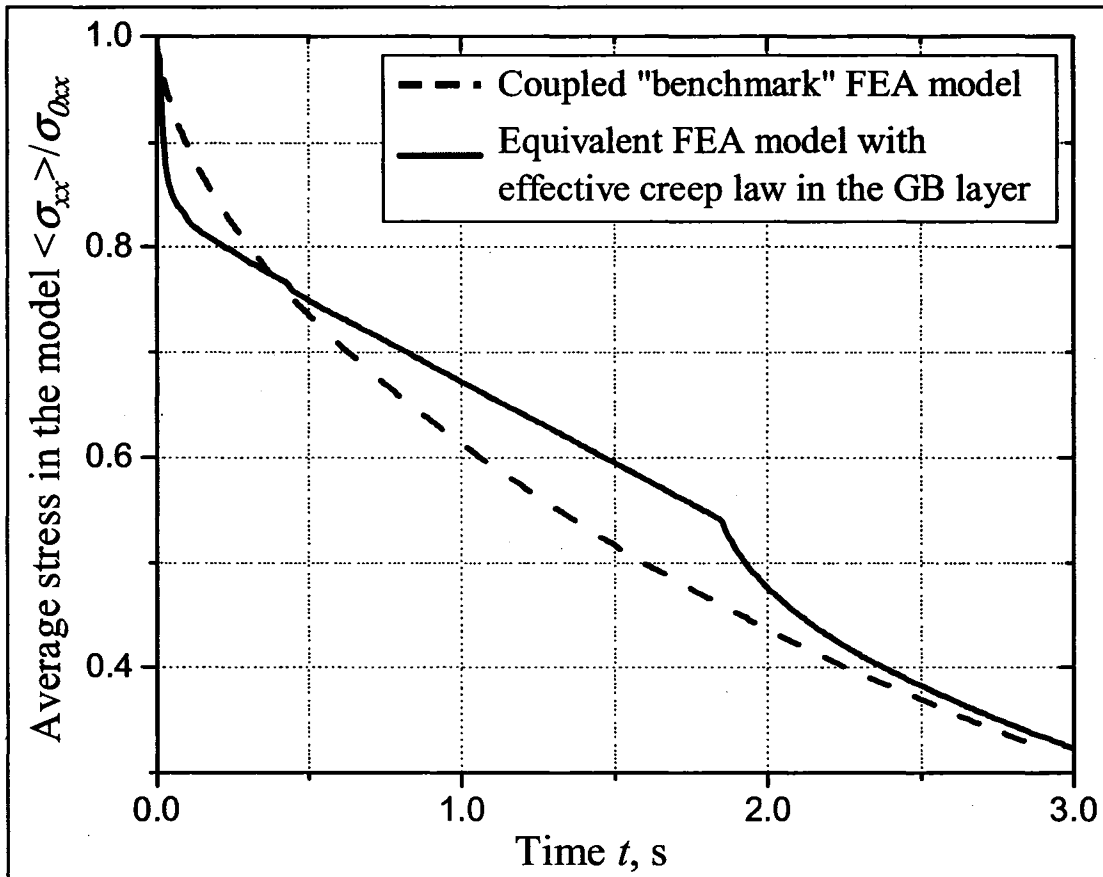

Figure 6.11. Time evolution of average stress in the ¼ grain model. Predictions of equivalent element technique are compared to the "benchmark"coupled FEA simulation.

We note that the stress relaxation curves exhibit jumps in the first derivative with respect to time for the average stress as well as for the stress in the individual nodes. We attribute this behavior to large element size in the equivalent model, as well as to our assumption of purely elastic material properties in the grain interior. As the creep strains are accumulated in the grain boundary layer, the elements in the equivalent FEA model

Reproduced with permission of the copyright owner. Further reproduction prohibited without permission.

experience large shear strain at the interface between elastic grain interior and the GB layer, as shown in Figure 6.13. These rotations, as well as the absence of creep deformations in the grain interior, contribute to the sudden release of stress in the model.

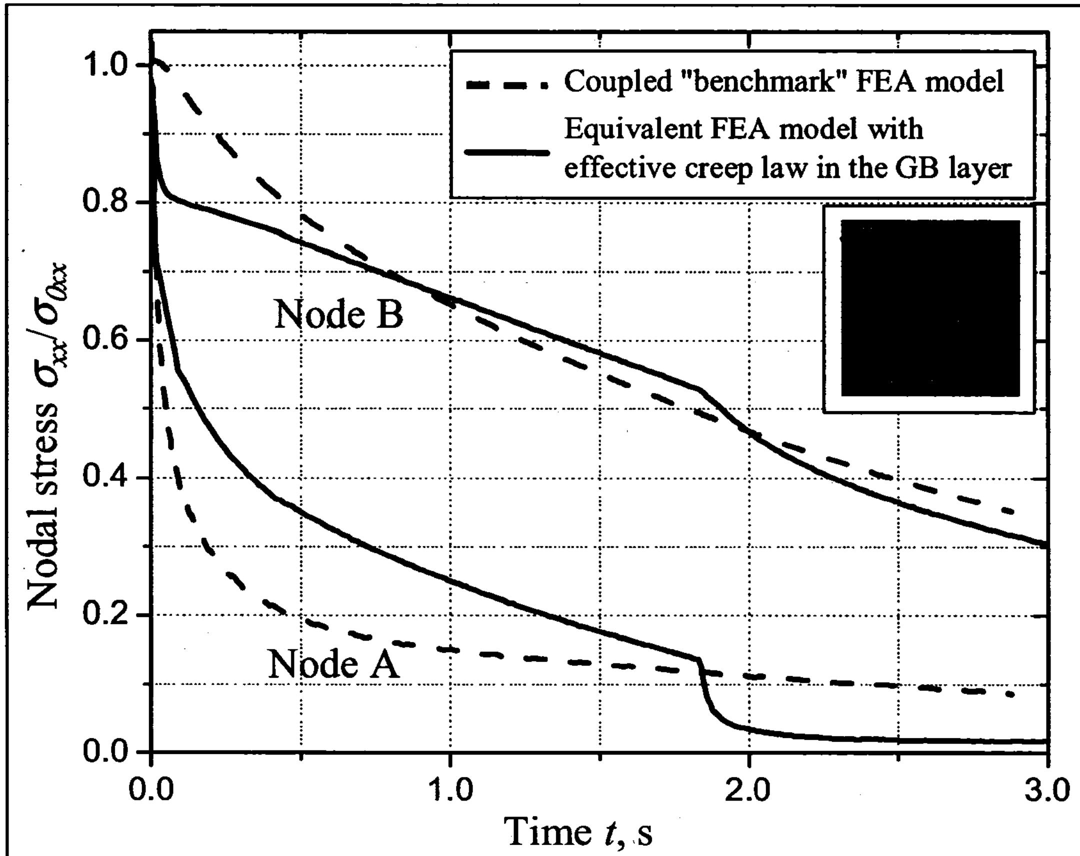

Figure 6.12. Time evolution of nodal stress in the ¼ grain model. Predictions of equivalent element technique are compared to the “benchmark”coupled FEA simulation.

It may be possible to eliminate the jumps in the first time derivative of stress using the following approach. First, the mesh may be refined to model more accurately the accumulation of diffusional creep strain that occurs in the equivalent viscoplastic elements. Second, the creep law may be computed for the grain interior to apply the

Reproduced with permission of the copyright owner. Further reproduction prohibited without permission.

equivalent viscoplastic finite element technique to all the elements in the equivalent FEA model. This approach is considered in the following section.

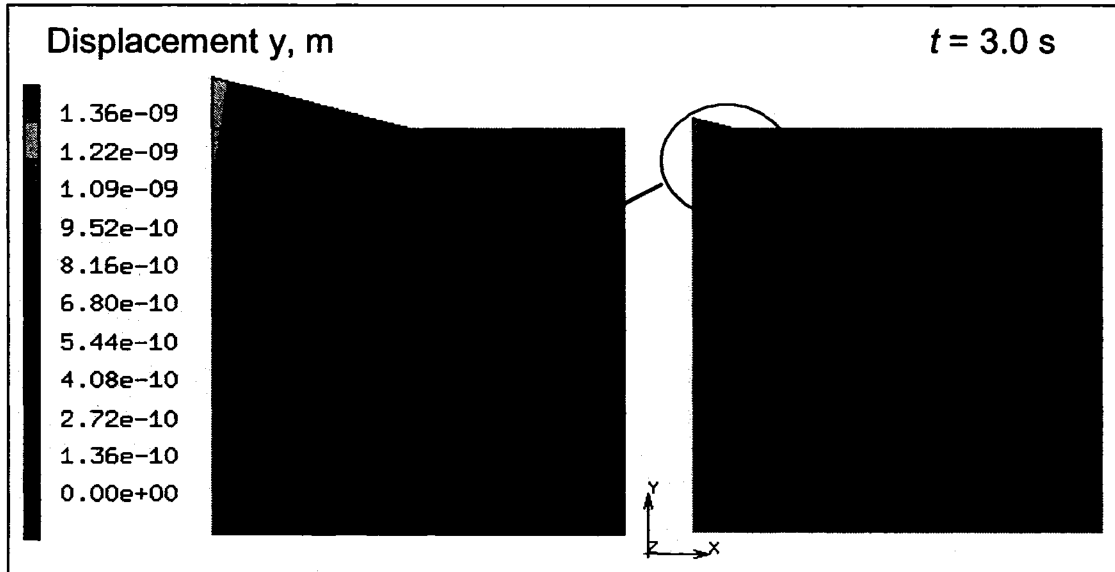

Figure 6.13. Deformed shape and vertical displacements in the equivalent GB layer finite element model at the final stage of stress relaxation.

6.4. Approximation of diffusional creep behavior in the entire Cu grain with four effective creep laws

We have considered the equivalent FEA models of Cu grain to explore the distribution of effective creep laws in the GB region, GB layer and grain interior. The diffusional creep behavior was approximated with equivalent stress vs creep strain rate relations averaged over 10 areas in the GB layer. The predictions of effective creep laws were different for each of the considered regions, which is attributed to the transient non-uniform distribution of concentration gradient throughout the model. Therefore the attempt to reduce the coupled elasticity-mass flow problem to purely mechanical simulation leads to the non-uniform distribution of effective diffusional creep relations in the Cu grain model.

Reproduced with permission of the copyright owner. Further reproduction prohibited without permission.

The application of the established creep laws in the equivalent FEA model approximates the stress relaxation predictions of coupled elasticity-mass flow model. Although the stress relaxation results follow the character of the coupled "benchmark" model predictions, the representation of creep behavior with a distribution of creep relations is not practical. Furthermore, Cu material is assumed uniform throughout the grain interior and GB region, therefore, physically speaking, the concept of diffusional creep law distribution is artificial.

To address these concerns, we need to adjust the proposed FEA technique to represent the distribution of effective creep laws as the averaged material properties assigned to the regions with the most significant difference in the effective diffusional creep behavior. We suggest to distinguish between the grain corners, GB region/layer and grain interior as the areas with the largest variation in the creep laws. The effective creep laws averaged over these areas are established through the numerical experiments described in this section. We consider the following two cases of effective creep law distribution. First, we establish the effective creep law for thin 1nm area in the GB region and 1nm x 1nm grain corners, assuming that the creep behavior for the rest of the grain area may be represented with a single grain interior effective creep law. Second, the effective creep law is established for the GB layer and grain corners which are comparable with the geometric dimensions of the entire grain. We compare the predictions of equivalent FEA models with 4 effective creep laws to the "benchmark" coupled simulation as well as the predictions of the model with the distribution of creep laws found in the previous sections.

Reproduced with permission of the copyright owner. Further reproduction prohibited without permission.

6.4.1. Effective creep laws in Cu grain corners, grain boundary region and grain interior

We model the stress relaxation of Cu grain using the effective diffusional creep material properties in the GB region, grain corners and grain interior as shown in Figure 6.14. To establish the effective creep laws over the GB regions 1-3, we perform the coupled FEA stress relaxation numerical experiment for the GB layer in the manner described earlier in this chapter. Although the coupled stress relaxation problem is solved for the GB layer, the equivalent stress and creep strain rate are averaged only over the GB regions 1-3. The effective creep laws established through this procedure are shown in Figure 6.15.

To obtain the creep law in the grain interior, we employ the following two approaches. (A) We compute two effective creep laws averaged over the GB layer and the rest of the grain interior. These creep laws are shown in Figure 6.16. They are established by performing two coupled simulations for the areas shown in the inset of Figure 6.16. The effective creep law is then obtained through the weighted average over the area of the entire grain interior. (B) The creep law is computed in a coupled simulation for the entire grain interior area. This creep law is shown in Figure 6.17. Note that in the creep law obtained according to the approach (A) the strain rate is approximately 2-3 orders of magnitude larger compared to the corresponding strain rate in creep law obtained through procedure (B).

The stress relaxation predictions for both methods (A) and (B) are shown in Figures 6.18-6.20. Compared to the numerical results of coupled "benchmark" simulation and the equivalent FEA model of section 6.3, the stress relaxation occurs faster for approach (A) and slower for approach (B). Since the only difference between

Reproduced with permission of the copyright owner. Further reproduction prohibited without permission.

these two approaches is the selection of the creep law assigned to the grain interior, we conclude that additional investigation is necessary to provide the adequate approximation for the grain interior effective creep law. Figures 6.18-6.20 show that it may be possible to reproduce the stress relaxation behavior of the "benchmark" problem with the equivalent model shown in Figure 6.14, but it is not clear how to obtain average creep law for the grain interior with large variation in effective creep behavior.

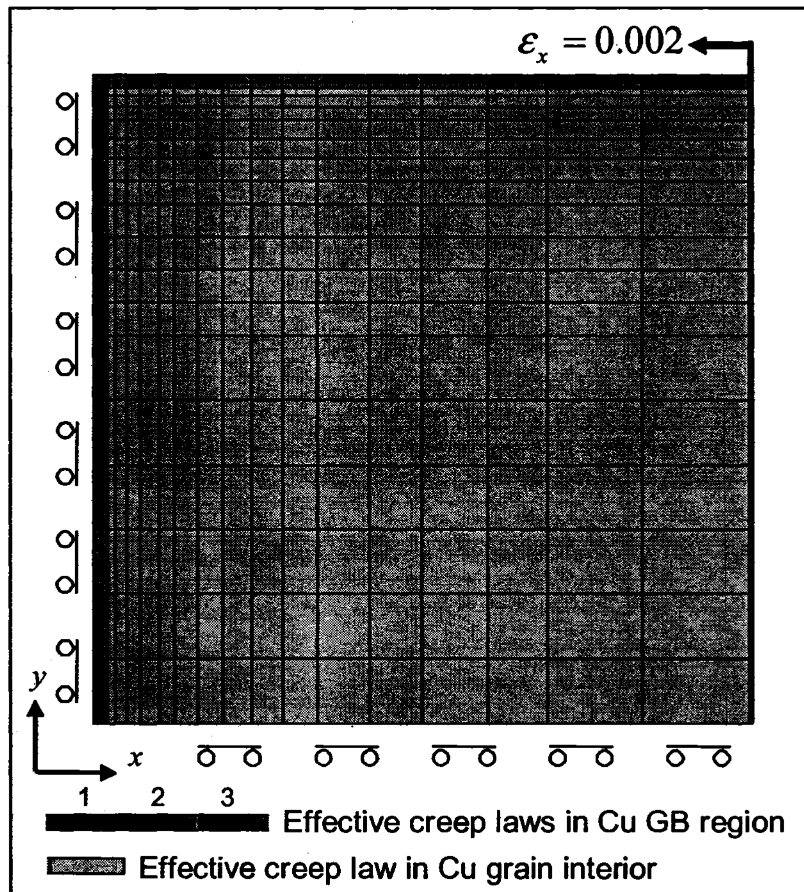

Figure 6.14. Equivalent FEA model of Cu grain with four effective diffusional creep laws and 1nm GB region.

Reproduced with permission of the copyright owner. Further reproduction prohibited without permission.

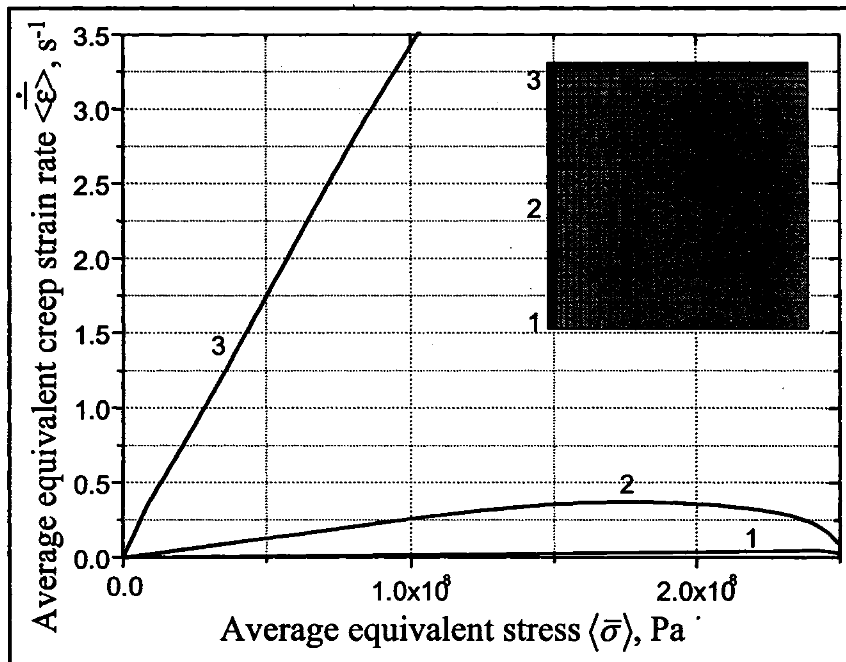

Figure 6.15. FEA predictions of effective creep laws in the grain corners and the rest of 1nm GB region at temperature 673 K.

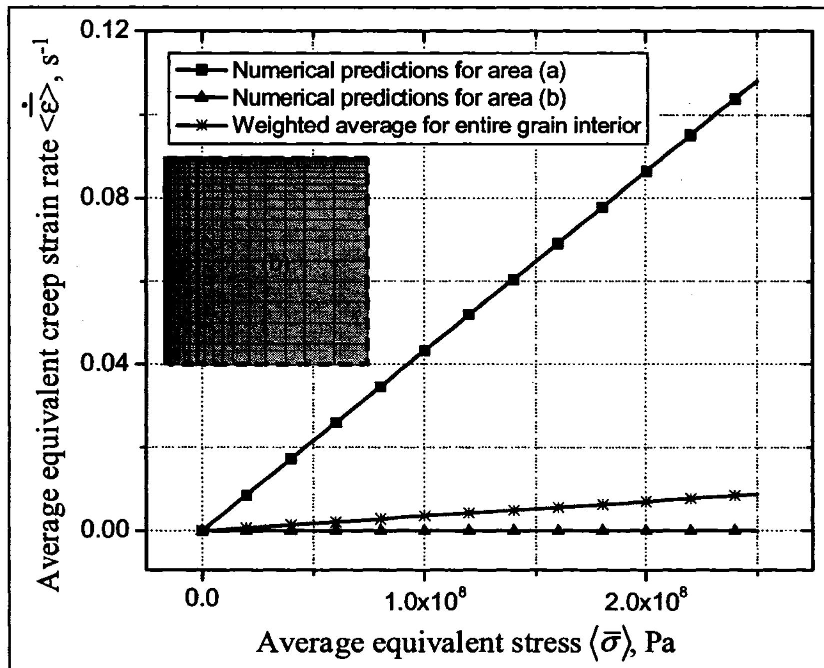

Figure 6.16. Approximation of creep behavior in the grain interior with a single effective creep law averaged over the areas of GB layer and the rest of the grain interior.

Reproduced with permission of the copyright owner. Further reproduction prohibited without permission.

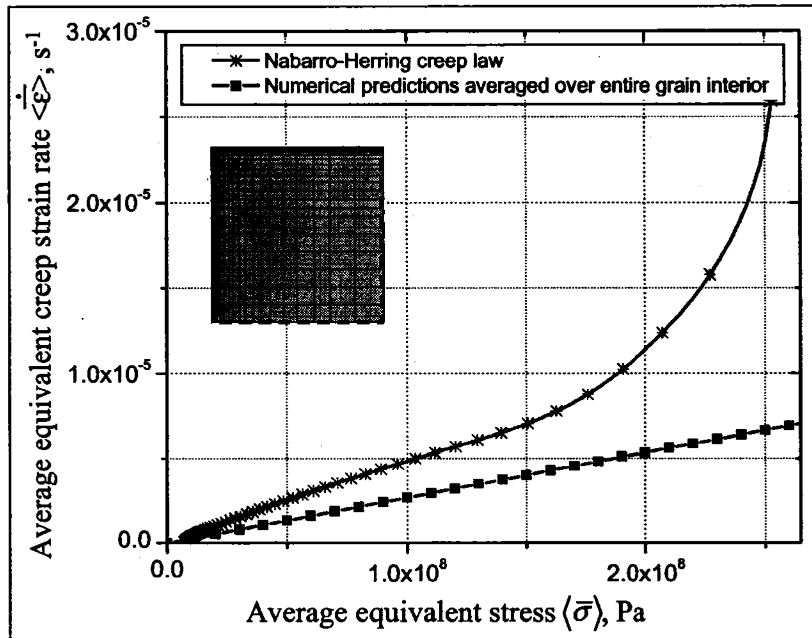

Figure 6.17. Approximation of creep behavior in the grain interior with a single effective creep law averaged over the entire area of the grain interior.

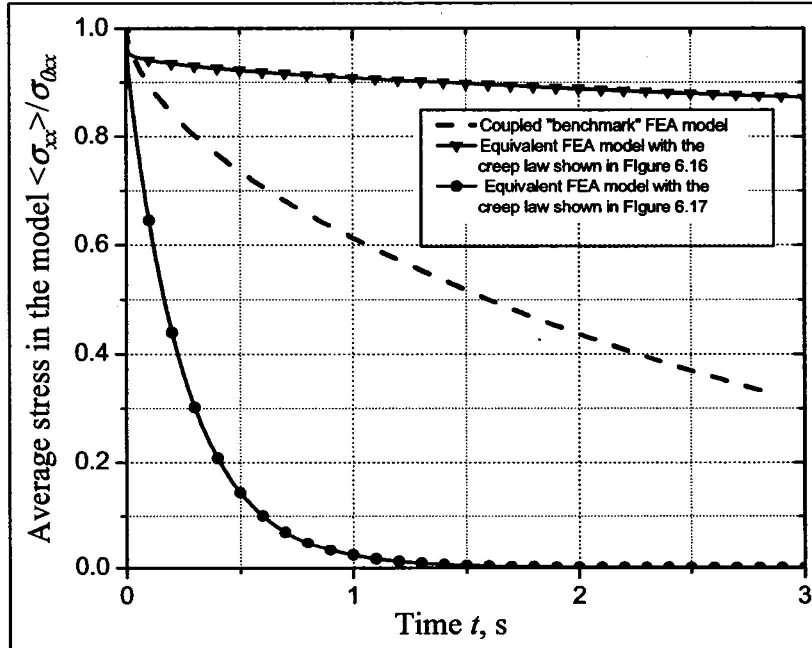

Figure 6.18. Time evolution of average stress in the equivalent model of Cu grain with the creep behavior approximated by four creep laws in the GB region and the grain interior.

Reproduced with permission of the copyright owner. Further reproduction prohibited without permission.

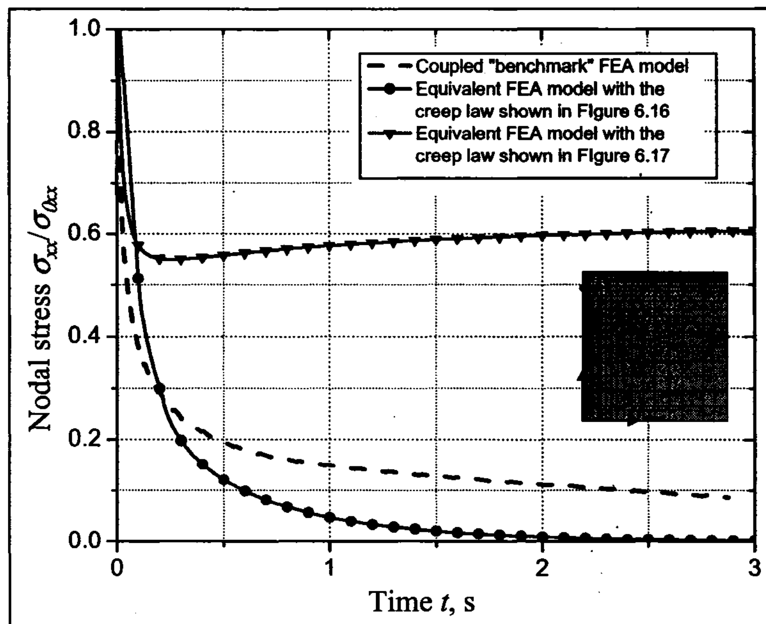

Figure 6.19. Predictions of time evolution of stress σ_{xx} in the grain corner node A for the equivalent FEA model with four creep laws in the GB region and the grain interior.

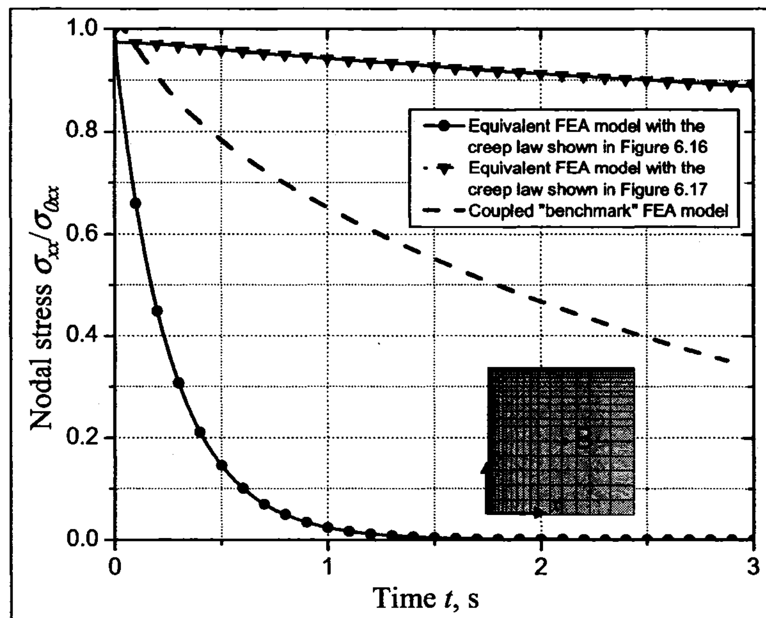

Figure 6.20. Predictions of time evolution of stress σ_{xx} in the grain center node B for the equivalent FEA model with four creep laws in the GB region and the grain interior.

Reproduced with permission of the copyright owner. Further reproduction prohibited without permission.

We believe that the consideration of GB layer rather than GB region would provide the adequate representation of effective creep law averaged over the grain interior since the areas with high creep strain rate in the vicinity of GB region will be incorporated into the GB layer. The following section considers the equivalent FEA model with four effective creep laws averaged over the GB layer, grain corners and the grain interior.

6.4.2. Effective creep laws in Cu grain corners, grain boundary layer and grain interior

In this section, the stress relaxation of Cu grain is modeled using the effective diffusional creep material properties in the GB layer, grain corners and grain interior as shown in Figure 6.21. To establish the effective creep laws for these areas, we perform the coupled FEA stress relaxation numerical experiment for the GB layer and grain interior in the manner described in Section 6.3.2. Figure 6.22 shows the effective creep laws obtained for the GB layer and grain interior and averaged over the areas shown in Figure 6.21. The predictions of the equivalent model for the stress relaxation of the entire grain are shown in Figures 6.23-6.25. The results are compared to the numerical predictions of coupled "benchmark" simulation and the equivalent FEA model of section 4.1.

We observe that the introduction of the material properties averaged only in 4 regions results in the stress relaxation curves which are smooth compared to the predictions obtained in Section 6.2.3 for the model with the distribution of 10 different creep laws over the GB layer. However the prediction of the average stress is not as close

Reproduced with permission of the copyright owner. Further reproduction prohibited without permission.

to the result of the benchmark simulation at the end of the stress relaxation as in the case of 10 different GB layer creep law material properties.

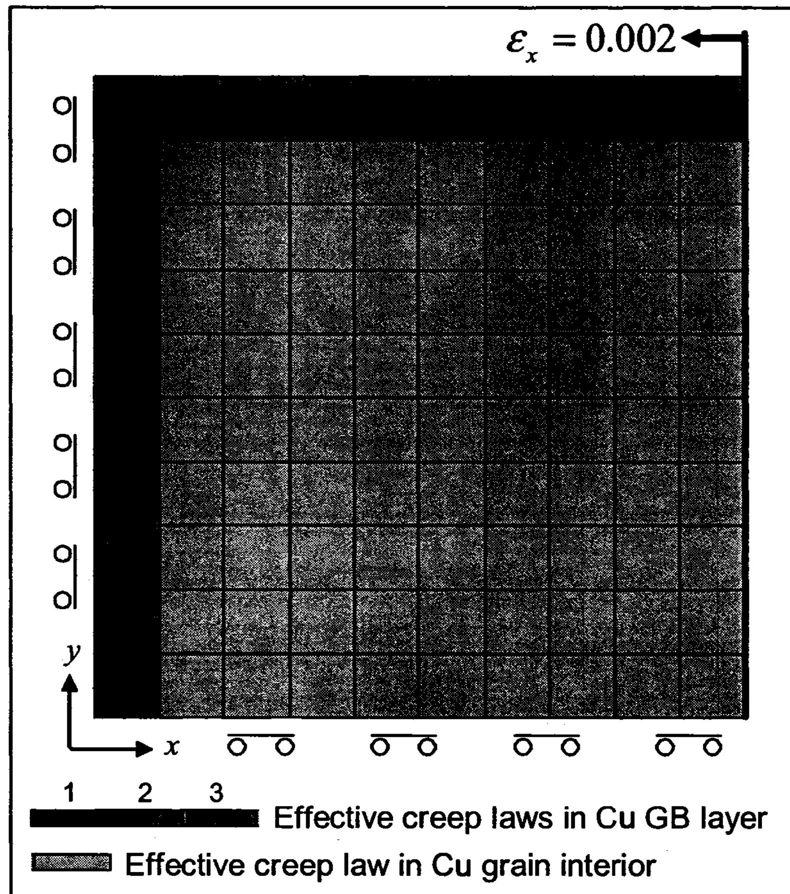

Figure 6.21. Equivalent FEA model of Cu grain with coarse mesh, 5nm GB layer and four effective diffusional creep laws.

We also explore whether the model with refined mesh shown in Figure 6.26 allows to obtain better correspondence with the benchmark problem for the same distribution of effective material properties. The results of equivalent FEA simulation for this model are shown in Figures 6.27-6.29. In addition, we considered the stress relaxation of the model with linearly approximated creep laws shown by the dashed lines in Figure 6.22. This approximation neglects the effect of sudden application of the

Reproduced with permission of the copyright owner. Further reproduction prohibited without permission.

external load. The model predicts the slower stress relaxation compared to the results of the benchmark simulation, while the simplified creep laws result in faster stress relaxation. The numerical predictions follow the results of the benchmark model and the curves are smooth compared to the coarse mesh.

Although was not possible to represent accurately the results of coupled "benchmark" simulation, we found that the prediction of the average stress at the end of the stress relaxation falls within 10% difference for the model with four effective creep laws averaged over the GB layer, grain corners and the grain interior.

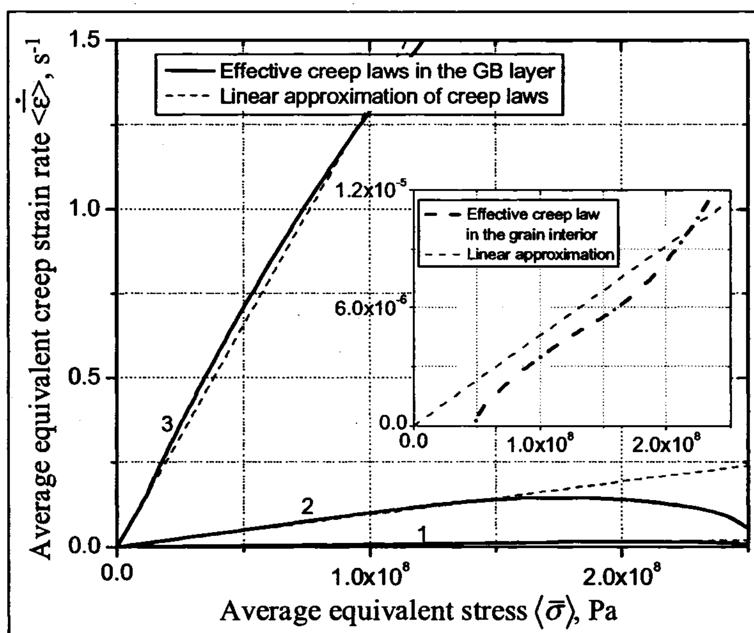

Figure 6.22. FEA predictions of four effective creep laws in the grain corners, 5nm GB layer and grain interior at temperature 673 K.

Reproduced with permission of the copyright owner. Further reproduction prohibited without permission.

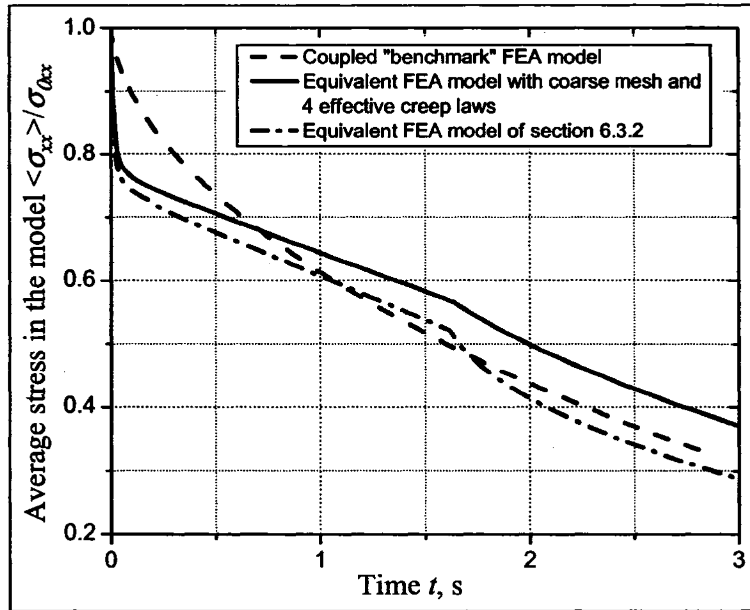

Figure 6.23. Average stress in the equivalent Cu grain model with coarse mesh and the creep behavior approximated by four creep laws in the GB layer and the grain interior.

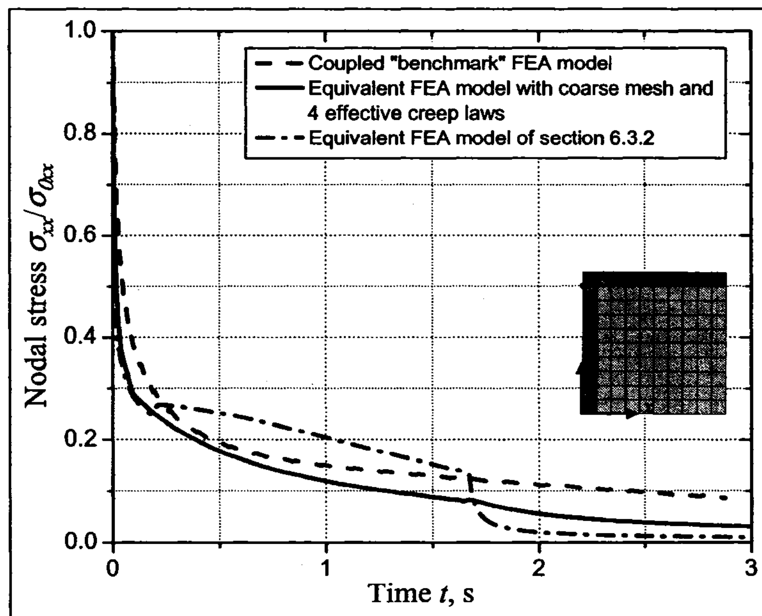

Figure 6.24. Stress σ_{xx} in the grain corner node A predicted by the equivalent FEA model with coarse mesh and four creep laws in the GB layer and the grain interior.

Reproduced with permission of the copyright owner. Further reproduction prohibited without permission.

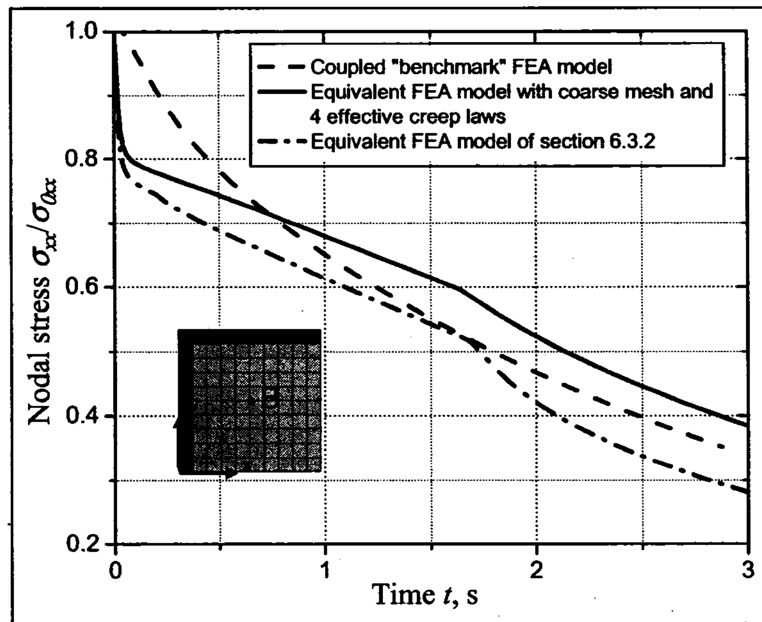

Figure 6.25. Stress σ_{xx} in the grain center node B predicted by the equivalent FEA model with coarse mesh and four creep laws in the GB layer and the grain interior.

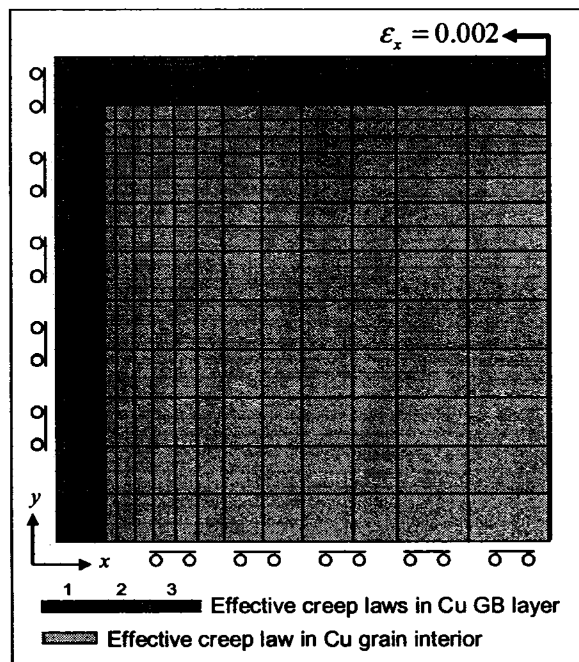

Figure 6.26. Equivalent FEA model of Cu grain with refined mesh, 5nm GB layer and four effective diffusional creep laws.

Reproduced with permission of the copyright owner. Further reproduction prohibited without permission.

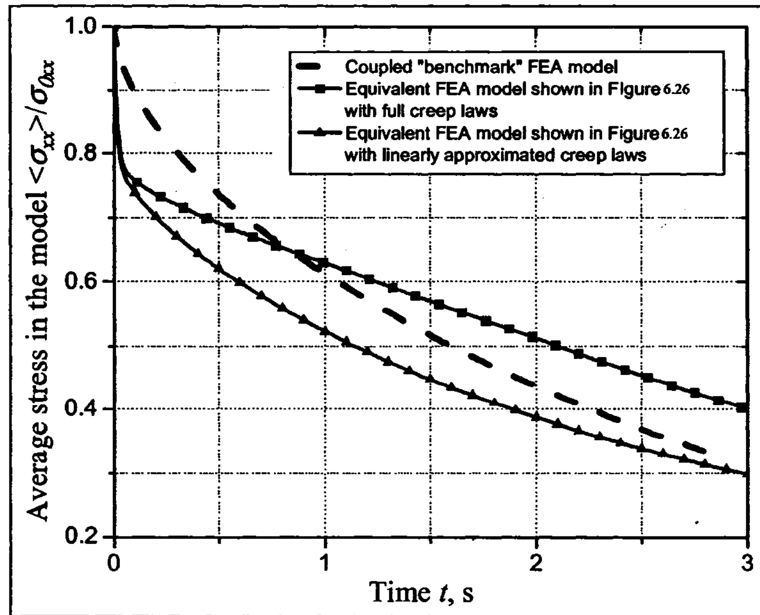

Figure 6.27. Average stress in the equivalent Cu grain model with refined mesh and the creep behavior approximated by four creep laws in the GB layer and the grain interior.

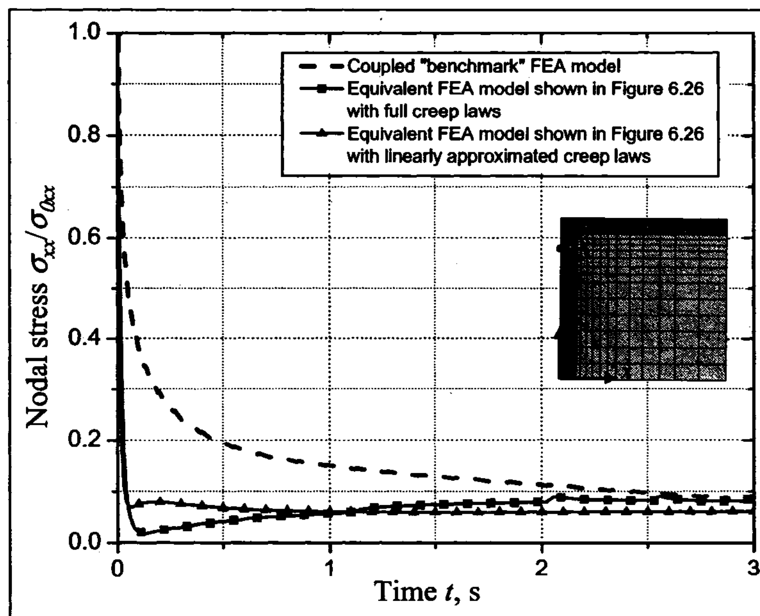

Figure 6.28. Stress σ_{xx} in the grain corner node A predicted by the equivalent FEA model with refined mesh and four creep laws in the GB layer and the grain interior.

Reproduced with permission of the copyright owner. Further reproduction prohibited without permission.

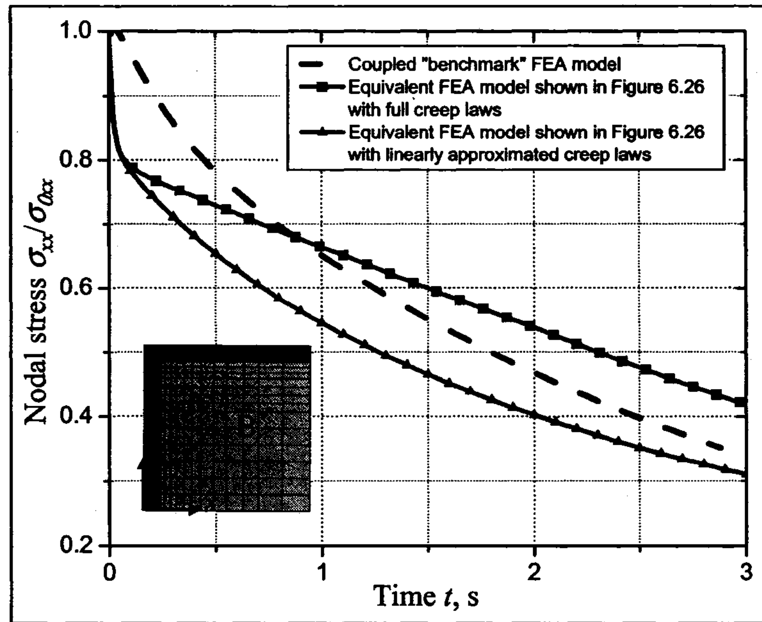

Figure 6.29. Stress σ_{xx} in the grain center node B predicted by the equivalent FEA model with refined mesh and four creep laws in the GB layer and the grain interior.

Reproduced with permission of the copyright owner. Further reproduction prohibited without permission.

CHAPTER 7

CONCLUSION

The diffusional creep due to stress-induced vacancy flow constitutes one of the major deformation mechanisms in Cu-damascene interconnects during thermal processing of integrated circuit devices. The phenomenon of diffusional creep and stress relaxation in polycrystalline metals can be modeled with the finite element technique that accounts for the enhanced vacancy diffusivity in the grain boundary region of finite thickness. The model introduced in this thesis is multiscale because the thickness of grain boundary region (~1 nm for Cu) is at least an order of magnitude smaller than the analyzed domain of one or more grains. The formulation couples the elasticity and vacancy concentration problems through diffusive creep strains. Transient solution is obtained using the iterative procedure with stress-dependent equilibrium vacancy concentration updated at each time step.

The numerical procedure has been implemented into a commercial finite element program MSC.Marc and validated by comparing its numerical predictions with analytical models and results of other authors obtained by different techniques. We used the stress relaxation of linear grain array model with grains of idealized square shape as the "benchmark" problem. The numerical results for evolution of normal stress distribution along the internal grain boundary are in good correspondence with the predictions existing in the literature. The numerically computed estimate of relaxation time is within

Reproduced with permission of the copyright owner. Further reproduction prohibited without permission.

30% correspondence to the estimate obtained using Nabarro-Herring and Coble theories. This suggests that the model presented in this thesis may be used to predict diffusive stress relaxation in more advanced systems of practical importance, such as Cu interconnects at elevated temperatures. We also considered the example of diffusional creep in 3x3 grain assembly subjected to the externally applied tractions. We found that the FEA results for smaller grain size (<100 nm) are in good agreement with the theoretical creep predictions. The study of the creep rate dependence on the choice of grain boundary region thickness suggests that the predictions of the diffusional creep strain rate are sensitive to the selection of the GB region thickness. Therefore the thickness of enhanced diffusivity region may be used as a parameter to calibrate the model and account for the interface characteristics such as impurities and deposition conditions.

We applied the coupled elasticity-mass flow FEA technique to predict the stress relaxation of typical uncapped Cu interconnect structures. The stress relaxation predictions as well as the material buildup in the grain boundary-free surface junction are experimentally verifiable using, for example, the wafer curvature measurement to investigate the stress relaxation and AFM image subtraction technique for nanoscale deformation measurement.

We used the first order mesh refinement multipoint constraints to coarsen the mesh in the grain bulk and mitigate the computational challenge while preserving the implementation of the model in the commercial FEA package. Further enhancement of the efficiency for diffusional creep modeling technique was done by the development of the equivalent viscoplastic finite element approach. The computational efficiency was

Reproduced with permission of the copyright owner. Further reproduction prohibited without permission.

significantly improved by the reduction of the coupled diffusional creep formulation to equivalent purely mechanical creep analysis. We explored the behavior of the numerically obtained equivalent creep laws in different areas of Cu grain. We found that due to the non-uniform distribution of vacancy concentration gradient in the model of the grain, the creep law distribution is highly nonuniform. However we obtained good correspondence to the coupled "benchmark" problem for the equivalent viscoplastic element model containing only four averaged equivalent creep laws computed for GB layer, grain corners and the rest of the grain interior. The difference for average stress relaxation predictions after the period that corresponds to the relaxation time τ is within 10% of initial value of stress in the model.

The equivalent finite element technique was developed in an effort to improve the computational efficiency of the FEA approach introduced in this thesis. Based on the numerical predictions for the test problems considered in the previous Section, we believe that this technique is capable of reducing the computation time while keeping reasonable accuracy of the numerical predictions. The enhancement of the computational capability allows to extend the work presented in this thesis to consider several possible future directions.

First, the equivalent viscoplastic finite element technique could be developed further. The directions of this development may include the exploration of the possibility to represent the diffusion creep behavior of an entire grain by some approximation of the creep law for arbitrary grain geometry and external loading.

Next, it may be of significant interest to consider the contribution of other important nanoscale deformation mechanisms to inelastic deformation, in addition to the

Reproduced with permission of the copyright owner. Further reproduction prohibited without permission.

diffusion-based mass flow mechanism studied in this dissertation. These mechanisms include the diffusion-assisted GB sliding and dislocation motion.

In addition to the stress-relaxation and creep, the phenomena of modeling and experimental interest include the void growth and hillock formation. The numerical predictions of the model which accounts for the combination of deformation mechanisms may become a subject for experimental verification. We strongly believe in the importance of experimental investigations, while recognizing all the technical, logistical and financial challenges involved in the organization, management and execution of nanoscale deformation measurements.

Another important direction of future work is motivated by the new developments and design solutions in the interconnect manufacturing. Because of the fast pace of progress in microelectronics industry, the selection of objects for modeling and experimental investigation needs to be constantly revised to maintain the practical significance of the research. For example, the emerging technology of air-gap interconnects may become a considerable interest of research to understand the nanoscale deformation in these structures. This may require the extension of the model presented in this dissertation to consider the three dimensional geometry of free-standing lines and vias.

Finally, the technique may be applied to study the parameter sensitivity for various interconnect structures of possible interest. Some of the design parameters that may affect the stress relaxation include the selection of the dielectric material, passivation layer material and interconnect line thickness. The predictions of stress relaxation may also depend on the internal parameters of the model such as the grain boundary region

Reproduced with permission of the copyright owner. Further reproduction prohibited without permission.

thickness and activation energy of vacancy motion. In addition, stress relaxation may be affected by anisotropy and orientation of Cu grains, grain boundary surface roughness and other parameters of interconnect line microstructure.

A remark should be made about the aforementioned directions of future work, considering that the research presented in this dissertation is motivated by the industry needs for the reliability of interconnect structures. The directions mentioned above represent only a tentative outlook on the possible future of this research. As the technology evolves to continue the minituarization of on-chip microelectronic systems, new topics may emerge and the suggested future directions may be revised to become more relevant and applicable.

Reproduced with permission of the copyright owner. Further reproduction prohibited without permission.

LIST OF REFERENCES

1. Rathore H.S. and Chanda K., in *Semiconductor Manufacturing Handbook*, H. Geng, Editor, pp. 4.1-4.13, McGraw-Hill (2005).

2. Sullivan T.D., *AIP Conf. Proc.* (491) pp. 39-50 (1999).

3. Kamsah N., Gross T.S., Tsukrov I.I., *Trans. ASME* **124** pp. 12-21 (2002).

4. Kobrinsky M.J., Thompson C.V., Gross M.E., *J. Appl. Phys.* **89**(1) pp. 91-8 (2001).

5. Gross T.S., bin Kamsah N., Tsukrov I.I., *J. Mater. Res.* **16**(12) pp. 3560-3566 (2001).

6. Li B., Sullivan T.D., Lee T.C., Badami D., *Microelectronics reliability* **44**(3) pp. 365-80 (2004).

7. Hussein M.A. and He J., *IEEE trans. semicond. manufact.* **18**(1) pp. 69-85 (2005).

8. Nabarro F.R.N., in *Report of a conference on strength of solids*, pp. 75-90, The Physical Society, London (1948).

9. Herring C., *J.Appl.Phys.* **21** pp. 437-445 (1950).

10. Coble R.L., *J.Appl.Phys.* **34**(6) pp. 1679-1682 (1963).

11. Ruano O.A., Wadsworth J., Wolfenstine J., Sherby O.D., *Mater. Sci. Eng. A* **A165**(2) pp. 133-141 (1993).

12. Ruano O.A., Sherby O.D., Wadsworth J., Wolfenstine J., *Mater. Sci. Eng. A* **A211**(1-2) pp. 66-71 (1996).

13. McNee, Scripta *Mater.* **47** pp. 619-623 (2002).

14. Kong Q.P., Cai B., Lu L., Lu K., *Diffusion and Defect Data* **188-190** pp. 45-58 (2001).

15. Langdon T.G., *Metal. Mater. Trans. A* **33**(2) pp. 249-259 (2002).

16. Ovid'ko I.A., *International Materials Reviews* **50**(2) pp. 65-82 (2005).

17. Gao H., Zhang L., Nix W.D., Thompson C.V., Arzt E., *Acta Mater.* **47**(10) pp. 2865-78 (1999).

Reproduced with permission of the copyright owner. Further reproduction prohibited without permission.

18. Weiss D., Gao H., Arzt E., *MRS Symp. Proc.* **673** pp. 1-2 (2001).

19. Buehler M.J., Hartmaier A., Gao H., *MRS Symp. Proc.* **821** pp. 221-32 (2004).

20. Raj R. and Ashby M., *Metall. Trans.* **2** pp. 1113-1127 (1971).

21. Gosz M. and Okyar A.F., *Mech.Mater.* **31** pp. 317-329 (1999).

22. Okyar A.F. and Gosz M., *Finite Element in Analysis and Design* **37** pp. 961-977 (2001).

23. Kim B.-N., Hiraga K., Morita K., *Acta Mater.* **53**(6) pp. 1791-1798 (2005).

24. Kamsah N., *Ph.D. Dissertation*, University of New Hampshire (2001).

25. Dutta I., Park C., Peterson K.A., Vella J., Pan D., *Thermomechanical Phenomena in Electronic Systems -Proceedings of the Intersociety Conference* **2** pp. 137-144 (2004).

26. Garikipati K., Bassman L., Deal M., *J. Mech. Phys. Solids* **49**(6) pp. p 1209-1237 (2001).

27. Bower A.F. and Craft D., *Fatigue and Fracture of Engineering Materials & Structures* **21**(5) pp. 611-630 (1998).

28. Zhang Y.W., Bower A.F., Xia L., Shih C.F., *J. Mech. Phys. Solids* **47**(1) pp. 173-199 (1999).

29. Singh N., Bower A.F., Gan D., Yoon S., Ho P.S., Leu J., Shankar S., *J. Appl. Phys.* **97**(1) pp. 013539.1-11 (2005).

30. Gan D., Huang R., Ho P.S., Leu J., Maiz J., Scherban T., in *Stress-Induced Phenomena in Metallization: 7th International Workshop*, P.S. Ho, et al., Editors, pp. 256-267, American Institute of Physics (2004).

31. Swygenhoven H.V., Caro A., *Appl. Phys. Lett.* **71**(12) p. 1652 (1997).

32. Shiotz J., DiTolla F.D., Jacobsen K., *Nature* **391** p. 561 (1998).

33. Wolf D., Yamakov V., Phillpot S.R., Mukherjee A., Gleiter H., *Acta Mater.* **53**(1) pp. 1-40 (2005).

34. Keblinski P., Wolf D., Gleiter H., Interface Sci. **6**(3) pp. 205-212 (1998).

35. Guo Q., Whitman C.S., Keer L.M., Chung Y.-W., *J. Appl. Phys.* **69**(11) pp. 7572-80 (1991).

36. Fedorov A.A., Gutkin M.Y., Ovid'ko I.A., *Scripta Mater.* **47**(1) pp. 51-55 (2002).

Reproduced with permission of the copyright owner. Further reproduction prohibited without permission.

37. Mullins W.W., *J. Appl. Phys.* **28**(3) pp. 333-339 (1956).

38. Thouless M.D., *Acta Metall.Mater.* **41**(4) pp. 1057-1064 (1992).

39. Sun B. and Suo Z., *Acta Mater.* **45**(12) pp. 4953-4962 (1997).

40. Cocks A.C.F. and Gill S.P.A., *Acta Mater.* **44**(12) pp. 4765-4775 (1996).

41. Pan J., Cocks A.C.F., Kucherenko S., *Proc. Royal Soc. A* **453**(1965) pp. 2161-2184 (1997).

42. Needleman A. and Rice J.R., *Acta Metall.* **28** pp. 1315-1332 (1980).

43. Sauter A.I. and Nix W.D., *J. Mater. Res.* **7**(5) pp. 1133-1143 (1992).

44. Molinari A. and Wright T.D., *J. Mech. Phys. Solids* **53** pp. 1476-1504 (2005).

45. Zhai C.J. and Blish R.C., *J. Appl. Phys.* **97**(11) pp. 113503.1-6 (2005).

46. Rzepka S., Meusel E., Korhonen M., Li C.-Y., *AIP Conference proceedings* **491** pp. 150-161 (1999).

47. Grychanyuk V., Tsukrov I., Gross T., *Int. J. Fracture* **127**(1) pp. 149-154 (2004).

48. Porter D.A. and Easterling K.E., *Phase Transformations in Metals and Alloys.* 2nd ed, London, Chapman&Hall (1992).

49. Frost H.J. and Ashby M.F., *Deformation-Mechanism Maps: the Plasticity and Creep of Metals and Ceramics*, Oxford, Pergamon (1982).

50. Bower A.F. and Wininger E., *J. Mech. Phys. Solids* **52**(6) pp. 1289-1317 (2004).

51. Salencon J., *Handbook of Continuum Mechanics : General Concepts - Thermoelasticity*, Springer (2001).

52. Huebner K.H., Dewhirst D.L., Smith D.E., Byrom T.G., *The Finite Element Method for Engineers*, Wiley-Interscience (2001).

53. *MSC.Marc Volume A: Theory and User Information*, MSC.Software Inc. (2005).

54. Al-Khafaji A.W. and Tooley J.R., *Numerical methods in engineering practice*, New York, CBS College Publishing (1986).

55. Korhonen T., Puska M.J., Nieminen R.M., *Physical Review B* **51**(15) pp. 9526-9532 (1995).

56. Hoshino T., Papanikolau N., Zeller R., Dederichs P.H., Asato M., Asada T., Stefanou N., *Computational Materials Science* **14** pp. 56-61 (1999).

Reproduced with permission of the copyright owner. Further reproduction prohibited without permission.

57. Sato K., Yoshiie T., Satoh Y., Xu Q., *Materials Transactions* **45**(3) pp. 833-838 (2004).

58. Grochola G., Du Plessis J., Snook I.K., Russo S.P., *Surface Science* **591**(1-3) pp. 32-37 (2005).

59. Burton B. and Greenwood G.W., *Metal Sci. J.* **4** pp. 215-18 (1970).

60. Wilshire B. and Palmer C.J., *Scripta Mater.* **46**(7) pp. 483-488 (2002).

61. Harper J.M.E., Cabral C.Jr., Andricacos P.C., Gignac L., Noyan I.C., Rodbell K.P., Hu C.K., *J.Appl.Phys.* **86**(5) pp. 2516-2525 (1999).

Reproduced with permission of the copyright owner. Further reproduction prohibited without permission.

APPENDIX A

LISTING FOR MSC.MARC FORTRAN USER SUBROUTINES

```
c *******************************************************
c     USER-DEFINED COMMON BLOCKS
c *******************************************************
      subroutine usdata(kin,kou,ic)
      implicit real*8 (A-H,O-Z)
      include 'dimen'
      real*8 USRINDISP(2000,2),USRIPSTR(2000,4,3),USRIPFLUX(2000,4,4),
     1 USRBC(2000,3),USRPREVNODFLUX(2000,2),USRTIMINC,
     2 USRINITSHAPE(2000,2),USRC0,USRTEMP,USRPREVTIME,
     3 USRAVESTRESS(100)
      integer USRNCM(2000,4),USRNEDGE,USREDGE(2000,2),
     1 USRNITERPEROUTPUT,USRCRFLAG,USREND,
     2 USRFREE(2000)
      common/USDACM/
c      Inelastic mass flow nodal displacement
       USRINDISP,
c      Element stress computed in 4 integration points
       USRIPSTR,
c      Element flux computed in 4 integration points
       USRIPFLUX,
c      Array to store values of displacement and concentration boundary
       conditions
       USRBC,
c      Flux on previous time step used for numerical integration
       USRPREVNODFLUX,
c      Time increment
       USRTIMINC,
c      Connectivity
       USRNCM,
c      Auxiliary variable for creep strain computation
       USRCRFLAG,
c      Average stress computed on each time step
       USRAVESTRESS,
c      Number of edges which belong to grain boundary
       USRNEDGE,
c      Edges which belong to grain boundary
       USREDGE,
c      Initial uniform value of concentration
       USRC0,
c      Temperature
       USRTEMP,
c      Number of iterations per output
       USRNITERPEROUTPUT,
c      Global time variable
       USRPREVTIME,
c      Initial geometrical configuration
```


Reproduced with permission of the copyright owner. Further reproduction prohibited without permission.

```
        USRINITSHAPE,
c       Total number of increments
        USREND,
c       Indicator array to identify free surface nodes
        USRFREE

c      INITIALIZATION
       if(ic.eq.2) then
         do i = 1,NUMNP
           read(34,*) (USRINITSHAPE(i,j),j=1,2)
           USRINDISP(i,1) = 0.0d0
           USRINDISP(i,2) = 0.0d0
           USRPREVNODFLUX(i,1) = 0.0d0
           USRPREVNODFLUX(i,2) = 0.0d0
           USRBC(i,1) = 0.0d0
           USRBC(i,2) = 0.0d0
         end do
         rewind(26)
         do i = 1,NUMEL
           read(26,*) (USRNCM(i,j),j=1,4)
         end do
         read(27,*) USRNEDGE
         do i = 1,USRNEDGE
           read(27,*) USREDGE(i,1),USREDGE(i,2)
         end do
         read(27,*) USRC0
         read(27,*) USRTEMP
         read(27,*) USREND
         do i = 1,numnp
           read(27,*) USRFREE(i)
         end do
         read(22,*) USRTIMINC
         read(24,*) USRNITERPEROUTPUT
         USRPREVTIME = 0.0d0
         USRCRFLAG = 0
         open(25,file = 'fort.25',position = 'append')
       end if
       return
       end

c *********************************************************
c      ASSIGNMENT OF STRESS-DEPENDENT
c      CONCENTRATION BOUNDARY CONDITIONS
c *********************************************************
        subroutine forcdt(u,v,a,dp,du,time,dtime,ndegl,node,
      1 ug,xord,ncrdl,iacflg,inc,ipass)
        implicit real*8 (A-H,O-Z)
        include 'dimen'
        include 'spacevec'
        include 'strvar'

        dimension u(ndegl),v(ndegl),a(ndegl),dp(ndegl),du(ndegl),
      1 ug(1),xord(1)
        DIMENSION CCNODE(12)
        real*8 USRINDISP(2000,2),USRIPSTR(2000,4,3),USRIPFLUX(2000,4,4),
      1 USRBC(2000,3)
        common/USDACM/ USRINDISP,USRIPSTR,USRIPFLUX,USRBC
```


Reproduced with permission of the copyright owner. Further reproduction prohibited without permission.

```
      if(INC.eq.0) then
        dp(1) = 0.0d0
        dp(2) = 0.0d0
      end if
      if(IPASS.eq.2) then
        du(1) = USRBC(node,3)
        dp(1) = 0.0d0
        dp(2) = 0.0d0
      end if
      return
      end
c *************************************************************
c   COMPUTATION OF CREEP STRAIN INCREMENTS FROM VACANCY FLUXES
c *************************************************************
      SUBROUTINE CRPLAW(EQCP,EQCPNC,STR,CRPE,T,DT,TIMINC,CPTIM,M,
     1 NN,KC,MATUS,NDI,NSHEAR)
      IMPLICIT REAL*8 (A-H, O-Z)
      include 'dimen'
      include 'concom'
      include 'spacevec'
      include 'strvar'
      DIMENSION T(3),DT(1),STR(4),CRPE(4),MATUS(2)
      DIMENSION CCNODE(12)
      real*8 USRINDISP(2000,2),USRIPSTR(2000,4,3),USRIPFLUX(2000,4,4),
     1 USRBC(2000,3),USRPREVNODFLUX(2000,2),USRTIMINC,
     2 USRAVESTRESS(100),USRC0,USRTEMP,USRPREVTIME
      integer USRNCM(2000,4),USRCRFLAG,
     1 USRNEDGE,USREDGE(2000,2),USRNITERPEROUTPUT
      common/USDACM/ USRINDISP,USRIPSTR,USRIPFLUX,USRBC,
     1 USRPREVNODFLUX,USRTIMINC,USRNCM,USRCRFLAG,USRAVESTRESS,
     2 USRNEDGE,USREDGE,USRC0,USRTEMP,USRNITERPEROUTPUT,
     3 USRPREVTIME
c     local variables
      real*8 USRSTRAIN(3)
      real*8 USRDETJ
      real*8 mnod(numnp,2)
      real*8 USRfluxval,USRval,USRvalstr,USRipcrd(2)

c     initialize USRAVESTRESS to zero
      if((M.eq.1).and.(NN.eq.1)) then
        do i = 1,100
          USRAVESTRESS(i) = 0.0d0
        end do
      end if
c     make sure nodal fluxes are computed only once per time increment
      if(((M.eq.1).and.(NN.eq.1)).and.(USRCRFLAG.eq.0)) then
        USRCRFLAG = 1
      else
        if(((M.eq.1).and.(NN.eq.1)).and.(USRCRFLAG.eq.1)) then
          USRCRFLAG = 0
        end if
      end if
      if(((M.eq.1).and.(NN.eq.1)).and.(USRCRFLAG.eq.1)) then
c     EXTRACT ELEMENT FLUXES FROM FEA RESULTS DATABASE
        do i = 1,NUMEL
```


Reproduced with permission of the copyright owner. Further reproduction prohibited without permission.

```
          do j = 1,4
           call ELMVAR(184,i,j,1,USRfluxval)
           USRIPFLUX(i,j,1) = USRfluxval
           call ELMVAR(185,i,j,1,USRfluxval)
           USRIPFLUX(i,j,2) = USRfluxval
           call ELMVAR(181,i,j,1,USRfluxval)
           USRIPFLUX(i,j,3) = USRfluxval
           call ELMVAR(182,i,j,1,USRfluxval)
           USRIPFLUX(i,j,4) = USRfluxval
          end do
         end do
c        compute nodal flux and inelastic displacement
         CALL USRCODE_NODFLUX_INDISP(mnod)
c        update time
         if (INC.gt.0) then
           USRPREVTIME = USRPREVTIME + USRTIMINC
         end if
c        update previous time increment flux values
         do i = 1,NUMNP
           do j = 1,2
             USRPREVNODFLUX(i,j) = mnod(i,j)
           end do
         end do
       end if
c      compute creep strain in M-th element, NN-th integration point
       CALL USRCODE_CREEPSTRAINIP(M,NN,USRSTRAIN,USRDETJ)
c      Output creep strain increments into MSC.Marc workspace
       EQCPNC = 0.0d0
       CRPE(1) = USRSTRAIN(1)
       CRPE(2) = USRSTRAIN(2)
       CRPE(3) = 0.0d0
       CRPE(4) = USRSTRAIN(3)
c      contribution of M-th element, NN-th integration point to average
       stress
       do i = 1,3
         USRAVESTRESS(i) = USRAVESTRESS(i) + USRDETJ*USRIPSTR(M,NN,i)
       end do
       USRAVESTRESS(4) = USRAVESTRESS(4) + USRDETJ
       RETURN
       END

c *******************************************************
c      COMPUTATIONS OF CONCENTRATION BOUNDARY CONDITIONS
c *******************************************************
       SUBROUTINE UEDINC(INC,INCSUB)
       IMPLICIT REAL*8 (A-H, O-Z)
       include 'dimen'
       include 'spacevec'
       include 'strvar'
       real*8 USRINDISP(2000,2),USRIPSTR(2000,4,3),USRIPFLUX(2000,4,4),
      1 USRBC(2000,3),USRPREVNODFLUX(2000,2),USRTIMINC,
      2 USRINITSHAPE(2000,2), USRC0,USRTEMP,USRPREVTIME,
      3 USRAVESTRESS(100)
       integer USRNCM(2000,4),USRNEDGE,USREDGE(2000,2),
      1 USRNITERPEROUTPUT,USRCRFLAG,USREND,
      2 USRFREE(2000)
       common/USDACM/ USRINDISP,USRIPSTR,USRIPFLUX,USRBC,
```


Reproduced with permission of the copyright owner. Further reproduction prohibited without permission.

```
     1 USRPREVNODFLUX,USRTIMINC,USRNCM,USRCRFLAG,USRAVESTRESS,
     2 USRNEDGE,USREDGE,USRC0,USRTEMP,USRNITERPEROUTPUT,
     3 USRPREVTIME,USRINITSHAPE,USREND,USRFREE
c     internal variables
      real*8 crd(NUMNP,2)
      real*8 USRval,USRvecval(2)
      integer USRIntVal
      DIMENSION CCNODE(12),DDNODE(12)

c     extract current configuration coordinates from FEA database
      do i = 1,NUMNP
        JRDPRE = 0
        call VECFTC(CCNODE,XORD_D,NCRDMX,NCRD,i,JRDPRE,2,1)
        JRDPRE = 0
        CALL VECFTC(DDNODE,DSXTS_D,NDEGMX,NDEG,i,JRDPRE,2,5)
        crd(i,1) = CCNODE(1) + DDNODE(1)
        crd(i,2) = CCNODE(2) + DDNODE(2)
      end do
c     update vacancy concentration boundary conditions
      CALL USRCODE_NEWCONCENTRATIONBC(crd)
c     output results to file
      USRIntVal = INC/USRNITERPEROUTPUT
      if(USRIntVal*USRNITERPEROUTPUT.eq.INC) then
        CALL USRCODE_WRITEOUTPUTFILE(INC,crd)
c     output average stress
        do i = 1,3
          USRAVESTRESS(i) = USRAVESTRESS(i)/USRAVESTRESS(4)
        end do
        write(31,'(4E15.6)') USRPREVTIME,USRAVESTRESS(1)
      end if
      RETURN
      END

c *********************************************************
c   EXTRACTING ELEMENT STRESS FROM FEA RESULTS DATABASE
c *********************************************************
      SUBROUTINE ELEVAR(N,NN,KC,GSTRAN,GSTRES,STRESS,PSTRAN,
     1 CSTRAN,VSTRAN,CAUCHY,EPLAS,EQUIVC,SWELL,KRTYP,PRANG,DT,
     2 GSV,NGENS,NGEN1,NSTATS,NSTASS,THERM)
      IMPLICIT REAL*8 (A-H, O-Z)
      include 'concom'
      DIMENSION GSTRAN(NGENS),GSTRES(NGENS),
     1 STRESS(NGEN1),PSTRAN(NGEN1),CSTRAN(NGEN1),VSTRAN(NGEN1),
     2 CAUCHY(NGEN1),DT(NSTATS),GSV(1),THERM(NGEN1),KRTYP(4),
     3 PRANG(3,2)
      real*8 USRINDISP(2000,2),USRIPSTR(2000,4,3)
      common/USDACM/ USRINDISP,USRIPSTR

      if(IPASS.eq.1) then
        USRIPSTR(N,NN,1) = STRESS(1)
        USRIPSTR(N,NN,2) = STRESS(2)
        USRIPSTR(N,NN,3) = STRESS(4)
      end if
      RETURN
      END

c *********************************************************
```


Reproduced with permission of the copyright owner. Further reproduction prohibited without permission.

```
c     COMPUTATION OF INITIAL THERMAL STRAINS
c *******************************************************
      SUBROUTINE ANEXP (N,NN,KC,T,TINC,COED1,NDI,NSHEAR,EQEXP)
      IMPLICIT REAL*8 (A-H, O-Z)
      include 'concom'
      include 'matdat'
      DIMENSION EQEXP(3),TINC(1),T(1),COED1(NDI),N(2)
      real*8 USRINDISP(2000,2),USRIPSTR(2000,4,3),USRIPFLUX(2000,4,4),
     1 USRBC(2000,3),USRPREVNODFLUX(2000,2),USRTIMINC,USRC0,USRTEMP,
     2 USRAVESTRESS(100)
      integer USRNCM(2000,4),USRNEDGE,USREDGE(2000,2),
     1 USRCRFLAG
      common/USDACM/ USRINDISP,USRIPSTR,USRIPFLUX,USRBC,
     1 USRPREVNODFLUX,USRTIMINC,USRNCM,USRCRFLAG,USRAVESTRESS,
     2 USRNEDGE,USREDGE,USRC0,USRTEMP

       IF(INC.eq.0) then
         EQEXP(1) = (1.0d0 + XU(1))*COED1(1)*(USRTEMP - 293.0d0)
         EQEXP(2) = EQEXP(1)
         EQEXP(3) = 0.0d0
       ELSE
         EQEXP(1) = 0.0d0
         EQEXP(2) = 0.0d0
         EQEXP(3) = 0.0d0
       END IF
      RETURN
      END

c **********************************************************************
c     COMPUTATION OF NODAL FLUXES AND INELASTIC DISPLACEMENTS
c     (nodal values are averaged over neighboring integration point
c      values)
c**********************************************************************
      SUBROUTINE USRCODE_NODFLUX_INDISP(mnod)
      IMPLICIT REAL*8 (A-H, O-Z)
      include 'dimen'
      real*8 mnod(NUMNP,2)
      real*8 USRINDISP(2000,2),USRIPSTR(2000,4,3),USRIPFLUX(2000,4,4),
     1 USRBC(2000,3),USRPREVNODFLUX(2000,2),USRTIMINC
      integer USRNCM(2000,4)
      common/USDACM/ USRINDISP,USRIPSTR,USRIPFLUX,USRBC,
     1 USRPREVNODFLUX,USRTIMINC,USRNCM
c     local variables
      integer i,j
      integer adds(NUMNP),USRintval

c     Compute nodal fluxes by averaging over neighboring integration
      point values
          do i = 1,NUMNP
            adds(i) = 0
            do j = 1,2
              mnod(i,j) = 0.0d0
            end do
          end do
          do i = 1,numel
            do j = 1,2
           mnod(USRNCM(i,1),j) = mnod(USRNCM(i,1),j) + USRIPFLUX(i,1,j)
```


Reproduced with permission of the copyright owner. Further reproduction prohibited without permission.

```
          mnod(USRNCM(i,2),j) = mnod(USRNCM(i,2),j) + USRIPFLUX(i,2,j)
          mnod(USRNCM(i,3),j) = mnod(USRNCM(i,3),j) + USRIPFLUX(i,4,j)
          mnod(USRNCM(i,4),j) = mnod(USRNCM(i,4),j) + USRIPFLUX(i,3,j)
          end do
          do j = 1,4
            adds(USRNCM(i,j)) = adds(USRNCM(i,j)) + 1
          end do
        end do
        do i = 1,NUMNP
          do j = 1,2
            if(adds(i).gt.0) then
              mnod(i,j) = mnod(i,j)/(1.0d0*adds(i))
            end if
          end do
        end do
c    Compute increment of mass flow displacement
        do i = 1,NUMNP
          do j = 1,2
            USRINDISP(i,j)=-5.0d-1
     1      *(mnod(i,j)+USRPREVNODFLUX(i,j))*USRTIMINC
          end do
        end do
      END SUBROUTINE

c ********************************************************************
c COMPUTATION OF CREEP STRAIN IN M-TH ELEMENT, NN-TH INTEGRATION POINT
c (using FEA element shape functions to compute strains from nodal
c  inelastic displacements)
c********************************************************************
      SUBROUTINE USRCODE_CREEPSTRAINIP(M,NN,USRSTRAIN,USRDETJ)
      IMPLICIT REAL*8 (A-H, O-Z)
      include 'dimen'
      include 'spacevec'
      include 'strvar'
      DIMENSION CCNODE(12),DDNODE(12)
      INTEGER M,NN
      REAL*8 USRSTRAIN(3),USRDETJ
      real*8 USRINDISP(2000,2),USRIPSTR(2000,4,3),USRIPFLUX(2000,4,4),
     1 USRBC(2000,3),USRPREVNODFLUX(2000,2),USRTIMINC,
     2 USRAVESTRESS(100),USRC0,USRTEMP,USRPREVTIME,USRINITSHAPE(2000,2)
      integer USRNCM(2000,4),USRCRFLAG,
     1 USRNEDGE,USREDGE(2000,2),USRNITERPEROUTPUT,USREND
      common/USDACM/ USRINDISP,USRIPSTR,USRIPFLUX,USRBC,
     1 USRPREVNODFLUX,USRTIMINC,USRNCM,USRCRFLAG,USRAVESTRESS,
     2 USRNEDGE,USREDGE,USRC0,USRTEMP,USRNITERPEROUTPUT,
     3 USRPREVTIME,USRINITSHAPE,USREND
c       local variables
      real*8 USRCRD(4,2),USRIP(4,2),USRQ(8)
      real*8 USRA(3,4),USRDIFF1(2,4),USRDIFF2(4,8)
      real*8 USRJM(2,2),USRB(3,8)
      real*8 val
      integer i,j,II,JJ,KK

      val = 1.0d0/sqrt(3.0d0)
      USRIP(1,1) = -val
      USRIP(1,2) = -val
      USRIP(2,1) = val
```


Reproduced with permission of the copyright owner. Further reproduction prohibited without permission.

```
      USRIP(2,2) = -val
      USRIP(3,1) = -val
      USRIP(3,2) = val
      USRIP(4,1) = val
      USRIP(4,2) = val
      do i = 1,4
        JRDPRE = 0
        call VECFTC(CCNODE,XORD_D,NCRDMX,NCRD,USRNCM(M,i),JRDPRE,2,1)
        JRDPRE = 0
        CALL VECFTC(DDNODE,DSXTS_D,NDEGMX,NDEG,USRNCM(M,i),JRDPRE,2,5)
        USRCRD(i,1) = CCNODE(1) + DDNODE(1)
        USRCRD(i,2) = CCNODE(2) + DDNODE(2)
      end do
      do i = 1,4
        USRQ(2*i-1) = USRINDISP(USRNCM(M,i),1)
        USRQ(2*i) = USRINDISP(USRNCM(M,i),2)
      end do
      do i = 1,3
        do j = 1,4
          USRA(i,j) = 0.0d0
        end do
      end do
      do i = 1,4
        do j = 1,8
          USRDIFF2(i,j) = 0.0d0
        end do
      end do
c       Strain in integration point NN
        USRDIFF1(1,1) = -0.25d0*(1.0d0-USRIP(NN,2))
        USRDIFF1(1,2) = -USRDIFF1(1,1)
        USRDIFF1(1,3) = 0.25d0*(1.0d0+USRIP(NN,2))
        USRDIFF1(1,4) = -USRDIFF1(1,3)
        USRDIFF1(2,1) = -0.25d0*(1.0d0-USRIP(NN,1))
        USRDIFF1(2,2) = -0.25d0*(1.0d0+USRIP(NN,1))
        USRDIFF1(2,3) = -USRDIFF1(2,2)
        USRDIFF1(2,4) = -USRDIFF1(2,1)
        DO II = 1,2
          DO JJ = 1,2
            USRJM(II,JJ) = 0.0d0
            DO KK = 1,4
              USRJM(II,JJ) = USRJM(II,JJ) +
     1         USRDIFF1(II,KK)*USRCRD(KK,JJ)
            END DO
          END DO
        END DO
        USRDETJ = USRJM(1,1)*USRJM(2,2) - USRJM(1,2)*USRJM(2,1)
        USRA(1,1) = USRJM(2,2)/USRDETJ
        USRA(1,2) = -USRJM(1,2)/USRDETJ
        USRA(2,3) = -USRJM(2,1)/USRDETJ
        USRA(2,4) = USRJM(1,1)/USRDETJ
        USRA(3,1) = -USRJM(2,1)/USRDETJ
        USRA(3,2) = USRJM(1,1)/USRDETJ
        USRA(3,3) = USRJM(2,2)/USRDETJ
        USRA(3,4) = -USRJM(1,2)/USRDETJ
        DO I = 1,4
          USRDIFF2(1,2*I-1) = USRDIFF1(1,I)
          USRDIFF2(2,2*I-1) = USRDIFF1(2,I)
```


Reproduced with permission of the copyright owner. Further reproduction prohibited without permission.

```
          USRDIFF2(3,2*I) = USRDIFF1(1,I)
          USRDIFF2(4,2*I) = USRDIFF1(2,I)
        END DO
c       Strain-displacement matrix
        DO II = 1,3
          DO JJ = 1,8
            USRB(II,JJ) = 0.0d0
            DO KK = 1,4
              USRB(II,JJ) = USRB(II,JJ) + USRA(II,KK)*USRDIFF2(KK,JJ)
            END DO
          END DO
        END DO
c       Diffusion creep strain in element integration points
        DO II = 1,3
          USRSTRAIN(II) = 0.0d0
          DO KK = 1,8
            USRSTRAIN(II) = USRSTRAIN(II) + USRB(II,KK)*USRQ(KK)
          END DO
        END DO
      END SUBROUTINE


c ***********************************************************************
c   COMPUTATION OF CONCENTRATION BOUNDARY CONDITIONS
c***********************************************************************
      SUBROUTINE USRCODE_NEWCONCENTRATIONBC(crd)
      IMPLICIT REAL*8 (A-H, O-Z)
      include 'dimen'
      REAL*8 CRD(NUMNP,2)
      real*8 USRINDISP(2000,2),USRIPSTR(2000,4,3),USRIPFLUX(2000,4,4),
     1 USRBC(2000,3),USRPREVNODFLUX(2000,2),USRTIMINC,
     2 USRINITSHAPE(2000,2),USRC0,USRTEMP,USRPREVTIME,USRAVESTRESS(100)
      integer USRNCM(2000,4),USRNEDGE,USREDGE(2000,2),
     1 USRNITERPEROUTPUT,USRCRFLAG,USREND,
      2 USRFREE(2000)
      common/USDACM/ USRINDISP,USRIPSTR,USRIPFLUX,USRBC,
     1 USRPREVNODFLUX,USRTIMINC,USRNCM,USRCRFLAG,USRAVESTRESS,
     2 USRNEDGE,USREDGE,USRC0,USRTEMP,USRNITERPEROUTPUT,
     3 USRPREVTIME,USRINITSHAPE,USREND,USRFREE
c     internal variables
      real*8 mnod(NUMNP,3)
      real*8 stressprod(NUMNP)
      real*8 KB,OMEGA,normal(2),len,USRval
      integer adds(NUMNP),USRIntVal

      KB = 1.3806d-23
      OMEGA = 1.18d-29
c     COMPUTATION OF NODAL STRESSES BY AVERAGING OVER INTEGRATION POINT
      VALUES
      DO i = 1,NUMNP
        adds(i) = 0
        do j = 1,3
          mnod(i,j) = 0.0d0
        end do
      END DO
      do i = 1,numel
        do j = 1,3
```


Reproduced with permission of the copyright owner. Further reproduction prohibited without permission.

```
          mnod(USRNCM(i,1),j) = mnod(USRNCM(i,1),j) + USRIPSTR(i,1,j)
          mnod(USRNCM(i,2),j) = mnod(USRNCM(i,2),j) + USRIPSTR(i,2,j)
          mnod(USRNCM(i,3),j) = mnod(USRNCM(i,3),j) + USRIPSTR(i,4,j)
          mnod(USRNCM(i,4),j) = mnod(USRNCM(i,4),j) + USRIPSTR(i,3,j)
        end do
        do j = 1,4
          adds(USRNCM(i,j)) = adds(USRNCM(i,j)) + 1
        end do
      end do
      do i = 1,NUMNP
        do j = 1,3
          if(adds(i).gt.0) then
            mnod(i,j) = mnod(i,j)/(1.0d0*adds(i))
          end if
        end do
      end do
c     COMPUTATION OF NORMALS TO BOUNDARY, AND NORMAL TRACTIONS
      do i = 1,NUMNP
        adds(i) = 0
        stressprod(i) = 0.0d0
      end do
      do i = 1,USRNEDGE
        normal(1) = crd(USREDGE(i,2),2) - crd(USREDGE(i,1),2)
        normal(2) = crd(USREDGE(i,1),1) - crd(USREDGE(i,2),1)
        len = sqrt(normal(1)**2 + normal(2)**2)
        if (len.ne.0.0d0) then
          normal(1) = normal(1)/len
          normal(2) = normal(2)/len
        end if
        do j = 1,2
          stressprod(USREDGE(i,j)) = stressprod(USREDGE(i,j))
     1    + mnod(USREDGE(i,j),1)*normal(1)**2
     2    + mnod(USREDGE(i,j),2)*normal(2)**2
     3    + 2.0*mnod(USREDGE(i,j),3)*normal(1)*normal(2)
          adds(USREDGE(i,j)) = adds(USREDGE(i,j)) +1
        end do
      end do
      USRIntVal = 0
c     STRESS-DEPENDENT BOUNDARY VACANCY CONCENTRATIONS
      do i = 1,NUMNP
        if(adds(i).gt.0) then
          stressprod(i) = stressprod(i)/(1.0d0*adds(i))
          stressprod(i) = USRC0*exp(stressprod(i)*OMEGA/(kb*USRTEMP))
          USRBC(i,3) = stressprod(i)
          if(USRFREE(i).ne.0) then
            USRBC(i,3) = USRC0
          end if
        end if
      end do
      END SUBROUTINE

c ***********************************************************************
c    OUTPUT OF RESULTS INTO JOB.T19 FILE FOR MENTAT2005
c***********************************************************************
      SUBROUTINE USRCODE_WRITEOUTPUTFILE(INC,crd)
      IMPLICIT REAL*8 (A-H, O-Z)
      include 'dimen'
```


Reproduced with permission of the copyright owner. Further reproduction prohibited without permission.

```
      INTEGER INC
      REAL*8 CRD(NUMNP,2)
      real*8 USRINDISP(2000,2),USRIPSTR(2000,4,3),USRIPFLUX(2000,4,4),
     1 USRBC(2000,3),USRPREVNODFLUX(2000,2),USRTIMINC,
     2 USRINITSHAPE(2000,2),USRC0,USRTEMP,USRPREVTIME,USRAVESTRESS(100)
      integer USRNCM(2000,4),USRNEDGE,USREDGE(2000,2),
     1 USRNITERPEROUTPUT,USRCRFLAG
      common/USDACM/ USRINDISP,USRIPSTR,USRIPFLUX,USRBC,
     1 USRPREVNODFLUX,USRTIMINC,USRNCM,USRCRFLAG,USRAVESTRESS,
     2 USRNEDGE,USREDGE,USRC0,USRTEMP,USRNITERPEROUTPUT,
     3 USRPREVTIME,USRINITSHAPE
c     internal variables
      real*8 mnod(numnp,3)
      real*8 USRval

          backspace(25)
          write(25,'(A4)') '****'
          write(25,'(A27,A43)')'=beg=51600 (Loadcase Title)',' '
          write(25,'(A10,A60)')'job       ',' '
          write(25,'(A5)') '=end='
          write(25,'(A48,A22)')
     1    '=beg=51701 (Integer Increment Verification Data)',' '
          write(25,'(6I13)') 0,INC,0,120,3,0
          write(25,'(6I13)') 0,1,0,0,0,0
          write(25,'(A5)') '=end='
          write(25,'(A45,A25)')
     1    '=beg=51801 (Real Increment Verification Data)',' '
          write(25,'(I13)') 24
          write(25,'(6E13.6)') USRPREVTIME,0.0,0.0,0.0,0.0,0.0
          write(25,'(6E13.6)') 0.0,0.0,0.0,0.0,0.0,0.0
          write(25,'(6E13.6)') 0.0,0.0,0.0,0.0,0.0,0.0
          write(25,'(6E13.6)') 0.0,0.0,0.0,0.0,0.0,0.0
          write(25,'(A5)') '=end='
          write(25,'(A43,A27)')
     1    '=beg=52000 (Magnitude of Distributed Loads)',' '
          write(25,'(3E13.6)') 0.0,0.0,0.0
          write(25,'(A5)') '=end='
          write(25,'(A45,A25)')
     1    '=beg=52300 (Element Integration Point Values)',' '
          do i = 1,numel
            do j = 1,4
              write(25,'(5E13.6)') (USRIPSTR(i,j,k),k=1,3),
     1         (USRIPFLUX(i,j,k),k=1,2)
            end do
          end do
          write(25,'(A5)') '=end='
          write(25,'(A26,A44)')'=beg=52401 (Nodal Results)',' '
          write(25,'(2I13)') 2,3
          write(25,'(A12,A36)') 'Displacement',' '
          write(25,'(6I13)') 1,0,0,2,0,0
          write(25,'(6I13)') -1,0,0,0,0,0
          do i = 1,NUMNP
            mnod(i,1) = crd(i,1) - USRINITSHAPE(i,1)
            mnod(i,2) = crd(i,2) - USRINITSHAPE(i,2)
          end do
          write(25,'(6E13.6)') ((mnod(i,j),j=1,2),i=1,NUMNP)
          write(25,'(A11,A37)') 'Temperature',' '
```


Reproduced with permission of the copyright owner. Further reproduction prohibited without permission.

```
    write(25,'(6I13)') 14,0,0,1,0,0
    write(25,'(6I13)') -1,0,0,0,0,0
    do i = 1,numnp
      call nodvar(14,i,USRval,1,0)
      mnod(i,3) = USRval
    end do
    write(25,'(6E13.6)') (mnod(i,3),i=1,NUMNP)
    write(25,'(A5)') '=end='
    write(25,'(A29,A41)') '=beg=52900 (Global Variables)',' '
    write(25,'(2I13)') 1,1
    write(25,'(A30,A18)') 'Loadcase Percentage Completion',' '
    write(25,'(6I13)') 7,0,0,1,0,0
    write(25,'(E13.6)') 0.0
    write(25,'(A5)') '=end='
    write(25,'(A4)') '----'
    write(25,'(A4)') '++++'
END SUBROUTINE
```


Reproduced with permission of the copyright owner. Further reproduction prohibited without permission.